# Imitating nature to produce nacre-inspired composite materials with bacteria

Schmieden, Dominik

**DOI**
10.4233/uuid:d165937b-4e6d-459d-acfb-5d45e46d4edf

**Publication date**
2019

**Document Version**
Final published version

**Citation (APA)**
Schmieden, D. (2019). *Imitating nature to produce nacre-inspired composite materials with bacteria*. [Dissertation (TU Delft), Delft University of Technology]. https://doi.org/10.4233/uuid:d165937b-4e6d-459d-acfb-5d45e46d4edf

**Important note**
To cite this publication, please use the final published version (if applicable).
Please check the document version above.

# IMITATING NATURE TO PRODUCE NACRE-INSPIRED COMPOSITE MATERIALS WITH BACTERIA

# IMITATING NATURE TO PRODUCE NACRE-INSPIRED COMPOSITE MATERIALS WITH BACTERIA

## Dissertation

for the purpose of obtaining the degree of doctor
at Delft University of Technology
by the authority of the Rector Magnificus, Prof.dr.ir. T.H.J.J. van der Hagen,
chair of the Board for Doctorates
to be defended publicly on Wednesday 20 March 2019 at 12:30 o'clock

by

**Dominik Tobias SCHMIEDEN**
Diplom Biologe, Johannes Gutenberg-Universität, Mainz, Germany

born in Wiesbaden, Germany.

This dissertation has been approved by the promotors.

Composition of the doctoral committee:

| | |
|---|---|
| Rector Magnificus, | chairperson |
| Prof. dr. A.S. Meyer | University of Rochester, USA, promotor |
| Dr. M.-E. Aubin-Tam | Delft University of Technology, copromotor |
| | |
| *Independent members:* | |
| Prof. dr. ir. H.E.J.G. Schlangen | Delft University of Technology |
| Prof. dr. R. Jerala | National Institute of Chemistry, Slovenia |
| Prof. dr. A.A. Zadpoor | Delft University of Technology |
| Dr. F. Natalio | Weizmann Institute of Science, Israel |
| Dr. E. Karana | Delft University of Technology |





This work was supported by the
Netherlands Organisation for Scientific Research (NWO/OCW).

*Keywords:* Biomimetics, nacre, biomaterials, synthetic biology, 3D printing, bioprinting



Casimir PhD Series, Delft-Leiden 2019-03

ISBN 978-90-8593-385-4

An electronic version of this dissertation is available at
`http://repository.tudelft.nl/`.

# CONTENTS

# SUMMARY

In this study, a method for the bacterial production of a nacre-mimicking composite material was developed. Nacre (mother-of-pearl) is an organic-inorganic composite found in the inner lining of many mollusk shells and in pearls. It has a brick-and-mortar structure consisting of 95% aragonite (calcium carbonate) platelets and 5% organic matrix. Serving as a protective structure against e.g. predators, nacre has developed into an extremely strong and tough material, despite largely consisting of ceramic calcium carbonate. Numerous mechanisms have been proposed to explain the outstanding mechanical properties of nacre, such as crack deflection and local strain hardening. Many groups are pursuing the aim of developing new materials which mimic nacre's structure and mechanical properties. Nacre is produced by mollusks at ambient temperatures with easily obtainable materials and with low expenditure of energy. In contrast, human methods usually require extensive energy input, high temperatures and/or pressures, and environmentally damaging chemicals.

In Chapter 2, a method for the production of "bacterial nacre" is presented. Bacteria are widely used as efficient microfactories for the production of various compounds. They are thus suitable candidate organisms towards the goal of developing a production method that can compare in efficiency to natural nacre growth. To produce bacterial nacre, the ureolytic bacterium *Sporosarcina pasteurii* was used to crystallize calcium carbonate. *S. pasteurii* hydrolyzes urea in the growth medium, leading to the release of ammonia and $CO_2$, which makes calcium carbonate fall out of solution. The bacterium *Bacillus licheniformis* was used to produce $\gamma$-polyglutamate (PGA). Calcium carbonate and PGA were alternately deposited on a glass substrate. The resulting coating showed layered structures reminiscent of nacre's layers in about 40% of the cross-sectional area of the samples. The layers had a thickness of about 8 µm, as opposed to about 0.5 µm in natural nacre.

In Chapter 3, the method was improved by producing bacterial nacre on PMMA substrates, allowing for the testing of the mechanical properties. Bacterial nacre was compared with a PGA-free, bacterially-produced calcium carbonate ("bacterial $CaCO_3$"), a chemically-produced calcium carbonate ("chemical $CaCO_3$"), and with natural *Mytilus edulis* nacre. As before, bacterial nacre was partly layered, while layers were restricted to spherulites in bacterial $CaCO_3$ and absent in chemical $CaCO_3$. Both bacterially-produced materials showed a nano-granular structure, and bacterial nacre additionally displayed asperities, small protrusions on the layer surfaces, which are also found in nacre and thought to play an important role in strain hardening. X-ray diffraction revealed that both bacterial nacre and bacterial $CaCO_3$ consisted of a mixture of the calcium carbonate polymorphs calcite and vaterite, chemical $CaCO_3$ consisted of purely calcite, and natural nacre consisted of aragonite. With thermogravimetry, an organic content of 4.4% was estimated in bacterial nacre, which is comparable to the content of 3.7% in natural nacre. Indentation and 3-point bending tests revealed an approximately four-fold in-

crease in toughness, as well as increased strain at failure between bacterial nacre and chemical $CaCO_3$, suggesting structure-derived toughening mechanisms. In bending experiments, both bacterial and chemical $CaCO_3$ failed with visible macrocracks, while bacterial nacre failed in a microcrack mode. This difference might be caused by toughening mechanisms such as crack deflection at layers, strain hardening due to nano-asperities, and PGA acting as a viscoelastic glue.

The bacterial nacre demonstrates that it is possible to produce a nacre-mimicking material with bacteria in a relatively inexpensive way and with a low ecological impact. However, the layer-by-layer process described here is slow and labor-intensive. A method that allows for the production of a bulk material instead of a coating would be desirable. Natural nacre grows by crystallization in a pre-formed organic matrix. If bacteria could be patterned efficiently and induced to produce such a matrix, the production process could potentially be sped up considerably. Chapter 4 reviews current approaches to achieve patterning in bacterial communities.

In Chapter 5, a 3D printer is presented that was re-purposed for extruding bioink, a suspension of bacteria in an alginate solution. When printed on $CaCl_2$-containing agar plates, the bioink solidified to form a gel, fixing the bacteria in a 3D structure. The printer produced lines down to the millimeter scale reliably with sub-millimeter resolution. A good separation of two stacked layers was observed when printing two different bacterial strains above each other. Additionally, the bacteria were shown to remain viable for at least 24 hours and expression of a fluorescent marker could be induced by addition of a chemical inducer to the agar substrate. This work demonstrates that bacteria can be patterned in macroscopic 3D structures by an easy, cost-effective, and reproducible process which does not require genetic engineering. At the same time, the bacteria remain accessible to the experimenter through chemical inducers.

Apart from controlled spacial patterning, production of new bulk materials with 3D-printed bacteria requires formation of a chemically-stable structure and long-term survival of the cells. In Chapter 6, bacteria were 3D-printed and induced to form a biofilm, an aggregate of cells surrounded by a self-produced matrix. To achieve control over biofilm formation, the expression of the *csgA* gene was controlled with a chemical inducer. CsgA self-aggregates into protein nanofibers (called curli) on the cell surface, interconnecting the cells. Curli fibers form the major extracellular component of the extracellular matrix of natural *E. coli* biofilms. When CsgA was produced by the printed bacteria, the gels remained stable even when treated with the gel-dissolving agent citrate. It was also demonstrated that cells in thus produced 3D structures remained stably patterned and viable for at least seven days. Additionally, a 3D printer built from K'NEX toy construction kit parts and standard electronic components is demonstrated. This "Biolinker" is the cheapest 3D printer for cells to date, and can serve as an interdisciplinary educational tool in the sciences.

3D-printed biofilms could be the first step towards the production of large-scale, living materials, which could mimic the properties of nacre in combination with biomineralization. High-performance, eco-friendly nacre-mimetic materials could be very useful in fields such as medicine, construction, or aerospace engineering, due to their high biocompatibility, reliability, and low weight. When combined with genetic engineering, 3D

printing of bacteria could lead to the development of completely new, tailored materials for a big variety of applications in science and engineering.

# SAMENVATTING

In dit onderzoek word gezocht naar een methode om een door bacteriën geproduceerde parelmoerachtige samengestelde bouwstof te ontwikkelen. Parelmoer is een organisch-inorganisch materiaal in de binnenkant van de schelpen van weekdieren en in parels. Het heeft een baksteen-en-mortel structuur met 95% aragonietplaatjes (calciumcarbonaat) en 5% organische matrix. Omdat parelmoer een beschermingsbarriere tegen bijvoorbeeld roofdieren is, is het zeer sterk en taai, hoewel het vooral uit keramisch calciumcarbonaat bestaat. Het materiaal werd onderzocht op de mechanismen om dit te verklaren, bijvoorbeeld crack deflection en plaatselijke versteviging. Vanwege die kwaliteiten probeert men materialen te ontwikkelen met de structuur en de eigenschappen van parelmoer. Weekdieren produceren parelmoer met weinig energie, de in hun omgeving beschikbare materialen, en bij relatief lage omgevingstemperatuur. Tot nu toe zijn voor het imiteren van parelmoer veel energie, hoge temperaturen en/of druk en voor de omgeving schadelijke materialen nodig.

In hoofdstuk 2 wordt een methode voor de productie van "bacterieel parelmoer" voorgesteld. Bacteriën worden veel gebruikt als micro-fabrieken voor de productie van verscheidene verbindingen. Daarom zijn het goede kandidaten voor een efficiënte productiemethode van kunstmatige parelmoer met vergelijkbare eigenschappen. Om bacterieel parelmoer te maken werd de bacterie *Sporosarcina pasteurii* gebruikt om calciumcarbonaat te kristalliseren. *S. pasteurii* hydrolyseert urea in de voedingsbodem, waarbij ammonium en $CO_2$ vrijkomen. Als er $Ca^{2+}$-ionen zijn, precipiteert calciumcarbonaat. De bacterie *Bacillus licheniformis* werd gebruikt om $\gamma$-polyglutamaat (PGA) te produceren. Calciumcarbonaat en PGA werden afwisselend op een objectglaasje aangebracht. De daardoor onstane bedekking had lagen zoals parelmoer in circa 40% van de oppervlakte van de dwardsdoorsnede. De lagen waren circa 8 µm dik, in tegenstelling tot 0.5 µm in natuurlijk parelmoer.

In hoofdstuk 3 werd deze methode voor bacterieel parelmoer verbeterd door het aanbrengen van dit materiaal op een PMMA schijfje, zodat de mechanische eigenschappen gemeten konden worden. Bacterieel parelmoer werd vergeleken met bacterieel geproduceerd PGA-vrij calciumcarbonaat ("bacterieel $CaCO_3$"), met chemisch geproduceerd calciumcarbonaat ("chemisch $CaCO_3$"), en met natuurlijk *Mytilus edulis* parelmoer. Zoals in het eerdere experiment werd er geconstateerd dat er in een gedeelte van het bacteriële parelmoer lagen voorkwamen. Lagen waren verder alleen zichtbaar in spherulites in bacteriel $CaCO_3$. In chemisch $CaCO_3$ kwamen geen lagen voor. Beide bacterieel geproduceerde materialen hadden een nano-korrelige structuur en in bacterieel parelmoer kwamen ook kleine uitsteeksels voor op de oppervlakte van de lagen. Deze "nano-asperities" zijn belangijk voor de plaatselijke versteviging in natuurlijk parelmoer. Röntgendiffractie studies toonden dat bacterieel parelmoer en bacterieel $CaCO_3$ uit calciet en vateriet bestonden, chemisch $CaCO_3$ alleen uit calciet, en natuurlijk parelmoer uit aragoniet. Met hulp van thermogravimetrische analyse wordt geschat dat er 4.4% or-

ganische verbindingen in bacterieel parelmoer voorkwamen. Dat is vergelijkbaar met de 3.7% die in parelmoer gemeten werden. Indentatie en driepuntsbuiging testen toonden dat bacterieel parelmoer circa 4 keer taaier is dan bacterieel $CaCO_3$. Dit verschil is waarschijnlijk veroorzaakt door verschillen in de structuren. In driepuntsbuiging tests waren grote barsten in bacterieel en chemisch $CaCO_3$ te zien, in bacterieel parelmoer kwamen alleen kleine barsten voor. Dit verschil zou het gevolg kunnen zijn van taaiheid veroorzakende mechanismen, zoals crack deflection aan lagen, versteviging door nano-asperities, en PGA als viscoelastische lijm.

Het bacteriele parelmoer demonstreert dat het mogelijk is een parelmoer-imiterend materiaal te creëren met bacteriën op een goedkope en milieuvriendelijke manier. Dit laag-per-laag proces is echter langzaam en arbeidsintensief. Een methode voor de productie van grote volumes in plaats van een bedekking zou wenselijker zijn. Natuurlijk parelmoer groeit in een organische matrix. Als het mogelijk was bacteriën in een gecontroleerd patroon te plaatsen en een vergelijkbare organische matrix te maken, zou er de mogelijkheid zijn dat het productieproces veel sneller verloopt. In hoofdstuk 4 worden verscheidene manieren samengevat om bacteriën een patroon te laten vormen.

In hoofdstuk 5 wordt een 3D printer voor bacteriën gepresenteerd, welke ontwikkeld is door een commerciële printer aan te passen. Deze printer drukt "bioink", een suspensie van bacteriën in en oplossing van alginaat. Als de bioink op een agar ondergrond met $CaCl_2$ aangebracht wordt, vormt die een gel die de bacteriën fixeert. De printer produceerde enkele millimeters dikke lijnen op een betrouwbare manier, en structuren met een resolutie van minder dan een millimeter. Een goede isolatie kon worden waargenomen tussen twee lagen met verschillende bacteriën die op elkaar geplaatst werden. De bacteriën bleven leven voor tenminste 24 uren en de productie van een fluorescerend proteïne kon teweeg gebracht worden door een chemische stof toe te voegen. Dit onderzoek toont aan dat bacteriën door 3D printen op een gemakkelijke, goedkope en reproduceerbare manier, zonder genetische modificaties toe te passen, in macroscopische structuren geplaatst kunnen worden. Gelijktijdig kan men de bacteriën met chemische stoffen beïnvloeden.

Afgezien van het printen met bacteriën is het ook belangrijk voor de productie van bacteriële materialen dat de bacteriën na het printen een chemisch stabiele structuur vormen en een langere tijd levend blijven. In hoofdstuk 6 werden bacteriën 3D geprint en er toe gebracht een biofilm te vormen, een gemeenschap van cellen in een zelfgemaakte, extracellulaire matrix. Om controle over de groei van de biofilm te bereiken, werd de expressie van het *csgA* gen door een chemische stof gecontroleerd. CsgA vormt nano-vezels ("curli") die de cellen verbinden. Curli vezels zijn het belangrijkste element in de extracellulaire matrix van natuurlijke *E. coli* biofilmen. Toen CsgA door de geprinte bacteriën geproduceerd werd, bleven de gellen stabiel, zelfs toen die door een stof behandeld werden die alginaat gellen oplost. In dit hoofdstuk wordt ook een 3D printer aangetoond die uit K'NEX speeltuig delen en elekronische componenten bestaat. De "biolinker" is hedendags de goedkoopste 3D printer voor cellen en een interdisciplinair instrument voor het STEM onderwijs.

3D-geprinte biofilmen mogen een allereerste stap zijn naar de productie van grootschalige, levende materialen, die in combinatie met biomineralisatie de eigenschappen van parelmoer imiteren. Parelmoer imiterende, milieuvriendelijke materialen van goede

kwaliteit kunnen nuttig zijn in de geneeskunde, de bouwsector, en de vliegtuigbouw, dankzij hun biocompatibiliteit, betrouwbaarheid, en lage gewicht. In combinatie met genetische technologie kan het 3D printen van bacteriën tot heel nieuwe materialen voor toepassingen in wetenschap en techniek leiden.

# ACRONYMS

**ACC** amorphous calcium carbonate

**BSA** bovine serum albumin

**CFU** colony forming unit

**DC** direct current

**EDTA** ethylenediaminetetraacetic acid

**GFP** green fluorescent protein

**GMP** guanosine monophosphate

**GTP** guanosine triphosphate

**HRTEM** high resolution transmission electron microscopy

**IPTG** Isopropyl β-D-1-thiogalactopyranoside

**LB** lysogeny broth

**LbL** layer-by-layer

**MICP** microorganism-induced calcium carbonate precipitation

**MWCO** molecular weight cut-off

**OD** optical density

**PAA** poly(acrylic acid)

**PBS** phosphate-buffered saline

**PDDA** poly(diallydimethylammonium) chloride polycation

**PEG** polyethylene glycol

**PGA** γ-polyglutamate

**PHA** polyhydroxyalkanoate

**PLA** poly-lactate

**PLGA** poly(lactate-co-glycolate)

**PVP** poly(4-vinyl pyridine)

**PMMA** poly(methyl methacrylate)

**PMT** photomultiplier tube

**RFP** red fluorescent protein

**SEM** scanning electron microscopy

**TEM** transmission electron microscopy

**TGA** thermogravimetry

**TSB** tryptic soy broth

**XRD** X-ray diffraction

# 1

# INTRODUCTION

The field of biomimetics strives to adapt natural building principles for human applications. An important inspiration for new high-performance materials is nacre, the material of pearls and the inner lining of many mollusk shells. Despite consisting of mostly brittle calcium carbonate, nacre displays extraordinarily high toughness and strength, which is caused by toughening mechanisms on different length scales, such as crack deflection and strain hardening. Different approaches to create nacre-like materials are pursued, but they suffer from poor scalability, high cost, or the need for dedicated equipment. Bacteria are well-established tools in biotechnology as efficient and eco-friendly cell factories for the production of many different compounds. Nacre-inspired materials grown with bacteria could find applications in civil engineering, medicine, and aerospace engineering, while at the same time preserving natural resources and avoiding dangerous waste products.

Figure 1.1: The leaves of the sacred lotus, *Nelumbo nucifera*, are superhydrophobic due to a combination of hydrophobic waxes and a special surface microstructure. This property leads to the formation of rounded droplets of water on the leaf surface and the lotus effect.

## 1.1. BIOMIMETICS

In the course of roughly 4 billion years of evolution, nature has developed high-performance materials and structures. The field of biomimetics strives to adapt and develop the design principles found in nature for human applications, and many examples of nature-imitating materials have been developed [1, 2].

The leaves of the sacred lotus *Nelumbo nucifera* (Figure 1.1) have been known for a long time to self-clean naturally through water droplets rolling over the surface after rain or fog. This "lotus effect" [3] is caused by a combination of hydrophobic waxes and the microscopically rough surface architecture of the cuticle covering the leaves. The surface roughness results in a composite surface, consisting of wax crystalloids and air in the gaps between the crystalloids. Water spreads on a surface if the energy gained from adsorption compensates for the energy required to enlarge the surface. On surfaces showing the lotus effect, the adsorption energy is very small due to the hydrophobic surface and the air interfaces so that the energetically most favorable state water can assume is a droplet with minimum surface contact [4]. Water droplets rolling over a lotus leaf readily capture dirt particles, as the particles are usually more wettable than

Figure 1.2: The burrs of the burdock (*Arctium spec.*) have tiny hooks that allow the burrs to attach to the fur of animals and distribute the seeds (top, bottom left). The hooks have been the inspiration for the invention of Velcro (bottom right).

the cuticle, and adsorption to the droplets increases the gained adsorption energy so that re-attachment to the leaf surface is minimized [4]. Knowledge of the lotus effect is used to produce e.g. self-cleaning clothes, sails, tents, and facade paints [5].

The scales of fast-swimming sharks such as the shortfin mako shark (*Isurus oxyrinchus*) have developed to decrease the hydrodynamic drag of the animal's skin. The scales have ridges, which reduce the drag, presumably by pinning vortices generated during swimming at the scale tips, reducing the shear stress on the scale surface [6]. Shark-skin inspired surfaces are now used e.g. for swimsuits [7] or boat hulls [6]. Other examples of surface-modifications that mimic nature are anti-reflective coatings inspired by the moth-eye [8], mussel-foot-inspired peptides on titanium implant surfaces to improve attachment to bone [9], and Velcro (Figure 1.2), which was inspired by tiny hooks found on the seeds of the cocklebur (*Xanthium strumarium*) that help the seed to attach to the fur of animals [2].

While many biomimetic approaches focus on the surfaces of materials, other approaches attempt to incorporate natural abilities such as self-healing or crack-resistance

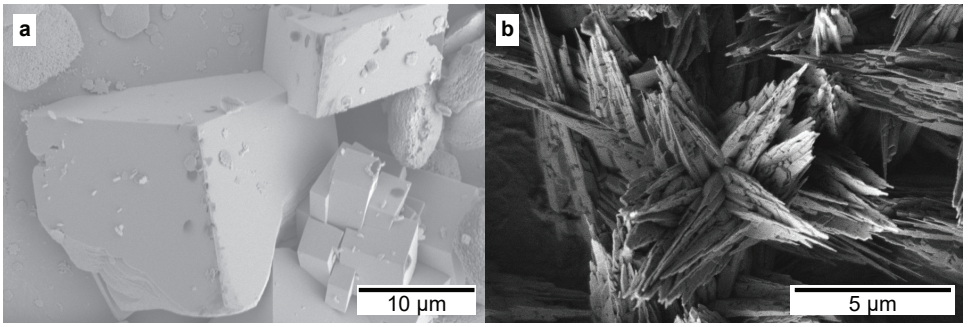


Figure 1.3: Calcium carbonate crystals grown as calcite (a) and aragonite (b) by diffusing $NH_3$ and $CO_2$ into a calcium chloride solution (Section 3.4.5). The polymorph was shifted from calcite to aragonite by addition of a 6:1 surplus of $Mg^{2+}$ to $Ca^{2+}$-ions in (b). Calcite crystals grown with this method are usually rhombohedral, while aragonite crystals display a needle shape. Biomineralization in mollusks is tightly controlled, resulting in different morphologies of both crystal types.

into bulk materials. Jonkers *et al.* [10] incorporated calcium carbonate-forming bacilli into cement to improve the clogging of micrometer-sized cracks upon ingress of water, which could potentially improve the lifetime of concrete structures. The shells of mollusks are extraordinarily strong and crack-resistant so that shell-mimicking materials have the potential to be used as long-lasting, lightweight and eco-friendly construction materials. These shells, formed by the classes Monoplacophora, Bivalvia, Gastropoda, and Scaphopoda [11], consist largely of calcium carbonate in two different crystal polymorphs: calcite and aragonite. Calcite is thermodynamically more stable than aragonite, and the crystal structures differ mainly in the position and orientation of the carbonate ions [12]. In vitro experiments show that crystallization of aragonite is favored over calcite in environments with a high $Mg^{2+}/Ca^{2+}$ ratio, as found in present-day seawater [13]. However, since mollusks maintain tight genetic control over polymorph selection, the distribution of calcite to aragonite in shells varies widely from species to species. For example, shells of the common jingle *Anomia simplex* [14] and the queen scallop *Aequipecten opercularis* are mostly calcitic [13], while shells of the common slipper shell *Crepidula fornicata* [14] and *Nautilus* are largely aragonitic [15]. A great variation in shell compositions and structures is observed, but in many cases, three distinct layers can be observed. The outer periostracum isolates the inner parts of the shell from the seawater and consists of cross-linked proteins. The middle layer consists of calcite or aragonite forming different structures, such as prisms or lamelles [15], while the innermost layer consists of aragonitic nacre (also called mother-of-pearl) [16] (Figures 1.4, 1.5a).

In this dissertation, nacre serves as inspiration for the production of new materials with the help of bacteria. In the following sections, the structure and resulting mechanical properties of nacre are discussed, as well as attempts to create nacre-mimicking materials.


Figure 1.4: Nacre (mother-of-pearl) (a) in the inner lining of the *Nautilus* shell, or (b) in form of pearls.

1

## 1.2. THE STRUCTURE OF NACRE

The nacreous layer of shells has attracted a lot of attention due to its outstanding mechanical properties: despite mostly consisting of ceramic material, it is both hard (resistant to deformation) and tough (resistant to crack formation and propagation), a combination of properties which is hard to achieve [17], since hard ceramics are usually susceptible to cracking. Nacre is comprised of about 95 wt% calcium carbonate in its aragonite conformation, while the rest of the material is made of a complex organic matrix containing large amounts of β-chitin and various proteins. Despite consisting in large parts of ceramic calcium carbonate, nacre behaves very differently from monolithic calcium carbonate. While the Young's modulus (i.e. the stiffness) of 70 GPa is comparable to pure calcium carbonate [18, 19], its toughness ($J_{IC}$ = 1.5 kJ m$^{-2}$) is estimated to be about 1000 times higher than the toughness of pure aragonite crystal [20].

The key to understanding nacre's properties lies in elucidating its composition and structure. Nacre shows a so-called "brick-and-mortar" structure: polygonal aragonite platelets with a thickness of on average 0.5 µm are embedded in the inter-crystalline matrix with a thickness of 20–50 nm between neighboring platelets [23] (Figure 1.6). On the platelet surface, tiny elevations ("asperities") of 10–30 nm diameter can be found which protrude into the inter-crystalline matrix and interpose with the asperities of the platelets below and above [24]. Furthermore, platelets are directly connected by mineral-bridges with a diameter of approximately 50 nm, which span the entire organic matrix between two platelets [18].

Interestingly, there is no final consensus about the fine structure of the aragonite tablets. In X-ray diffraction experiments, tablets appear as single crystals [25], and TEM studies have shown that the crystal orientations within one platelet are aligned [26, 27]. Nassif *et al.* [28] reported a thin layer of amorphous calcium carbonate (ACC) on the surface of *Haliotis laevigata* tablets, leading to the hypothesis that a tablet has a crystalline core which is surrounded by ACC [29]. In stark contrast to this single-crystal hypothesis stands the finding that when *Haliotis rufescens* tablets were examined by AFM, the tablets seemed to consist of nanograins with a diameter of about 32 nm [30]. In tensile tests, these nanograins were shown to deform and rotate [31].

The platelets of nacre can be arranged in two different fashions: gastropods form mainly columnar nacre, while bivalves form mostly sheet nacre (Figure 1.5b–e). In columnar nacre, the platelets are stacked in a concentric way above each other, which results in tessellated bands visible in the cross-section, and "Christmas-tree" or "stack-of-coins"-like structures in the growth areas. In sheet nacre, the platelets are stacked randomly above each other, resulting in terraces in the growth areas [21]. In nacre from animals grown in nature, relatively thick (300 nm [32]) proteinaceous meso-layers can often be found in regular intervals in the cross-sections. As these layers are absent in lab-grown animals during continuous feeding, it is assumed that they arise from growth during times of reduced calcification [32].

The components of the organic matrix of nacre can be classified by their solubility in water [22]. β-chitin is the major component of the water-insoluble fraction, forming flat sheets between the platelets [33], which are associated with hydrophobic proteins that share sequence similarities to spider silk proteins [34]. In mature nacre, these silk-like proteins are found between nacre tablets [35], but observations of growing nacre suggest

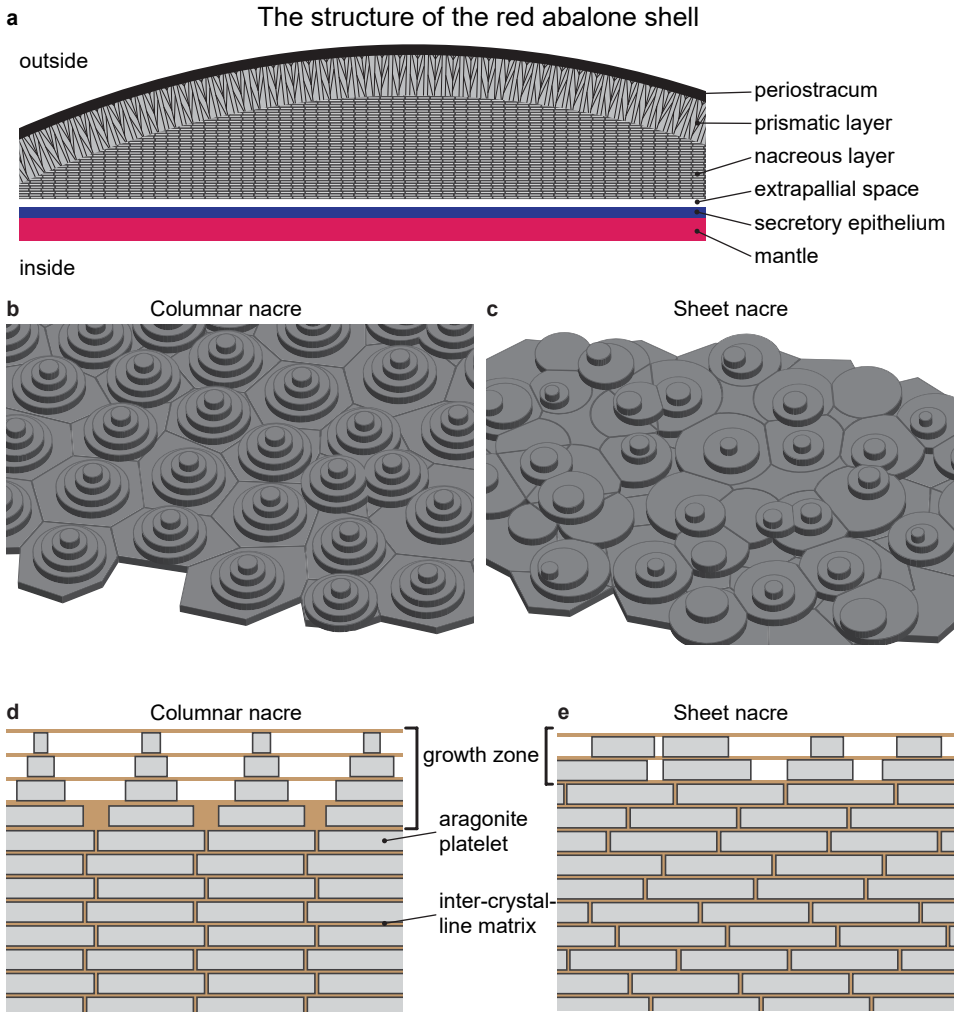


Figure 1.5: (a) The structure of the red abalone (*Haliotis rufescens*) shell [21]. (b) Top-view of growing columnar nacre, with characteristic "christmas-tree" structures that arise from the nucleation of new aragonite platelets on vertically-stacked nucleation centers. (c) Top-view of growing sheet nacre, nucleation centers are distributed randomly so that a terrace-like structure is formed. (d, e) Side-views of the growth zones of columnar and sheet nacre. Note the presence of the inter-crystalline matrix before nucleation of the new platelets [22].

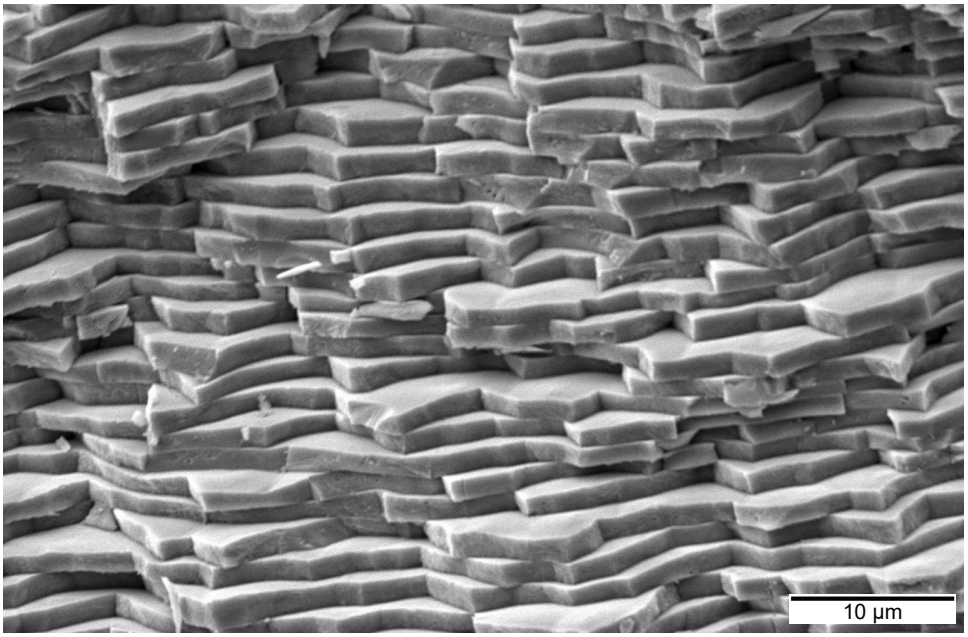


Figure 1.6: Scanning electron micrograph of blue mussel (*Mytilus edulis*) nacre (cross-section).

that they form a gel in which platelet formation takes place [33, 36]. During this process, the silk-like proteins are displaced by the newly formed calcium carbonate and accumulate in the inter-platelet space [36]. The water-soluble matrix of nacre consists of a large number of proteins, often with a high content of aspartic acid [37], which control the formation of nacre by e.g. controlling the formed calcium carbonate polymorph [11, 12]. For example, the protein n16 from *Pinctada fucata* is believed to self-aggregate during nacre growth [38] and was shown to promote the selective growth of aragonite [39].

## 1.3. THE GROWTH OF NACRE

The growth region of nacre is located in the extrapallial space between the periostracum and the secretory epithelium of the mantle [40]. Despite being a layered structure, nacre does not grow in a classical layer-by-layer fashion. Instead, TEM studies have shown that the chitin sheets of the organic matrix are present before crystallization is initiated and that tablets can nucleate and grow before the previous layer is completed ([41], Figure 1.5d, e). There are currently two models of tablet nucleation: epitaxial nucleation on an organic template, and nucleation on previous layers through mineral bridges [22].

The first evidence for the involvement of the organic matrix in crystal nucleation and morphology selection was uncovered by Watabe and Wilbur [42], who observed that de-mineralized nacre matrices that were re-inserted into the nacre growth zones would be covered by aragonite, while non-matrix samples were covered by calcite. Weiner *et al.* [35] showed that the crystallographic axes of *Nautilus* nacre's β-chitin and the *a*/*b*-axes of the aragonite tablets were aligned. In the de-mineralized organic matrix of *Nautilus*

*pompilius*, complex nucleation centers were found in the centers of the tablet imprints. These centers were shown to be rich in calcium-binding carboxylates and sulfates, as well as proteins thought to be involved in crystal nucleation [43]. Furthermore, several matrix-associated proteins were found to be important for nacre formation. The complex of the proteins Pif80 and Pif97 from *Pinctada fucata* binds to chitin fibers by means of Pif97's chitin-binding domain, while the acidic protein Pif80 attracts calcium ions and controls crystallization into aragonite [44]. A knock-down of these proteins by RNA interference resulted in the disturbed growth of the nacreous shell portion [45].

Early TEM studies of nacre of different gastropods, cephalopods, and bivalves revealed that the organic layers of nacre contain pores [46], and that nucleation of new tablets in *Pinctada radiata*, *Mytilus exustus*, and *Anomia simplex* occurred adjacent to already formed tablets when perforations in the separating layer were present [41]. In *Haliotis rufescens*, these pores had a diameter of 5–50 nm, an average spacing of 50 nm, and were found to be ion-conductive [47], leading to the hypothesis that nucleation of new tablets occurs through mineral bridges that span the organic layer. The presence of these mineral bridges was confirmed by TEM [48, 49]. Feng *et al.* [50] found with TEM studies of e.g. *Mytilus edulis* nacre that there are domains of platelets in nacre which share all three crystallographic orientations (with the *a*/*b*-axes parallel to the organic matrix layers and the *c*-axis perpendicular). These domains consisted of 3–10 tablets along the *c*-axis and 1–5 platelets in the *a*/*b*-plane. This finding suggested that domain members had nucleated from the same ancestor platelet and that the crystallographic orientation was propagated through the following generations via the mineral bridges.

The actual nucleation mechanism is probably a combination of epitaxial nucleation and nucleation through mineral bridges [22]: nucleation occurs on the matrix during *de-novo* synthesis of nacre, when no underlying platelet could furnish mineral bridges, as well as randomly during later stages of nacre growth. This mode of growth would explain why domains of platelets with aligned crystal axes only encompass a relatively small number of platelets. The hypothesis of a mixed mechanism is further supported by the finding that the degree of axis alignment is lowest in the growth regions close to the prismatic layer (where *de-novo* initiation occurs), and higher in layers further away [52].

The mixed nucleation mechanism described above would complement a hypothetic single-crystal growth mechanism where $Ca^{2+}$ and $CO_3{}^{2-}$-ions secreted from the secretory epithelium bind to the nascent aragonite crystals for enlargement. However, the transport of big numbers of ions and the subsequent removal of large volumes of water would pose significant logistical challenges to the cells of the mantle [53]. Instead, epithelial cells were found to contain vesicles with granules of amorphous calcium carbonate (ACC), which are hypothesized to be secreted into the extrapallial space instead of ions. Furthermore, mature platelets were found to have a granular nano-structure, and nascent platelets in the growth region of nacre contain high amounts of ACC, which decrease as the platelets mature [54]. The protein Pif80 is thought to play a pivotal role in the generation of aragonite platelets from ACC: by stabilizing ACC in the vesicles, assisting export into the extrapallial space, and selection of the aragonite polymorph upon calcium carbonate crystallization [44]. The exact mechanism of conversion of ACC into aragonite has not been conclusively elucidated to date [29].

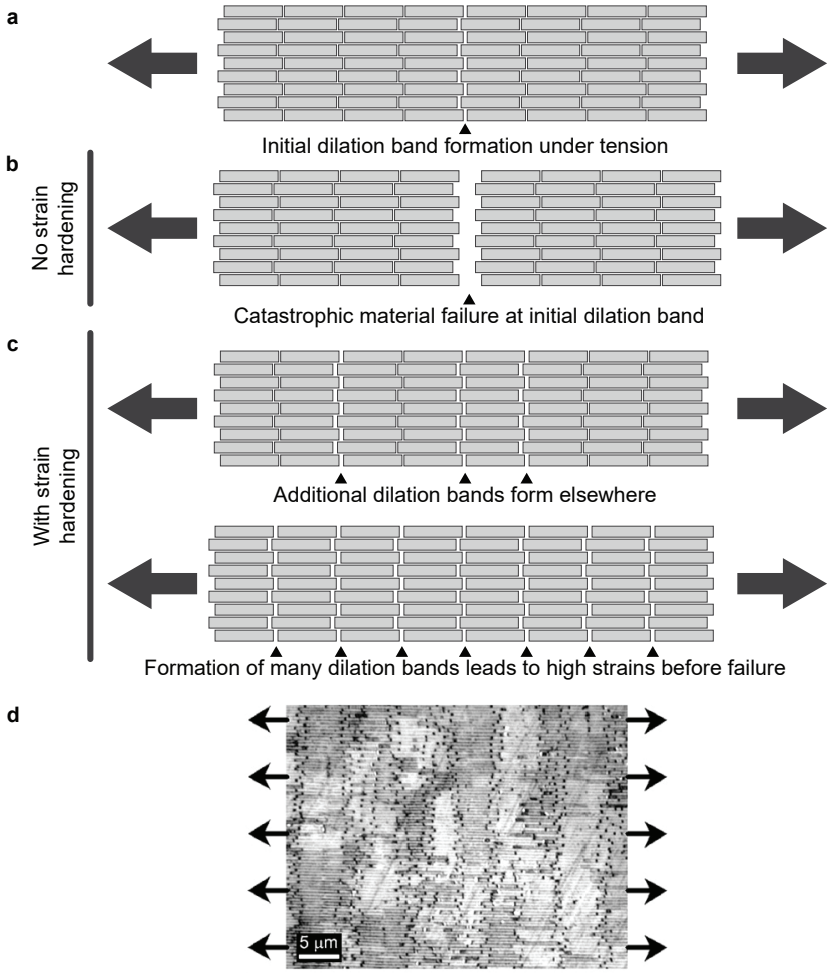


Figure 1.7: (a) When nacre is loaded in tension along the *a*/*b*-plane, platelet shifting leads to initial plastic deformation, visible as dilation band. (b) Without strain hardening mechanisms, the initially-formed dilation band would be the weakest spot of the material, leading to catastrophic failure at this place. (c) Nacre exhibits strain hardening, leading to increased force required to extend an existing dilation band. Catastrophic failure only occurs after new dilation bands have formed elsewhere so that a much higher strength and failure strain is reached. (d) SEM image of red abalone nacre in tension, showing dilation bands (Reprinted from Barthelat *et al.* [51], Copyright (2006), with permission from Elsevier).

## 1.4. TOUGHENING MECHANISMS OF NACRE

Nacre's extraordinary toughness is caused by a surprising number of toughening mechanisms across the length scales. Every component is tuned to improve the overall resistance to crack generation and propagation, providing a fascinating example of a material which surpasses human-made materials thanks to evolution and strong selective pressures over a very long time span. To understand how nacre's mechanical properties emerge from its microscopic structure, it is useful to consider a concrete example: sea otters open abalone shells by pounding the shells against rocks, often while swimming on their backs and carrying the rocks on their chest [55, 56]. This sophisticated, tool-supported behavior has likely arisen thanks to the extreme difficulty of breaking the shells. Like other ceramics, nacre has a high compressive strength and thus the compressive forces exerted on the shell can be neglected in this discussion. Due to the shape of the shell, compressive forces directed from the outside onto the mollusk translate into bending forces in the nacreous layer [57], which is important since the weak points of ceramics are the low tensile strength and the high chance of crack formation in tension. Unlike in classical ceramics, a large amount of energy is necessary to cause complete failure in nacre. When damaged nacre is examined, the cracks that were caused due to mechanical force often appear highly tortuous: the organic-inorganic interfaces of the brick-and-mortar structure act as crack barriers, deflecting the cracks and forcing a much longer crack path length [58], thus increasing the amount of work of fracture before failure of the shell as a whole. Recently, it was shown that constrained microcracks form ahead of the main crack tip, releasing local stresses and thus slowing down the propagation of the main crack [59]. However, crack deflection was deemed insufficient to explain the high toughness of nacre [60] so that additional toughening mechanisms were proposed.

When nacre was subjected to tensile tests along the plane of the layers, SEM [51] and AFM [61] showed the emergence of dilation bands: rows of gaps in the material where neighboring tablets were pulled apart. Surprisingly, an increase of the tensile forces did not result in the failure of the material at the present dilation bands—instead, new dilation bands appeared in other areas of the material. Due to the stacked arrangement in columnar nacre, this behavior resulted in tessellated bands, while the gap locations were randomly distributed in sheet nacre. These observations are a strong indicator for one of the main mechanisms of toughness generation in nacre: strain hardening, i.e. the increasing hardening of a material at higher extensions when loaded in tension (Figure 1.7). In nacre, the pulling-apart of platelets requires more and more force the more the platelets have been already been shifted. At a certain extension, the required force is so high that a new dilation band forms elsewhere instead to relieve the tension in the material, distributing the exerted energy on a much bigger volume of the material [57]. The local stresses are transferred via shear stresses in the overlap regions of the platelets [51]. The cumulative formation of many extension bands leads to a high failure strain of 1%, which is considerably larger than the usual failure strain of ceramics [51].

Several mechanisms for strain hardening have been identified, which are thought to act synergistically to produce the high toughness of nacre [62] (Figure 1.8). Under tension along the *c*-axis, the formation of ligaments between platelets that were pulled apart could be observed [63]. When an AFM probe was attached to the de-mineralized organic matrix of nacre and the required force to retract the probe from the matrix was mea-

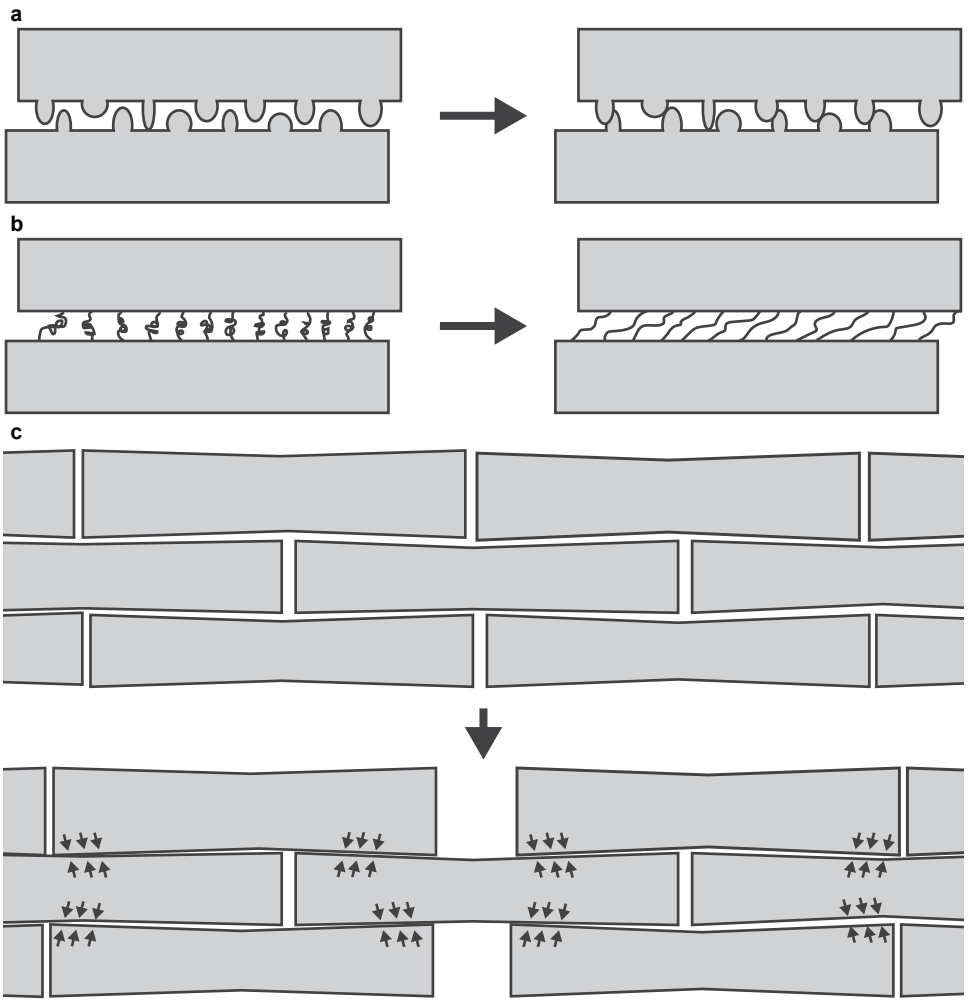


Figure 1.8: Strain hardening mechanisms in nacre. (a) Interposing nano-asperities resist platelet sliding. (b) Domains of proteins interconnecting platelets are unfolded. (c) The wavy platelet surface leads to platelet interlocking. Figure adapted from [23, 57]. Dimensions of all features are adjusted for clarity.

sured, a sawtooth-like pattern was recorded in the force-extension curve [64]. This led to the hypothesis that modular proteins connecting neighboring platelets are unfolded domain-by-domain, leading to a much higher energy absorption in tension than e.g. linear proteins [64] (Figure 1.8b). A potential candidate for a protein acting as glue between tablets is the 115 kDa protein Lustrin A, first identified in *Haliotis rufescens*, which was shown to contain repeating cysteine-rich domains [65]. These domains are thought to fold into loop-structures that allow for reversible unfolding of the protein in tension [66]. Another piece of evidence pointing towards the involvement of the organic matrix in toughening is the observation that wet nacre is considerably tougher than dry nacre. It was hypothesized that water reduces the shear modulus and the strength of the organic matrix, allowing for a more ductile overall behavior [21].

Besides the organic matrix, the geometry and composition of the tablets themselves is an important factor for improving the toughness of nacre. While the tablets are often depicted with a constant thickness, SEM micrographs of cross-sections show that the thickness varies, resulting in "surface waviness" of the platelets [57]. When platelets are pulled apart in the *a*/*b*-plane, this feature leads to interlocking when the thicker regions of neighbor platelets juxtapose, which in turn causes stress distribution to other, still un-locked regions of the shell [51, 67] (Figure 1.8c). Interposing nano-asperities [24] between nacre tablets, as well as mineral bridges directly connecting tablets [49], are thought to hinder sliding of tablets along each other [68] (Figure 1.8a). The number of asperities and mineral bridges, as well as the thickness of the individual tablets, are tuned to promote sliding instead of brittle fracture of the tablets [60, 69]. If the cracking of a tablet occurs, the crack within the tablet is deflected at the interfaces between aragonite nanograins and the intra-crystalline organic matrix [70], increasing the amount of absorbed energy upon crack propagation. Furthermore, the nanograins were shown to rotate and deform under mechanical stress conditions [31], which leads to ductile behavior of the platelet as a whole, as well as stretching of components of the intra-crystalline matrix in a rubber band-like fashion [71].

## 1.5. NACRE-MIMETIC APPROACHES

The outstanding mechanical properties of nacre have encouraged many groups to pursue research into the generation of nacre-mimicking materials for applications in e.g. engineering or medicine [72], and different approaches have been developed to produce nacre-inspired materials, all with specific advantages and challenges. Widely used methods are freeze-casting, electrophoretic deposition, and layer-by-layer assembly [62].

During freeze-casting, the freezing kinetics of water or other solvents are exploited to generate porous scaffolds with e.g. alumina slurries, which can be infused with a second phase after sublimation of the frozen agent. Due to the large number of parameters involved in the formation of the pores, such as solvents, particle sizes, freezing speed and directionality, complex experimental setups and rigid control over the experimental parameters are required [73]. Electrophoretic deposition, where an electric field guides the assembly of charged particles into layered films, was shown to be a versatile tool to generate composite structures with a variety of materials and cost-effective equipment, but optimization of the experimental parameters, to e.g. reach a satisfactory ceramic content [74], is slow and labor-intensive [75]. A production method also employed in

this work is layer-by-layer (LbL) assembly, i.e. the sequential and repeated deposition of at least two different compounds on a substrate, usually with rinsing steps in between.

Tang *et al.* [76] alternately deposited poly(diallydimethylammonium) chloride polycation (PDDA) and anionic montmorillonite clay on a glass substrate, repeating the process up to 200 times. The resulting composite film showed a layered structure in the cross-section and polygonal clay platelets arranged in a fashion reminiscent of the aragonite platelets in natural nacre. In tensile tests, the film showed initial ductility, followed by strain hardening, which was attributed to the unfolding of the PDDA chains in tension. While the ultimate tensile stress of 100 MPa was comparable to nacre, the Young's modulus and strain at failure were considerably lower, which was attributed to the higher organic content of the material, as well as the shape of the clay nanoparticles, which lacked features such as asperities or surface waviness.

Finnemore *et al.* [77] developed an LbL process for artificial nacre which reproduces several features of natural nacre. A glass substrate was immersed alternately in a solution of poly(acrylic acid) (PAA) and poly(4-vinyl pyridine) (PVP). The resulting film was functionalized by treatment with pH 10 solution, which dissolved the PAA and led to nanopore formation, and stabilized by UV-cross-linking. With the help of a gas diffusion method, amorphous calcium carbonate was generated in the film, which was subsequently crystallized to calcite. The resulting material showed layered structures comparable to nacre and even displayed iridescence. Domains with aligned crystal orientations across the organic matrix suggested the presence of mineral bridges. Compared to single crystal calcite, the artificial nacre showed improved toughness.

Gao *et al.* [78] produced nacre-mimetic films by evaporating water from a suspension of calcium phosphate platelets in an alginate solution. Many such films were glued together with chitosan, cross-linked with $CaCl_2$-solution, and hot-pressed, resulting in a layered bulk material displaying toughening mechanisms such as crack deflection and crack branching.

LbL approaches give tight spatial and temporal control over the formation process, but face a number of challenges so far [72], such as poor mechanical properties, gain of toughness only at the loss of strength and rigidity, low mineral content, requirement for dedicated equipment, and extensive energy input. By imitating growth processes occurring in organisms, these challenges might be overcome.

## 1.6. RESEARCH OBJECTIVES AND DISSERTATION OUTLINE

Due to the selective pressures in their ecological niches, mollusks are able to produce nacre from easily attainable, natural components. The expenditure of energy is relatively low and nacre growth can occur in ambient temperatures. Production methods that not only result in the successful reproduction of nacre's superior mechanical properties, but which also mimic the environmentally-friendly production process, could be a great asset for fields such as medicine, space exploration, or civil and aerospace engineering. Since nacre is produced by cells as a result of the execution of a genetic program, attempts to produce nacre-mimicking materials could also make use of cells and the tools of modern biology. However, to date it is challenging to use eukaryotic cells for bio-engineering purposes. In contrast, bacteria are used extensively in biotechnology as robust, easy-to-manipulate, and efficient microfactories for the production of diverse

compounds and materials. Consequently, the research objective of this study is:

**To investigate if bacteria can be used to produce nacre-inspired materials, mimicking both some of the morphological and mechanical features, while maintaining an eco-friendly production method.**

The research questions in particular are:

1. **Can bacterial products be combined to produce a new composite material that shares morphological features with nacre?**

   In Chapter 2, a calcium carbonate-polyglutamate material is presented that was produced with bacteria in a simple layer-by-layer production process. This "bacterial nacre" shares the inorganic-organic composite approach with nacre and displays comparable layered structures.

2. **Does this composite show improved mechanical properties compared to its constituents, and if yes, what are probable mechanisms?**

   Chapter 3 demonstrates that bacterial nacre shows a four-fold higher toughness and nearly two-fold higher strain at failure compared to pure calcium carbonate materials as a result of a distinct cracking behavior.

3. **Can bacteria be arranged efficiently and in a cost-effective way in a 3D space, while maintaining metabolic activity and the possibility of external control?**

   Natural nacre is produced by a specialized tissue under tight spatio-temporal control, which is difficult to achieve with single-cell organisms such as bacteria. A method for the controlled patterning of bacteria in 3D space could improve control over the production of bacterial nacre considerably and allow for a more time-efficient scale-up to the macroscale. Chapter 4 provides an overview over techniques to pattern bacteria. Chapter 5 introduces a method for 3D printing layered structures with bacteria-infused bioink and a cost-effective 3D printer for cells.

4. **Can control of biofilm formation be used to stabilize bacteria in 3D-printed hydrogels towards the production of organic matrices for bioengineering applications?**

   The aragonite platelets of nacre grow in a pre-formed organic matrix, which guides and controls nacre growth. Bacterially-produced matrices could assist in the production of new biomaterials. Biofilms are aggregates of bacterial cells, stabilized by an extracellular matrix. Chapter 6 presents a method for controlling the formation of *E. coli* biofilms in 3D printed structures as a proof-of-principle towards that direction.

## REFERENCES

[1] B. Bhushan, *Biomimetics: lessons from nature–an overview,* Philosophical Transactions of the Royal Society A: Mathematical, Physical and Engineering Sciences **367**, 1445 (2009).

[2] J. Hwang, Y. Jeong, J. M. Park, K. H. Lee, J. W. Hong, and J. Choi, *Biomimetics: forecasting the future of science, engineering, and medicine,* International Journal of Nanomedicine **10**, 5701 (2015).

[3] P. Roach, N. J. Shirtcliffe, and M. I. Newton, *Progess in superhydrophobic surface development,* Soft Matter **4**, 224 (2008).

[4] W. Barthlott and C. Neinhuis, *Purity of the sacred lotus, or escape from contamination in biological surfaces,* Planta **202**, 1 (1997).

[5] P. Forbes, *Self-cleaning materials,* Scientific American **299**, 88 (2008).

[6] G. D. Bixler and B. Bhushan, *Fluid drag reduction with shark-skin riblet inspired microstructured surfaces,* Advanced Functional Materials **23**, 4507 (2013).

[7] K. Krieger, *Do pool sharks swim faster?* Science **305**, 636 (2004).

[8] R. Brunner, O. Sandfuchs, C. Pacholski, C. Morhard, and J. Spatz, *Lessons from nature: biomimetic subwavelength structures for high-performance optics,* Laser & Photonics Reviews **6**, 641 (2012).

[9] H. Zhao, Y. Huang, W. Zhang, Q. Guo, W. Cui, Z. Sun, D. Eglin, L. Liu, G. Pan, and Q. Shi, *Mussel-inspired peptide coatings on titanium implant to improve osseointegration in osteoporotic condition,* ACS Biomaterials Science & Engineering **4**, 2505 (2018).

[10] H. M. Jonkers, A. Thijssen, G. Muyzer, O. Copuroglu, and E. Schlangen, *Application of bacteria as self-healing agent for the development of sustainable concrete,* Special Issue: BioGeoCivil Engineering **36**, 230 (2010).

[11] F. Marin and G. Luquet, *Molluscan shell proteins,* Biomineralisation: Diversité et unité **3**, 469 (2004).

[12] G. Falini, S. Albeck, S. Weiner, and L. Addadi, *Control of aragonite or calcite polymorphism by mollusk shell macromolecules,* Science **271**, 67 (1996).

[13] A. G. Checa, C. Jiménez-López, A. Rodríguez-Navarro, and J. P. Machado, *Precipitation of aragonite by calcitic bivalves in mg-enriched marine waters,* Marine Biology **150**, 819 (2007).

[14] O. H. Pikey and H. G. Goodell, *Trace elements in recent mollusk shells,* Limnology and Oceanography **8**, 137 (1963).

[15] J. D. Currey and J. D. Taylor, *The mechanical behaviour of some molluscan hard tissues,* Journal of Zoology **173**, 395 (1974).

[16] C. M. Zaremba, A. M. Belcher, M. Fritz, Y. Li, S. Mann, P. K. Hansma, D. E. Morse, J. S. Speck, and G. D. Stucky, *Critical transitions in the biofabrication of abalone shells and flat pearls,* Chem. Mater. **8**, 679 (1996).

[17] R. O. Ritchie, *The conflicts between strength and toughness,* Nature Materials **10**, 817 EP (2011).

[18] F. Song, A. K. Soh, and Y. L. Bai, *Structural and mechanical properties of the organic matrix layers of nacre,* Biomaterials **24**, 3623 (2003).

[19] A. P. Jackson, Vincent, J. F. V., and R. M. Turner, *The mechanical design of nacre,* (1988).

[20] N. S. Al-Maskari, D. A. McAdams, and J. N. Reddy, *Modeling of a biological material nacre: Waviness stiffness model,* Materials Science and Engineering: C **70**, 772 (2017).

[21] J. Sun and B. Bhushan, *Hierarchical structure and mechanical properties of nacre: a review,* RSC Advances **2**, 7617 (2012).

[22] F. Nudelman, *Nacre biomineralisation: A review on the mechanisms of crystal nucleation,* Biomineralisation & Motorisation of pathogens **46**, 2 (2015).

[23] M. A. Meyers, A. Y.-M. Lin, P.-Y. Chen, and J. Muyco, *Mechanical strength of abalone nacre: Role of the soft organic layer,* Journal of the Mechanical Behavior of Biomedical Materials **1**, 76 (2008).

[24] R. Z. Wang, Z. Suo, A. G. Evans, N. Yao, and I. A. Aksay, *Deformation mechanisms in nacre,* Journal of Materials Research **16**, 2485 (2001).

[25] Q. L. Feng, H. B. Li, F. Z. Cui, H. D. Li, and T. N. Kim, *Crystal orientation domains found in the single lamina in nacre of the mytilus edulis shell,* Journal of Materials Science Letters **18**, 1547 (1999).

[26] M. Rousseau, X. Bourrat, P. Stempflé, M. Brendlé, and E. Lopez, *Multi-scale structure of the pinctada mother of pearl: Demonstration of a continuous and oriented organic framework in a natural ceramic,* Key Engineering Materials **284-286**, 705 (2005).

[27] M. Rousseau, E. Lopez, P. Stempflé, M. Brendlé, L. Franke, A. Guette, R. Naslain, and X. Bourrat, *Multiscale structure of sheet nacre,* Biomaterials **26**, 6254 (2005).

[28] N. Nassif, N. Pinna, N. Gehrke, M. Antonietti, C. Jäger, and H. Cölfen, *Amorphous layer around aragonite platelets in nacre,* Proceedings of the National Academy of Sciences of the United States of America **102**, 12653 (2005).

[29] G. Zhang and J. Xu, *From colloidal nanoparticles to a single crystal: New insights into the formation of nacre's aragonite tablets,* JSB 50th Anniversary Issue **182**, 36 (2013).

[30] X. Li, W.-C. Chang, Y. J. Chao, R. Wang, and M. Chang, *Nanoscale structural and mechanical characterization of a natural nanocomposite material: The shell of red abalone,* Nano Lett **4**, 613 (2004).

[31] X. Li, Z.-H. Xu, and R. Wang, *In situ observation of nanograin rotation and deformation in nacre,* Nano Lett **6**, 2301 (2006).

[32] A. Lin and M. A. Meyers, *Growth and structure in abalone shell,* Materials Science and Engineering: A **390**, 27 (2005).

[33] Y. Levi-Kalisman, G. Falini, L. Addadi, and S. Weiner, *Structure of the nacreous organic matrix of a bivalve mollusk shell examined in the hydrated state using cryotem,* JSB 50th Anniversary Issue **135**, 8 (2001).

[34] S. Sudo, T. Fujikawa, T. Nagakura, T. Ohkubo, K. Sakaguchi, M. Tanaka, K. Nakashima, and T. Takahashi, *Structures of mollusc shell framework proteins,* Nature **387**, 563 (1997).

[35] S. Weiner, W. Traub, and S. B. Parker, *Macromolecules in mollusc shells and their functions in biomineralization [and discussion],* Philosophical Transactions of the Royal Society B: Biological Sciences **304**, 425 (1984).

[36] F. Nudelman, E. Shimoni, E. Klein, M. Rousseau, X. Bourrat, E. Lopez, L. Addadi, and S. Weiner, *Forming nacreous layer of the shells of the bivalves atrina rigida and pinctada margaritifera: an environmental- and cryo-scanning electron microscopy study,* Journal of Structural Biology **162**, 290 (2008).

[37] S. Weiner, *Aspartic acid-rich proteins: Major components of the soluble organic matrix of mollusk shells,* Calcified Tissue Research **29**, 163 (1979).

[38] G. O. Rutter, A. H. Brown, D. Quigley, T. R. Walsh, and M. P. Allen, *Emergence of order in self-assembly of the intrinsically disordered biomineralisation peptide n16n,* Molecular Simulation **44**, 463 (2018).

[39] E. C. Keene, J. S. Evans, and L. A. Estroff, *Matrix interactions in biomineralization: Aragonite nucleation by an intrinsically disordered nacre polypeptide, n16n, associated with a beta-chitin substrate,* Crystal Growth & Design **10**, 1383 (2010).

[40] F. Heinemann, M. Launspach, K. Gries, and M. Fritz, *Gastropod nacre: Structure, properties and growth — biological, chemical and physical basics,* Biophysical Chemistry **153**, 126 (2011).

[41] G. Bevelander and H. Nakahara, *An electron microscope study of the formation of the nacreous layer in the shell of certain bivalve molluscs,* Calcified Tissue Research **3**, 84 (1969).

[42] N. Watabe and K. M. Wilbur, *Influence of the organic matrix on crystal type in molluscs,* Nature **188**, 334 (1960).

[43] F. Nudelman, B. A. Gotliv, L. Addadi, and S. Weiner, *Mollusk shell formation: mapping the distribution of organic matrix components underlying a single aragonitic tablet in nacre,* JSB 50th Anniversary Issue **153**, 176 (2006).

[44] S. Y. Bahn, B. H. Jo, Y. S. Choi, and H. J. Cha, *Control of nacre biomineralization by pif80 in pearl oyster,* Science Advances **3** (2017), 10.1126/sciadv.1700765.

[45] M. Suzuki, K. Saruwatari, T. Kogure, Y. Yamamoto, T. Nishimura, T. Kato, and H. Nagasawa, *An acidic matrix protein, pif, is a key macromolecule for nacre formation,* Science **325**, 1388 (2009).

[46] C. Grégoire, *Topography of the organic components in mother-of-pearl,* The Journal of Biophysical and Biochemical Cytology **3**, 797 (1957).

[47] T. E. Schäffer, C. Ionescu-Zanetti, R. Proksch, M. Fritz, D. A. Walters, N. Almqvist, C. M. Zaremba, A. M. Belcher, B. L. Smith, G. D. Stucky, D. E. Morse, and P. K. Hansma, *Does abalone nacre form by heteroepitaxial nucleation or by growth through mineral bridges?* Chemistry of Materials **9**, 1731 (1997).

[48] F. Song, X. H. Zhang, and Y. L. Bai, *Microstructure and characteristics in the organic matrix layers of nacre,* Journal of Materials Research **17**, 1567 (2002).

[49] A. G. Checa, J. H. E. Cartwright, and M.-G. Willinger, *Mineral bridges in nacre,* Journal of Structural Biology **176**, 330 (2011).

[50] Q. L. Feng, F. Z. Cui, G. Pu, R. Z. Wang, and H. D. Li, *Crystal orientation, toughening mechanisms and a mimic of nacre,* Materials Science and Engineering: C **11**, 19 (2000).

[51] F. Barthelat, H. Tang, P. D. Zavattieri, C.-M. Li, and H. D. Espinosa, *On the mechanics of mother-of-pearl: A key feature in the material hierarchical structure,* Journal of the Mechanics and Physics of Solids **55**, 306 (2007).

[52] P. U. Gilbert, R. A. Metzler, D. Zhou, A. Scholl, A. Doran, A. Young, M. Kunz, N. Tamura, and S. N. Coppersmith, *Gradual ordering in red abalone nacre,* Journal of the American Chemical Society **130**, 17519 (2008).

[53] L. Addadi, D. Joester, F. Nudelman, and S. Weiner, *Mollusk shell formation: A source of new concepts for understanding biomineralization processes,* Chemistry – A European Journal **12**, 980 (2006).

[54] E. Macías-Sánchez, M. G. Willinger, C. M. Pina, and A. G. Checa, *Transformation of acc into aragonite and the origin of the nanogranular structure of nacre,* Scientific Reports **7**, 12728 (2017).

[55] K. R. L. Hall and G. B. Schaller, *Tool-using behavior of the california sea otter,* Journal of Mammalogy **45**, 287 (1964).

[56] J. A. Estes and J. F. Palmisano, *Sea otters: their role in structuring nearshore communities,* Science (New York, N.Y.) **185**, 1058 (1974).

[57] F. Barthelat and H. D. Espinosa, *An experimental investigation of deformation and fracture of nacre–mother of pearl,* Experimental Mechanics **47**, 311 (2007).

[58] K. K. Chawla and M. A. Meyers, *Mechanical behavior of materials* (Prentice Hall, 1999).

[59] J. Song, C. Fan, H. Ma, L. Liang, and Y. Wei, *Crack deflection occurs by constrained microcracking in nacre,* Acta Mechanica Sinica **34**, 143 (2018).

[60] M. A. Meyers, P.-Y. Chen, A. Y.-M. Lin, and Y. Seki, *Biological materials: Structure and mechanical properties,* Progress in Materials Science **53**, 1 (2008).

[61] R. Rabiei, S. Bekah, and F. Barthelat, *Failure mode transition in natural mineralized composites,* MRS Proceedings **1301** (2011), 10.1557/opl.2011.564.

[62] J. Wang, Q. Cheng, and Z. Tang, *Layered nanocomposites inspired by the structure and mechanical properties of nacre,* Chemical Society Reviews **41**, 1111 (2012).

[63] G. Mayer and M. Sarikaya, *Rigid biological composite materials: Structural examples for biomimetic design,* Experimental Mechanics **42**, 395 (2002).

[64] B. L. Smith, T. E. Schaffer, M. Viani, J. B. Thompson, N. A. Frederick, J. Kindt, A. Belcher, G. D. Stucky, D. E. Morse, and P. K. Hansma, *Molecular mechanistic origin of the toughness of natural adhesives, fibres and composites,* Nature **399**, 761 (1999).

[65] X. Shen, A. M. Belcher, P. K. Hansma, G. D. Stucky, and D. E. Morse, *Molecular cloning and characterization of lustrin a, a matrix protein from shell and pearl nacre of haliotis rufescens,* Journal of Biological Chemistry **272**, 32472 (1997).

[66] B. Zhang, B. A. Wustman, D. Morse, and J. S. Evans, *Model peptide studies of sequence regions in the elastomeric biomineralization protein, lustrin a. i. the c-domain consensus-pg-, -nvnct-motif,* Biopolymers **63**, 358 (2002).

[67] H. D. Espinosa, A. L. Juster, F. J. Latourte, O. Y. Loh, D. Gregoire, and P. D. Zavattieri, *Tablet-level origin of toughening in abalone shells and translation to synthetic composite materials,* Nature communications **2**, 173 (2011).

[68] A. G. Evans, Z. Suo, R. Z. Wang, I. A. Aksay, He, M. Y., and Hutchinson, J. W., *Model for the robust mechanical behavior of nacre,* Journal of Materials Research **16**, 2475 (2001).

[69] H. Gao, B. Ji, I. L. Jäger, E. Arzt, and P. Fratzl, *Materials become insensitive to flaws at nanoscale: Lessons from nature,* Proceedings of the National Academy of Sciences **100**, 5597 (2003).

[70] S. Wang, X. Zhu, Q. Li, R. Wang, and X. Wang, *Damage-tolerance strategies for nacre tablets,* Journal of Structural Biology **194**, 199 (2016).

[71] X. Li, *Nanoscale structural and mechanical characterization of natural nanocomposites: Seashells,* The Journal of The Minerals **59**, 71 (2007).

[72] J. R. Rodrigues, N. M. Alves, and J. F. Mano, *Nacre-inspired nanocomposites produced using layer-by-layer assembly: Design strategies and biomedical applications,* Materials Science and Engineering: C **76**, 1263 (2017).

[73] S. Deville, *Freeze–casting of porous ceramics: A review of current achievements and issues,* Advanced Engineering Materials **10**, 155 (2008).

[74] B. Long, C.-A. Wang, W. Lin, Y. Huang, and J. Sun, *Polyacrylamide-clay nacre-like nanocomposites prepared by electrophoretic deposition,* Composites Science and Technology **67**, 2770 (2007).

[75] A. R. Boccaccini, S. Keim, R. Ma, Y. Li, and I. Zhitomirsky, *Electrophoretic deposition of biomaterials,* Journal of The Royal Society Interface **7**, S581 (2010).

[76] Z. Tang, N. A. Kotov, S. Magonov, and B. Ozturk, *Nanostructured artificial nacre,* Nature Materials **2**, 413 (2003).

[77] A. Finnemore, P. Cunha, T. Shean, S. Vignolini, S. Guldin, M. Oyen, and U. Steiner, *Biomimetic layer-by-layer assembly of artificial nacre,* Nature Communications **3**, 966 (2012).

[78] H.-L. Gao, S.-M. Chen, L.-B. Mao, Z.-Q. Song, H.-B. Yao, H. Cölfen, X.-S. Luo, F. Zhang, Z. Pan, Y.-F. Meng, Y. Ni, and S.-H. Yu, *Mass production of bulk artificial nacre with excellent mechanical properties,* Nature Communications **8**, 287 (2017).

# 2

# USING BACTERIA TO MAKE IMPROVED, NACRE-INSPIRED MATERIALS

**Dominik T. SCHMIEDEN, Anne S. MEYER and Marie-Eve AUBIN-TAM**

Nacre (mother-of-pearl) is an attractive model for the development of new materials. Its sheet structure of alternating layers of calcium carbonate and an organic matrix confers it highly desirable properties such as high toughness and strength. In this study, we produce a nacre-inspired composite material using only bacterially-produced components. Calcium carbonate is crystallized via the action of ureolytic bacteria. After each crystallization event, we apply bacterially produced $\gamma$-polyglutamate (PGA) to the sample, which promotes layering compared to the PGA-free control. We show that the combination of these two compounds yields a layered material reminiscent of nacre, showing a way towards the biotechnological production of new, nacre-inspired materials.

Parts of this chapter have been published in MRS Advances 1, 559 (2016) [1].

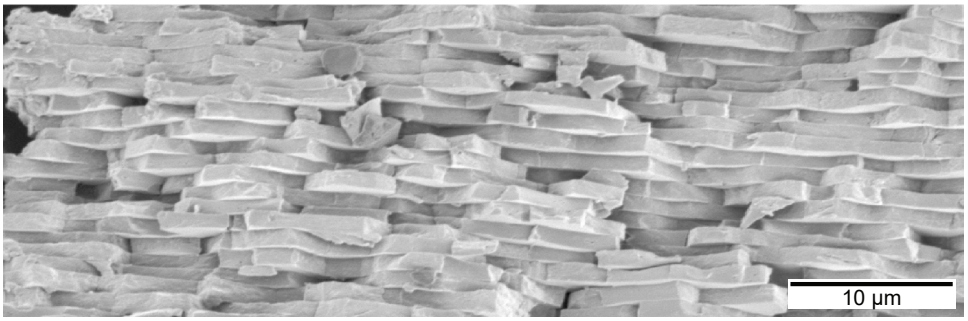


Figure 2.1: SEM picture of blue mussel (*Mytilus edulis*) nacre.

## 2.1. INTRODUCTION

Mollusks have developed hard shells as protection against predators. The inner layer of many of these shells is nacre (mother-of-pearl), a composite material consisting of layers of aragonite (calcium carbonate) platelets interconnected by a complex organic matrix (Figure 2.1). The calcium carbonate layers have in many cases a thickness of 0.3–0.5 µm, depending on the animal species, while the organic matrix reaches only 20–30 nm [2]. Even though nacre consists of 95% calcium carbonate, its mechanical properties differ dramatically from monolithic calcium carbonate, e.g. with a much higher fracture toughness and strength (reviewed by Sun and Bhushan [3]). These highly desirable mechanical properties have inspired a great deal of research into the production of nacre-like composite materials (reviewed by Wang *et al.* [4], Corni *et al.* [5]), using techniques ranging from freeze-casting [6] to self-assembly of nanoclays [7]. In this study, we aim at laying the foundation for producing nacre-inspired composite materials with the aid of bacteria. Bacteria offer a wide range of metabolic products, are readily accessible to genetic engineering, and are efficient and environmentally-friendly tools for the production of various compounds. For the production of nacre-like compounds, at least two building blocks are required: calcium carbonate layers and a connecting matrix.

Bacteria have been associated with carbonate deposition in diverse habitats including sea water, saline lakes, soils, and geological formations [8]. One mechanism of bacterially-induced calcium carbonate formation is the breakdown of urea by ureolytic bacteria such as *Sporosarcina pasteurii*. The ensuing formation of ammonia and carbonate increases the ambient pH, causing calcium to fall out of solution as crystalline calcium carbonate. The use of *S. pasteurii* to produce calcium carbonate has been demonstrated in laboratory settings for applications such as soil improvement and biogrouting [9, 10] or repair of cracks in concrete [11]. This ureolytic activity can be transferred into the model organism *Escherichia coli* by genetic engineering [12], making it an attractive candidate for synthetic biology projects.

$\gamma$-Polyglutamate (PGA) is an exo-polymer produced by many members of the *Bacillus* genus that serves e.g. as protection against the immune system [13]. Thanks to its unusual $\gamma$-linkage, it is resistant to proteases [14]. PGA has evoked considerable interest in industrial applications, as it is non-toxic, non-immunogenic, biodegradable, edible, and water soluble [15]. Cationic polymeric substances such as polyaspartate have

been demonstrated to promote the formation of calcium carbonate thin-films on a chitosan substrate, where their negatively charged carboxyl groups serve as binding sites for calcium ions [16]. In this study, we employ PGA as a mimic for the organic matrix of nacre, expecting that PGA might show a calcium carbonate templating function similar to polyaspartate, while being easy to produce from natural producers or transgenic organisms [17, 18].



The aim of this study is to investigate whether the combination of calcium carbonate and PGA can produce a layered, nacre-like material, which would open the door for the development of transgenic microorganisms for the production of new composite materials in an easy and environmentally friendly manner.

## 2.2. RESULTS AND DISCUSSION

The aim of this study was to generate a nacre-inspired compound material using only bacterially-produced materials. To achieve this, we subjected glass slides to 23 calcium carbonate crystallization cycles by *S. pasteurii*. After each crystallization cycle, a subset of slides was coated with 0.5 mg cm$^{-2}$ of microbially-produced PGA. The other set of samples received no PGA between calcium carbonate crystallization events, serving as a negative control.

Various features of PGA-containing samples were analyzed. Macroscopic investigation showed that the slides were densely covered with deposited material (Figure 2.2a). Cavities were observed under large areas of the material, leading to detachment of flakes. Scanning electron microscopy (SEM) of top views (Figure 2.2b) revealed a seemingly random arrangement of crystals of different morphologies, suggesting the presence of primarily spherical vaterite, but also rhombohedral calcite and vaterite-calcite intermediates.

SEM images of cross-sections of the PGA-containing material showed layered structures in about 40% of the cross-sectional area, either forming a relatively flat, layered sheet on the substrate, or as internal structures of spherical crystals (Figure 2.2c). Layers were observed mostly at the edges of the slide. Here, also the overall material thickness was highest. The central regions of the slide showed a base layer of calcium carbonate with crystals of various shapes protruding from it (Figure 2.2d). When layering occurred here, it was restricted to spherical crystals. No organic material could be detected between layers of calcium carbonate, thus any layer of PGA would have a thickness of below 50 nm.

PGA-free samples showed an altered morphology. Macroscopically, we observed good coverage of calcium carbonate that was strongly bound to the surface, though with some rough areas with inhomogeneous coverage in the center of the slide (Figure 2.2e). As in PGA-containing samples, the main crystal morphology was spherical vaterite (Figure 2.2f). SEM on cross-sections of the samples showed either single crystals or, as in the central region of PGA-containing samples, a base layer of calcium carbonate with crystals protruding from it (Figure 2.2g). This base layer generally did not contain obvious internal structures, but regions of spherical crystals often had an inner structure that contained 3–10 layers (Figure 2.2h). Layers stretched over a much smaller overall width of the cross-section than in PGA-containing samples (Table 2.1) and were absent in regions outside of spherical crystals.

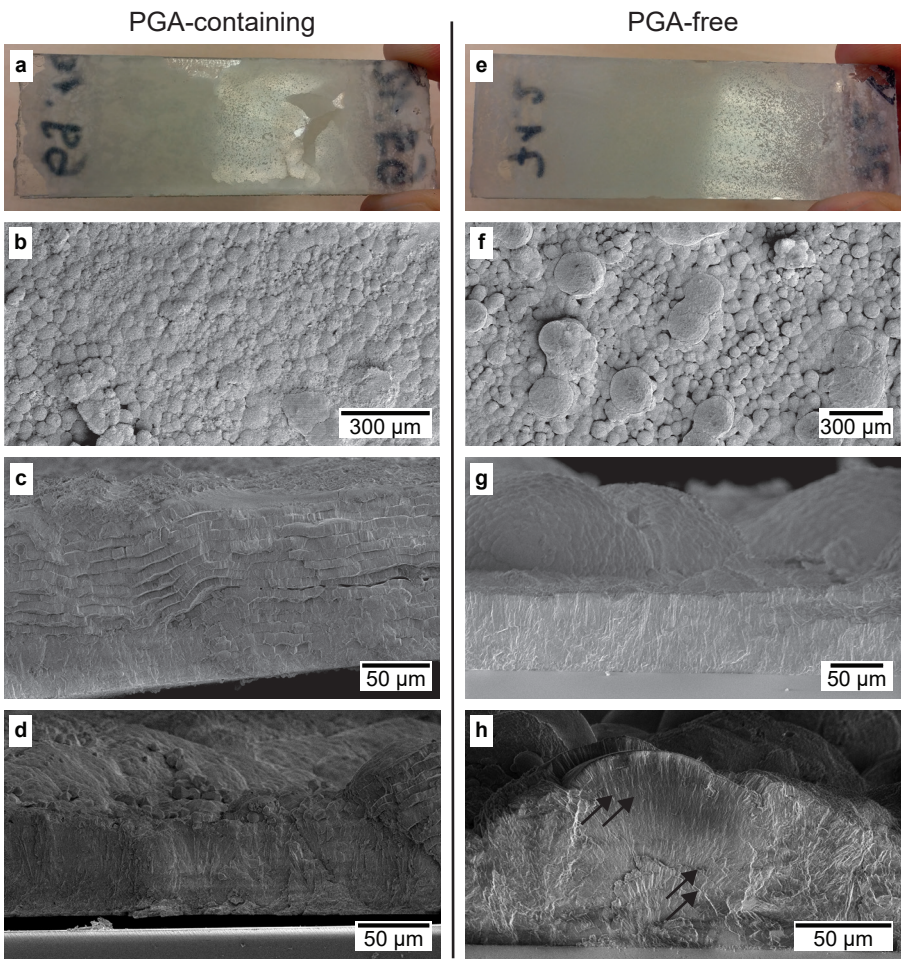


Figure 2.2: **a-d:** Glass slides covered with $CaCO_3$, crystallized 23 times on the slide via the action of ureolytic *S. pasteurii*. After each crystallization event, 0.5 mg cm$^{-2}$ PGA was dried on the slide **e–h:** Samples prepared as in a–d, but without PGA application **a, e:** Macroscopic view after polishing **b, f:** SEM pictures of top views **c, d, g, h:** SEM pictures of cross-sections, c and h showing layered, d and g showing un-layered areas. Boundaries between individual layers are marked with arrows in panel h.

Layers in PGA-containing samples had an average thickness of 6 ± 1 µm (SD), while layers in PGA-free samples were 8 ± 1 µm thick. These layers are 5–20 times thicker than calcium carbonate layers in nacre, which have a typical thickness of 0.3–0.5 µm [2]. These thicker layers may result in a lower fracture strength in comparison to natural nacre [19].



Table 2.1: Estimated proportion of layered structures in cross-sections of four samples

| Sample | Layered |
|---|---|
| PGA-free 1 | 10% |
| PGA-free 2 | 8% |
| PGA-containing 1 | 37% |
| PGA-containing 2 | 42% |

## 2.3. CONCLUSION

We have shown that PGA promotes formation of layers resembling nacre in experiments with repeated crystallization of calcium carbonate, allowing the production of a layered composite material exclusively made with bacterial products. This research could lead to the development of new, biotechnologically-produced, nacre-like materials with potential applications in engineering or medicine.

## 2.4. METHODS

Chemicals were purchased from VWR Netherlands or Sigma Aldrich Netherlands unless otherwise indicated. Bacterial cultures were grown in rotary shakers with temperature control at 180 rpm unless otherwise indicated.

### 2.4.1. SUBSTRATE PREPARATION

Microscope slides (Corning 2947, 75 × 25 × 1 mm) were used as substrates for material deposition. Since calcium carbonate does not crystallize as a film on glass, the slides were covered with a calcium carbonate thin-film as in Sugawara and Kato [16] for the first crystallization event. A solution of 1% w/v chitosan (Sigma 448877, medium mol. weight, 75–85% deacetylation) in 1% v/v acetic acid was spin-coated on the microscope slides, dried for 10–30 min at 60 °C, neutralized with 0.1% w/v NaOH solution, rinsed with MilliQ water, and air-dried with a flow of nitrogen gas. The slide was then placed downwards-facing, on two magnetic stirrer bars as supports, into a Petri dish containing a solution of 30 mM $CaCl_2$, 90 mM $MgCl_2$, and 0.005% w/v polyacrylic acid (avg. Mw 2100 g mol$^{-1}$). The dish and a beaker containing 50 g $(NH_4)HCO_3$ were placed in a 5 L closed desiccator and incubated for 3 days at room temperature, allowing a thin film of calcium carbonate to form on the chitosan. Afterwards, the slide was removed from the solution, rinsed with MilliQ water, dried with a flow of nitrogen gas, and used as a substrate for the subsequent crystallization experiments.

### 2.4.2. PGA PRODUCTION AND ISOLATION

*Bacillus licheniformis* NBRC12107 (ATCC 9945a) was purchased from the Biological Resource Center, National Institute of Technology and Evaluation (Japan) and cultured in BL-medium (10 g$L^{-1}$ peptone, 2 g$L^{-1}$ yeast extract, 2 g$L^{-1}$ $MgSO_4 \cdot 7H_2O$, sterilized by autoclaving) overnight at 30 °C for starter cultures and glycerol stock cultures.

For production of PGA, Medium E [20] (20 g$L^{-1}$ L-glutamic acid, 13.6 g$L^{-1}$ monosodium citrate, 80 g$L^{-1}$ glycerol, 7 g$L^{-1}$ $NH_4Cl$, 0.5 g$L^{-1}$ $KH_2PO_4$, 0.244 g$L^{-1}$ $MgSO_4$, 0.04 g$L^{-1}$ $FeCl_3 \cdot 6H_2O$, 0.15 g$L^{-1}$ $CaCl_2 \cdot 2H_2O$, 0.1 g$L^{-1}$ $MnSO_4 \cdot H_2O$, pH 7.5 with NaOH, sterilized by autoclaving) was inoculated with 1.5% starter culture and cultured at 30 °C for around 2 days until formation of a viscous fluid. The following steps were performed at 4–8 °C wherever possible. The bacteria culture was centrifuged for 30 min at 8200 × *g*, and PGA was precipitated from the supernatant by addition of 0.3–0.4 M $CuSO_4$ [21]. The solution was centrifuged for 10 min at 8200 × *g* and the sediment re-dissolved in 0.5 M EDTA (pH 8 with NaOH). Copper-EDTA complexes were removed by dialysis with Spectra/Por 2 Dialysis Tubing, 12–14 kDa MWCO (Spectrum Europe B.V., The Netherlands) against MilliQ water. The dialyzed PGA solution was centrifuged for 20 min at 8200 × *g* to remove any solid residue, frozen at 20 °C, and freeze-dried. The resulting PGA crystals were ground, dissolved in MilliQ water (8 g$L^{-1}$, pH 13 with NaOH) and frozen until use.

### 2.4.3. CRYSTALLIZATION EXPERIMENTS

*Sporosarcina pasteurii* DSM-33 (ATCC 11859) was purchased from the Leibniz Institute DSMZ (Germany) and cultured in SP2-medium (20 g$L^{-1}$ yeast extract, 10 g$L^{-1}$ $NH_4Cl$, 10 µM $NiCl_2$, pH 8.5 with NaOH, sterilized by autoclaving) [13]. This medium was used for generation of glycerol stocks (20% w/v) and starter cultures for crystallization experiments. For the latter, *S. pasteurii* was cultured for 2 days at 20 °C. The culture was then concentrated 10× by centrifugation for 15 min at 1500 × *g* and mixed 1:1 with sterile 40% w/v glycerol. Aliquots were stored at −80 °C until use.

Crystallization experiments were performed by placing a glass slide covered with a $CaCO_3$ thin film, facing downwards, on magnetic stirrer bars as supports, in an 800 mL glass beaker. The beaker was then filled with 100 mL crystallization medium (10 g$L^{-1}$ tryptone, 5 g$L^{-1}$ yeast extract, 10 g$L^{-1}$ $NH_4Cl$, 60 mM $CaCl_2$, 20 g$L^{-1}$ urea, sterilized by autoclaving except urea, which was filter-sterilized) and inoculated with 100 µL *S. pasteurii* starter culture. After incubation overnight at 28 °C without shaking, the glass slide was removed, rinsed with MilliQ water, and air-dried. For experiments with PGA, the slide was then covered with PGA solution (0.5 mg PGA/$cm^2$) and dried with a hot air gun (Limitless LS-H2000, 2000 W). Crystallization of $CaCO_3$ and application of PGA (where applicable) were repeated 23 times, the first two PGA applications were omitted to provide a better substrate for $CaCO_3$ deposition on the slides.

### 2.4.4. ELECTRON MICROSCOPY AND LAYERING ESTIMATE

Before imaging by scanning electron microscopy (SEM), samples were fractured manually and covered with a 10 nm gold film using a Leica EM ACE 60 sputter coater. SEM was performed with a FEI Nova Nano SEM 450, using a beam acceleration of 3 kV. To estimate the extent of layering in a sample, entire cross-sections were imaged, and the width of the layered structures measured.

*M. edulis* shells were prepared similarly but fractured with a hammer prior to imaging.

## REFERENCES




[1] D. T. Schmieden, A. S. Meyer, and M.-E. Aubin-Tam, *Using bacteria to make improved, nacre-inspired materials,* MRS Advances **1**, 559 (2016).

[2] M. A. Meyers, P.-Y. Chen, A. Y.-M. Lin, and Y. Seki, *Biological materials: Structure and mechanical properties,* Progress in Materials Science **53**, 1 (2008).

[3] J. Sun and B. Bhushan, *Hierarchical structure and mechanical properties of nacre: a review,* RSC Advances **2**, 7617 (2012).

[4] J. Wang, Q. Cheng, and Z. Tang, *Layered nanocomposites inspired by the structure and mechanical properties of nacre,* Chemical Society Reviews **41**, 1111 (2012).

[5] I. Corni, T. J. Harvey, J. A. Wharton, K. R. Stokes, F. C. Walsh, and R. J. K. Wood, *A review of experimental techniques to produce a nacre-like structure,* Bioinspiration & Biomimetics **7**, 031001 (2012).

[6] S. Deville, E. Saiz, R. K. Nalla, and A. P. Tomsia, *Freezing as a path to build complex composites,* Science **311**, 515 (2006).

[7] P. Das, J.-M. Malho, K. Rahimi, F. H. Schacher, B. Wang, D. E. Demco, and A. Walther, *Nacre-mimetics with synthetic nanoclays up to ultrahigh aspect ratios,* Nature Communications **6** (2015).

[8] F. Hammes and W. Verstraete, *Key roles of ph and calcium metabolism in microbial carbonate precipitation,* Reviews in Environmental Science and Biotechnology **1**, 3 (2002).

[9] M. P. Harkes, L. A. van Paassen, and V. S. Whiffin, *Microbial carbonate precipitation as a soil improvement technique,* Geomicrobiology Journal **24**, 417 (2007).

[10] L. A. van Paassen, R. Ghose, T. van der Linden, W. van der Star, and M. van Loosdrecht, *Quantifying biomediated ground improvement by ureolysis: Large-scale biogrout experiment,* Journal of Geotechnical and Geoenvironmental Engineering **136**, 1721 (2010).

[11] S. S. Bang, J. K. Galinat, and V. Ramakrishnan, *Calcite precipitation induced by polyurethane-immobilized bacillus pasteurii,* Enzyme and Microbial Technology **28**, 404 (2001).

[12] K. L. Bachmeier, A. E. Williams, J. R. Warmington, and S. S. Bang, *Urease activity in microbiologically-induced calcite precipitation,* Journal of Biotechnology **93**, 171 (2002).

[13] S. Makino, I. Uchida, N. Terakado, C. Sasakawa, and M. Yoshikawa, *Molecular characterization and protein analysis of the cap region, which is essential for encapsulation in bacillus anthracis,* Journal of Bacteriology **171**, 722 (1989).

[14] F. B. Oppermann-Sanio and A. Steinbüchel, *Occurrence, functions and biosynthesis of polyamides in microorganisms and biotechnological production,* Naturwissenschaften **89**, 11 (2002).

[15] J. M. Buescher and A. Margaritis, *Microbial biosynthesis of polyglutamic acid biopolymer and applications in the biopharmaceutical, biomedical and food industries,* Critical Reviews in Biotechnology **27**, 1 (2007).

[16] A. Sugawara and T. Kato, *Aragonite caco3 thin-film formation by cooperation of mg and organic polymer matrices,* Chemical Communications , 487 (2000).

[17] H. Jiang, L. Shang, S. Yoon, S. Lee, and Z. Yu, *Optimal production of poly-gamma-glutamic acid by metabolically engineered escherichia coli,* Biotechnology Letters **28**, 1241 (2006).

[18] M. Ashiuchi, K. Soda, and H. Misono, *A poly-gamma-glutamate synthetic system of bacillus subtilis ifo 3336: Gene cloning and biochemical analysis of poly-gamma-glutamate produced by escherichia coli clone cells,* Biochemical and Biophysical Research Communications **263**, 6 (1999).

[19] H. Gao, B. Ji, I. L. Jäger, E. Arzt, and P. Fratzl, *Materials become insensitive to flaws at nanoscale: Lessons from nature,* Proceedings of the National Academy of Sciences **100**, 5597 (2003).

[20] G. Kedia, D. Hill, R. Hill, and I. Radecka, *Production of poly-gamma-glutamic acid by bacillus subtilis and bacillus licheniformis with different growth media,* Journal of Nanoscience and Nanotechnology **10**, 5926 (2010).

[21] B. Manocha and A. Margaritis, *A novel method for the selective recovery and purification of gamma-polyglutamic acid from bacillus licheniformis fermentation broth,* Biotechnology progress **26**, 734 (2010).

# 3

# BACTERIALLY-PRODUCED, NACRE-INSPIRED COMPOSITE MATERIALS

**Dominik T. SCHMIEDEN*, Ewa M. SPIESZ*, Antonio M. GRANDE, Kuang LIANG, Jakob SCHWIEDRZIK, Filipe NATALIO, Johann MICHLER, Santiago J. GARCIA, Marie-Eve AUBIN-TAM, Anne S. MEYER**

Living organisms can produce highly tough and strong composite materials such as nacre or bone under ambient conditions [1, 2]. The impressive mechanical properties of natural composites arise from their multi-scale hierarchical structures, which span from nano- to macroscale [3]. The high toughness of natural composite materials derives from their diverse mechanisms for effective energy dissipation, including crack deflection, organic components acting as viscoelastic matrix, and nano-asperities that resist inelastic shearing [3, 4]. Tough bio-inspired materials have broad potential applications as advanced materials, but the current production methods are complex and typically involve toxic chemicals, extreme temperatures, and/or high pressures [5–7]. Here, we introduce the use of bacteria to produce high-performance composite materials. Remarkably, both the organic and the inorganic phase of our composite material were generated by bacteria. The resulting calcium carbonate-polyglutamate composite ("bacterial nacre") displayed a hierarchical structure similar to natural nacre and showed toughness four times higher than other calcium carbonate materials examined in this study, either bacterially or chemically-produced. On the nanoscale, the bacterial nacre

* equally contributing authors

showed a granular structure containing nano-asperities, which have been reported to be responsible for local toughening mechanisms in natural nacre [4]. The bacterial nacre showed improved extensibility while maintaining high stiffness, which is uncharacteristic of calcium carbonate materials [3]. Our results demonstrate a new bacteria-driven production method of nacre-inspired tough and stiff materials. The extensive diversity of bacterial metabolic abilities and the possibility of genetic engineering will allow for the creation of bacterially-inspired nacre, with the potential of creating a library of eco-friendly composite materials with tunable mechanical properties.

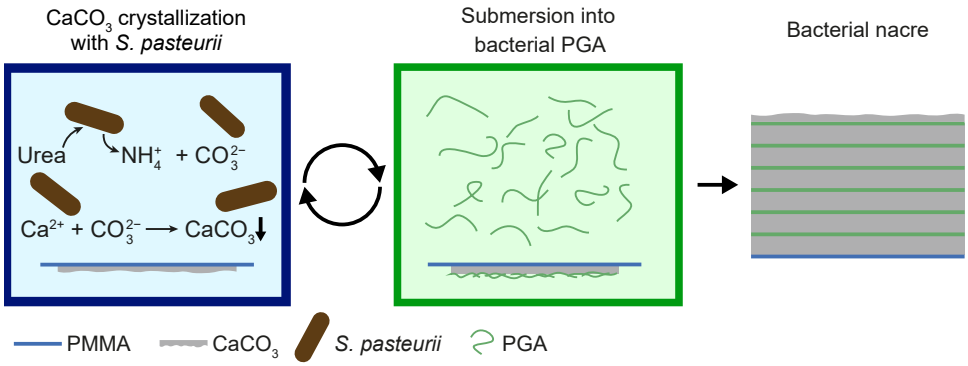


Figure 3.1: Production of bacterial nacre. A PMMA slide was submerged in a growth medium containing *Sporosarcina pasteurii* to form calcium carbonate in the presence of urea and calcium ions. The slide was then immersed in bacterially-produced PGA solution, which resulted in PGA binding to the calcium carbonate. Both steps (with intermediate washing, described in detail in Section 3.4) were repeated 23 times to form the approx. 200 µm-thick bacterial nacre composite deposited on the slide. For bacterial $CaCO_3$ samples, the PGA application step was omitted.

## 3.1. INTRODUCTION

The use of bacteria as cell factories is a well-established and cost-effective biotechnological process for industrial-scale production of compounds such as polymers (e.g., PLGA [8] or PHA [9]) and inorganic materials (e.g. calcium carbonate [10]). Such bacterially-produced materials are typically far simpler than the complex hierarchical materials made by other living organisms in nature. Biological materials such as tooth enamel, nacre, or bone attain their superior mechanical properties from a combination of organic and inorganic components as well as from the specific structural arrangements across different length scales [2, 3]. For instance, nacre, the tough, iridescent layer constituting the inner lining of mollusk shells, consists of a tessellated structure [2] of layered calcium carbonate platelets interconnected by an organic matrix to create a hierarchical structure [3, 11].

As shown in Chapter 2, we used bacteria to assemble a bio-inspired, nacre-like composite material. We alternately deposited calcium carbonate and γ-polyglutamate (PGA) layers produced by two different bacterial strains. Calcium carbonate was generated by microbially-induced calcium carbonate precipitation with the bacterium *Sporosarcina pasteurii* [10] in a crystallization medium containing urea. *S. pasteurii* expresses urease, an enzyme that cleaves urea into ammonia and carbonate [10]. The resultant increase in pH shifts the equilibrium of carbonate, causing precipitation of calcium carbonate [12]. *Bacillus licheniformis* [13] was used to produce the anionic polymer PGA to act as an organic matrix between the calcium carbonate layers, as well as providing equally-distributed negative charges as nucleation centers for $CaCO_3$ crystallization [14].

Here, the process described in Chapter 2 was modified by replacing the chitosan-modified glass microscope slide used as crystallization substrate. Chitosan films swell in water, so that samples underwent deformation during the wet-dry cycles during production, leading to substantial loss of samples and detachment from the substrate. Fur-

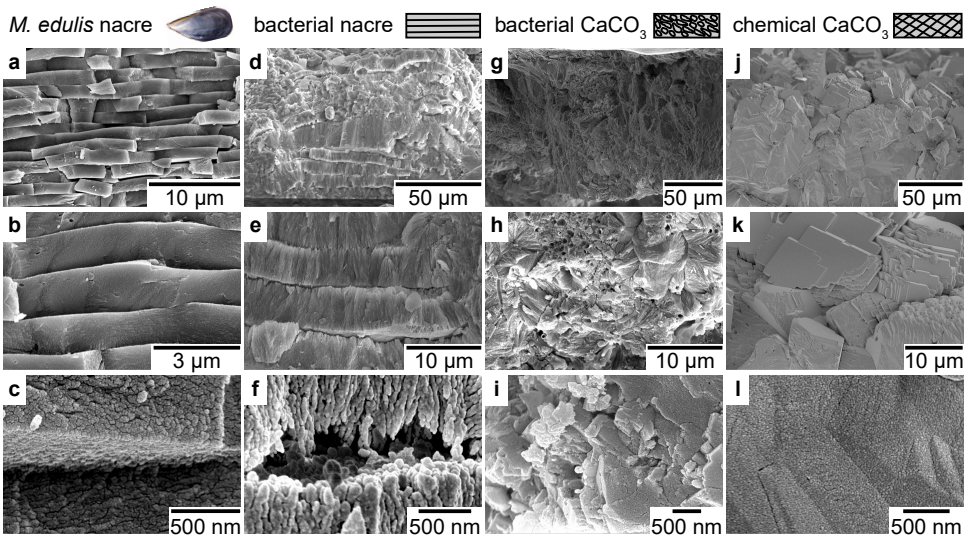


Figure 3.2: Bacterially-produced nacre contained calcium carbonate layers similar to natural nacre. Samples were fractured, and cross-sections were imaged by SEM. (a) *Mytilus edulis* nacre showed a characteristic layered structure with (b) layer irregularity enabling interlocking and (c) nano-asperities that resist inelastic shearing, both acting as toughening mechanisms. (d) Bacterial nacre, produced through alternate deposition of calcium carbonate by *S. pasteurii* and submersion in PGA produced with *B. licheniformis*, also displayed (e) irregular layers and (f) nano-asperities, which might contribute to increased toughness. (g–i) Bacterial calcium carbonate material produced by repeated deposition with *S. pasteurii* without PGA showed few layered structures. (j) Chemically-produced calcium carbonate material generated by slow diffusion of ammonia and $CO_2$ into a $CaCl_2$ solution showed (k) no layers and (l) no nano-asperities.

thermore, the rigid, approximately 1 mm thick microscope slide prevented the use of 3-point bending experiments, since the behavior of the glass substrate would have occluded the effect of the much thinner nacre-mimetic coating. In the modified procedure upon which the results of this chapter are based, the deposition process (Figure 3.1) began with the formation of a layer of calcium carbonate on poly(methyl methacrylate) (PMMA) slides by horizontal suspension of the slides within a culture of *S. pasteurii*. This step was followed by placing the calcium carbonate-covered PMMA slides into a solution of PGA collected from *B. licheniformis* cultures. The process was iteratively repeated to produce nacre-resembling layered composites, here called "bacterial nacre", with a thickness of approximately 200 µm. A bacterially-produced $CaCO_3$ material without PGA ("bacterial $CaCO_3$") and a purely inorganic calcium carbonate material precipitated via a chemical slow diffusion method [15] ("chemical $CaCO_3$") were also deposited on PMMA slides and used as controls.

## 3.2. RESULTS AND DISCUSSION

Scanning electron microscopy (SEM) analysis of freshly fractured sections of bacterial nacre revealed structural similarity to *Mytilus edulis* nacre, a natural nacre chosen as an additional control. *M. edulis* and bacterial nacre showed layered structures with a

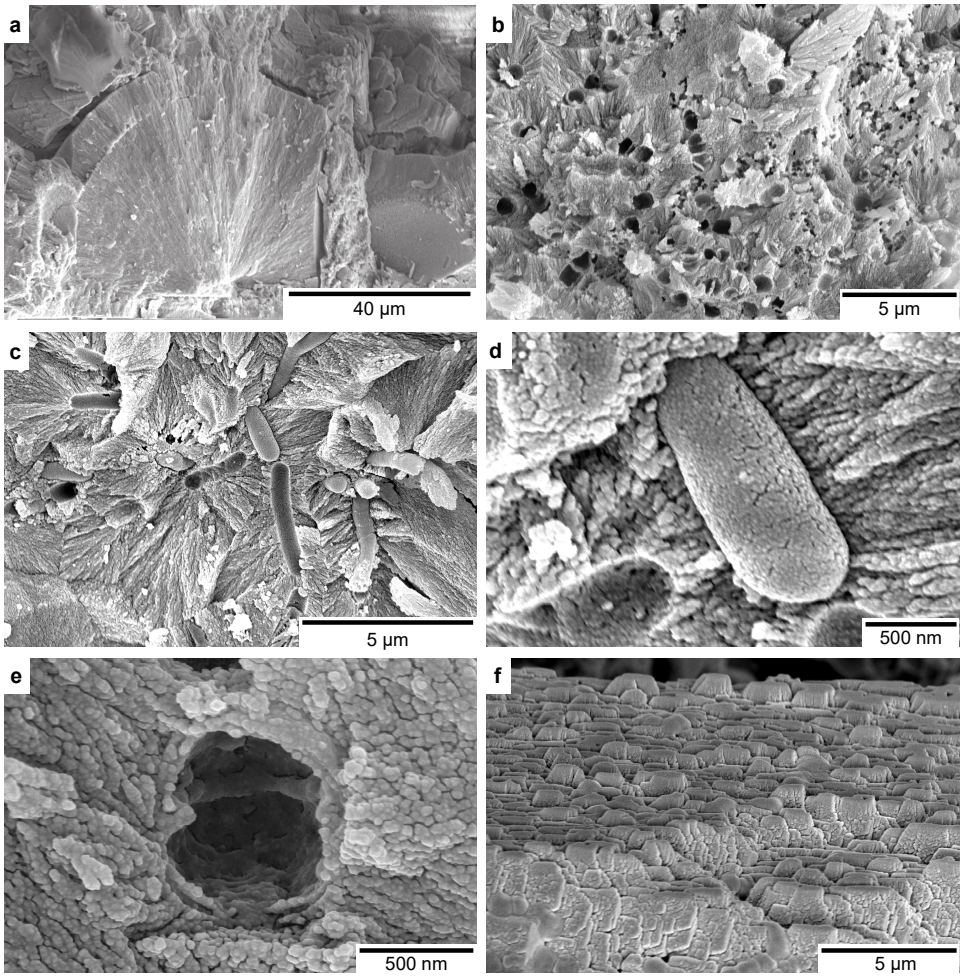


Figure 3.3: Structural details of bacterially-produced materials visualized by SEM (a–e) *S. pasteurii* was used repeatedly to crystallize calcium carbonate on PMMA slides. (a) Spherulites, round crystallites with a spherical shape, were occasionally found in bacterially-produced $CaCO_3$ samples. (b-e) *S. pasteurii* and bacteria-sized cavities found in bacterially-produced $CaCO_3$ samples. (f) Calcium carbonate deposited by *S. pasteurii* onto 3D-printed PLA substrate.

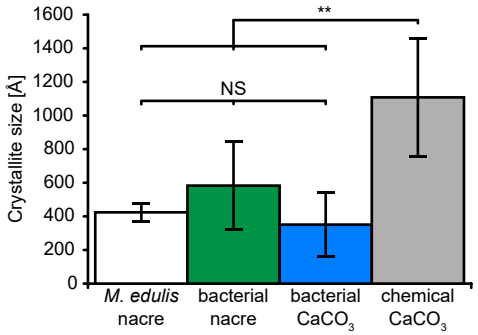


Figure 3.4: Naturally-mineralized and bacterially-produced materials showed smaller crystallite sizes than chemically-produced $CaCO_3$ materials. XRD was performed on powdered samples. Scherrer's equation was applied to determine crystallite sizes, taking the peak full-width half-maximum (FWHM), removing the instrumental broadening, and then assuming that all remaining broadening was caused by particle size effects alone. Data represent medians with the interquartile range ($n = 3$). Significant differences marked as ** for $p < 0.01$, and NS for not significant.

layer thickness of 1.4 ± 0.3 µm (Figure 3.2a, b) and 16.2 ± 15.0 µm (Figure 3.2d, e), respectively. The layered calcium carbonate platelets in bacterial nacre were formed by dense needle-like structures (Figure 3.2f) and were oriented parallel to each other, as in natural nacre (Figure 3.2b, e). This morphology suggests that PGA can promote layered crystal growth, as reported elsewhere [16]. In contrast, the bacterial $CaCO_3$ specimens displayed a prevalence of randomly distributed plates, with less than 10% of the cross-sectional area containing layered zones (Figure 3.2g, h). The layers in bacterial $CaCO_3$ samples were limited to spherical crystal structures (spherulites [17], Figure 3.3a) that occasionally appeared in the bacterial nacre samples as well (Figure 3.2d). In contrast, the chemically-produced calcium carbonate material showed no clear formation of small particles but rather large crystals with no layered structure (Figure 3.2j–l).

On the nanoscale, the two bacterially-produced materials showed a granular texture similar to *M. edulis* nacre (which contained nano-asperities of approx. 20–40 nm in diameter, Figure 3.2c, comparable to other natural nacres [4]). Nano-asperities in the bacterial nacre showed a similar diameter of approx. 10–70 nm (Figure 3.2f), while in the bacterial $CaCO_3$ they were somewhat larger (approx. 60–90 nm, Figure 3.2i). Chemically-produced calcium carbonate showed neither granular texture nor nano-asperities (Figure 3.2l), and the average crystallite size was significantly larger (Figure 3.4). The nano-granular morphology found only in the biomineralized samples (nacre and bacterially-produced materials) may be the result of the various (organic) components present during crystallization, such as PGA or urea in the bacterial growth medium, which might influence crystal formation and the polymorph (crystal structure) [15, 18].

Crystal polymorph analyses of the bacterially-produced materials, determined by X-ray diffraction (XRD), showed a mixture of calcite and vaterite (approximately 40 wt % and 60 wt % respectively, Figure 3.5a, confirmed by TEM, Figures 3.6, 3.7), similar to other microbially-induced calcium carbonate materials [19, 20], while *M. edulis* nacre contained exclusively aragonite (100.0 ± 0.0 wt %), and chemically-produced samples

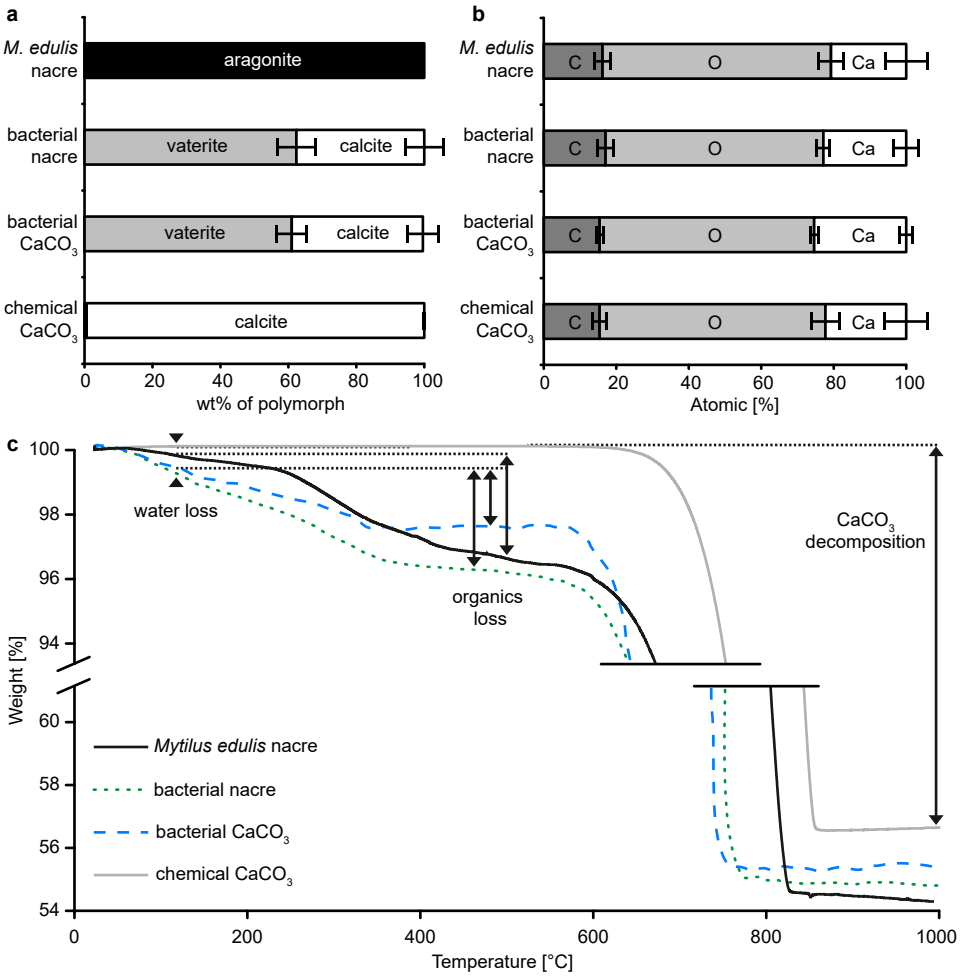


Figure 3.5: Chemical analysis of bacterially-generated materials. (a) XRD analysis showed weight fractions of calcium carbonate polymorphs (aragonite, calcite, vaterite) present in the samples ($n \geq 3$). *M. edulis* nacre consisted exclusively of aragonite (100.0 ± 0.0 wt %), while bacterial nacre contained 62.4 ± 5.9 wt % vaterite and 37.6 ± 5.9 wt % calcite, and bacterial $CaCO_3$ contained 61.0 ± 4.8 wt % vaterite and 38.6 ± 5.9 wt % calcite. Differences between the bacterially-produced materials were not significant ($p > 0.05$), but they were significantly different from natural nacre ($p < 0.01$) and chemical $CaCO_3$ ($p < 0.01$). Chemically-produced samples consisted of 99.4 ± 0.1 wt % calcite with 0.6 ± 0.1 wt % aragonite. (b) Elemental compositions were determined using EDX. Carbon (C), oxygen (O), and calcium (Ca) were detected. The data represent means with standard deviations ($n \geq 5$). Differences between the groups were statistically insignificant ($p > 0.05$). (c) Thermogravimetric traces ($n \geq 3$) indicated weight fractions of organic material. Chemically-precipitated calcium carbonate samples showed no organic content (0.0 ± 0.0 wt %), while both bacterially-created samples, as well as nacre samples, contained a fraction of organics (4.4 ± 0.5, 3.4 ± 0.0, 3.7 ± 0.6 wt %, for bacterial nacre, bacterial $CaCO_3$, and *M. edulis* nacre, respectively).

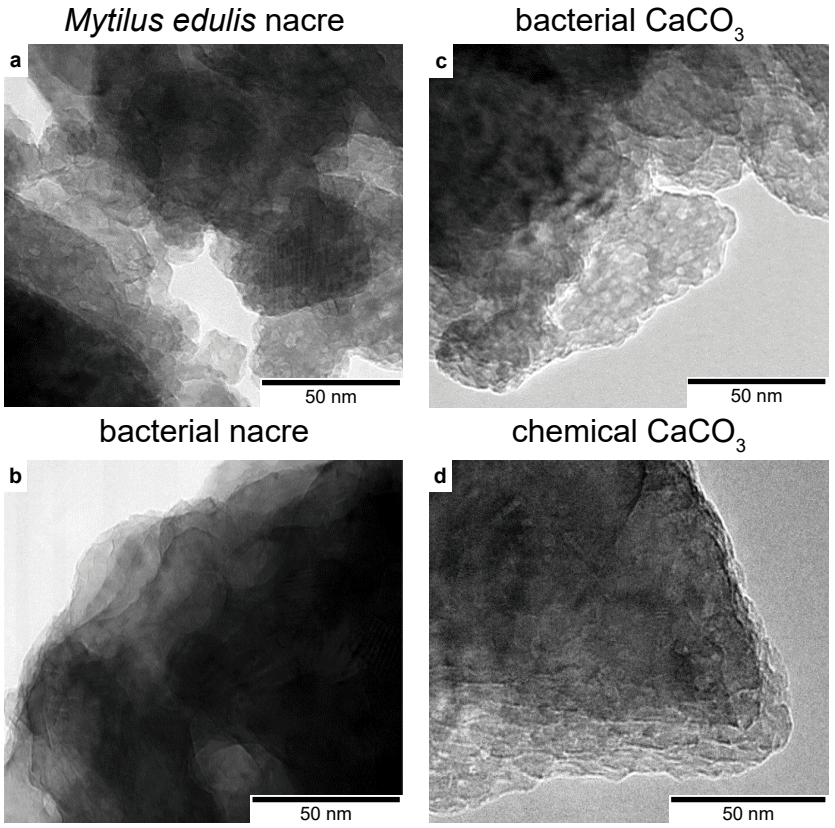


Figure 3.6: TEM images of (a) *Mytilus edulis* nacre, (b) bacterial nacre, (c) bacterial $CaCO_3$ and (d) chemical $CaCO_3$.

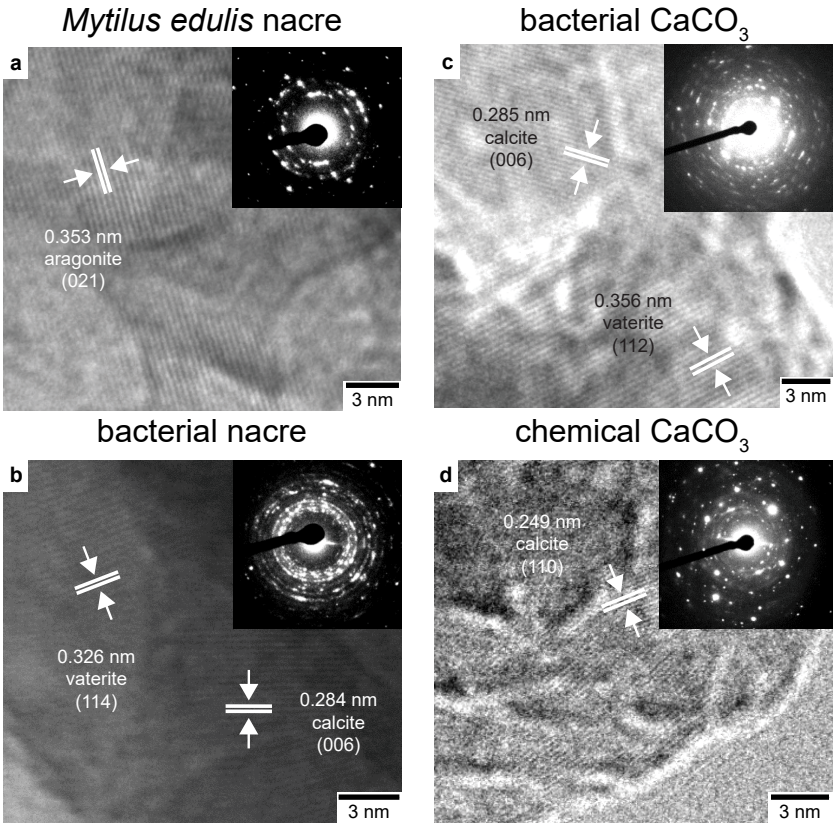


Figure 3.7: Identification of crystal polymorphs through TEM analysis. HRTEM images of (a) *Mytilus edulis* nacre, (b) bacterial nacre, (c) bacterial $CaCO_3$ and (d) chemical $CaCO_3$. The arrows point out typical lattice distances. The text labels state the measured distance, the corresponding crystal polymorph, and the crystal orientation. The inserts show the corresponding SAED patterns.

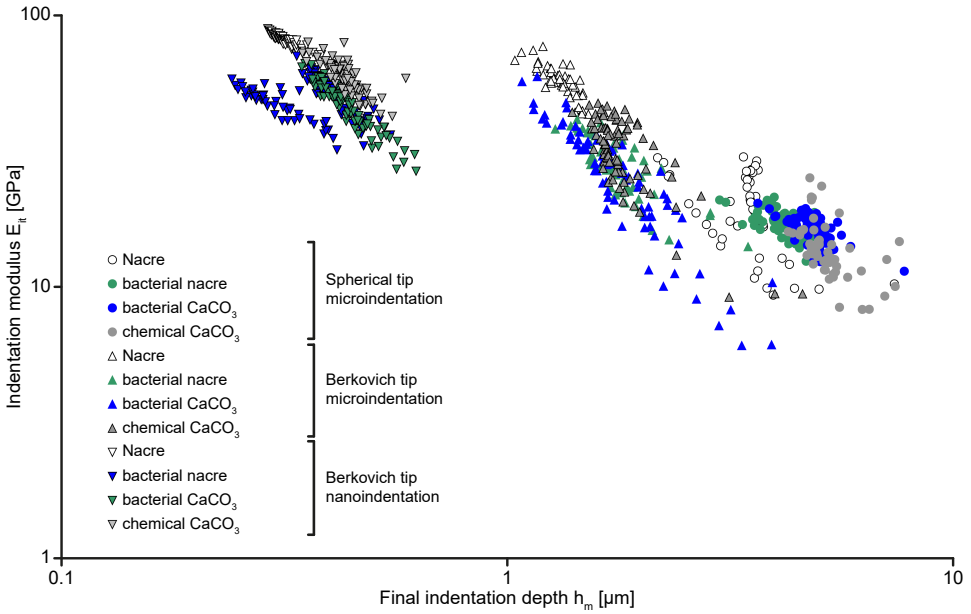


Figure 3.8: The indentation moduli of all examined materials decreased with increasing indentation depth. The indentation moduli of *M. edulis* nacre, bacterial nacre, bacterially produced $CaCO_3$, and chemically-produced $CaCO_3$ were determined with micro- and nanoindentation to varying final indentation depths. Triangular symbols indicate a Berkovich indenter, and spherical symbols indicate a spherical indenter, $n \geq 3$ (at least 60 indents per sample type).

consisted almost exclusively of calcite (99.4 ± 0.1 wt %) [15]. The ratio of vaterite to calcite in bacterially-produced samples could have changed over the course of the production cycle, since the samples periodically entered conditions of under-saturation (after submersion in fresh bacteria suspension), which is known to facilitate vaterite-to-calcite conversion [21].

Samples were analyzed with thermogravimetry (Figure 3.5c) to estimate the content of organics. Bacterial nacre contained 4.43 ± 0.48 wt % organics. This value was significantly higher than in bacterial $CaCO_3$ samples, which contained 3.39 ± 0.02 wt % ($p < 0.05$), indicating an estimated PGA content of 1 wt % in bacterial nacre. The organic content of bacterially-produced samples did not differ significantly from natural nacre (organic content of 3.92 ± 0.63 wt %, consistent with reported values [3], $p = 0.21$ and 0.68, respectively). The organics present in the bacterial $CaCO_3$ samples likely originated from the presence of bacteria and/or growth medium components in this material; no organics were found in the chemically-produced $CaCO_3$.

The mechanical properties of the bacterially-produced materials were determined at different length scales [22]: nanoscopically with nanoindentation, microscopically with microindentation, and macroscopically with three-point bending tests. Using mechanical tests at these three hierarchical levels allowed a determination of how the properties changed throughout the length scales (Figure 3.8). Nanoindentation showed a high stiff-

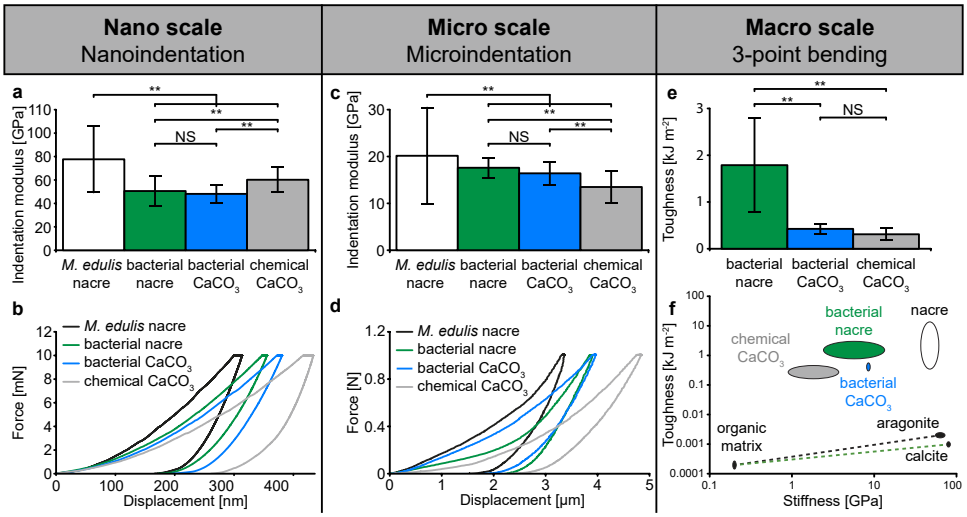


Figure 3.9: Bacterial nacre showed increased toughness and extensibility compared to bacterial $CaCO_3$ and chemical $CaCO_3$. (a) Nanoindentation stiffness (indentation moduli) measured with indentation depths up to approximately 350 nm using a pyramidal Berkovich tip ($n \geq 3$, at least 60 indents per sample type). (b) Representative nanoindentation curves. (c) Microindentation stiffness (indentation moduli) measured with a spherical tip, with an approximate maximum indentation depth of 1.5 µm ($n \geq 3$, at least 60 indents per sample type). (d) Representative microindentation curves. (e) Toughness measured in 3-point bending experiments. (f) The rule of mixtures (dashed lines) is a simplified model for estimating mechanical properties of composite materials based on the properties of components and their volume fractions [3]. Both natural nacre and the samples produced in this work violate this rule, indicating that more complex toughening mechanisms are involved. Data are presented as medians with interquartile range. Significant differences marked as * for $p < 0.05$, ** for $p < 0.01$, and NS for not significant.

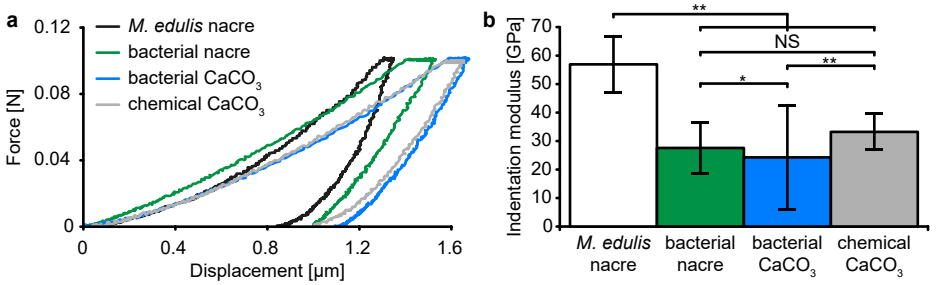


Figure 3.10: Indentation curves and indentation moduli obtained from microindentation using a Berkovich tip. (a) Typical force-displacement curves and (b) resulting indentation moduli. Indentation protocols involved a maximum indentation depth of approximately 1.5 µm, $n \geq 3$ (at least 60 indents per sample type). Significant differences marked as * for $p < 0.05$, ** for $p < 0.01$, and NS for not significant.

ness (indentation modulus) in all samples: 77.7 ± 29.1 GPa in *M. edulis*, 49.3 ± 8.2 GPa in bacterial nacre, 47.5 ± 6.1 GPa in bacterial $CaCO_3$, and 59.3 ± 8.1 GPa in chemical $CaCO_3$ ($n \geq 3$, at least 60 indents per sample type). No significant difference in stiffness between the two bacterial material types was measured ($p = 0.83$), while the differences with respect to *M. edulis* nacre and the chemically precipitated $CaCO_3$ were significant ($p < 0.01$, Figure 3.9a). The nanoindentation stiffness of the bacterial nacre was higher than for other artificial nacre materials reported [7, 23]. Similar trends were observed in microindentation, but the average indentation moduli were lower. This finding is probably related to the greater indentation depths—when sampling a bigger volume of the material, we expect the soft organic components to influence the measurement more than with lower indentation depths, where mostly the $CaCO_3$-surface is sampled (20.2 ± 10.5 GPa in *M. edulis*, 17.6 ± 2.3 GPa in bacterial nacre, 16.4 ± 2.7 GPa in bacterial $CaCO_3$, and 13.5 ± 3.6 GPa in chemical $CaCO_3$, $n \geq 3$, at least 60 indents per sample type; Figure 3.9c, d and Figure 3.10).

At the macroscale, characteristic parameters such as toughness, flexural stiffness, and extensibility (strain at failure), were determined in un-notched three-point bending experiments [24] (Figures 3.9e–f, 3.11, 3.12). Remarkably, we could not identify any macroscopic cracks in the bacterial nacre at high strains, at strain regimes prior to where the crystallization substrate (PMMA) dominates the mechanical response (Figure 3.11). This behavior contrasted with that of the other two sample types not containing PGA (bacterial and chemical $CaCO_3$, Figure 3.11), where large cracks were detected. The toughness (work of fracture) of bacterial nacre was 1.7 ± 1.0 kJ m$^{-2}$ ($n = 6$), within the lower range of toughness reported for natural nacre (0.3–13 kJ m$^{-2}$ [3, 25]). Since we could not detect macrocracks in these samples, we used video data and comparisons to the 3-point bending curves of pure PMMA substrates to gauge the point of failure. This procedure might have led to an underestimation of the toughness. Nevertheless, the toughness of the bacterial nacre constituted an approximately fourfold increase over the bacterial $CaCO_3$ (0.4 ± 0.1 kJ m$^{-2}$, $n = 4$) and an almost six-fold increase compared to the chemically-produced samples (0.3 ± 0.1 kJ m$^{-2}$, $n = 3$, Figure 3.9e). We have not found significant differences in macroscopic flexural stiffness of the bacterially-produced materials (7.9 ± 5.5 GPa and 7.5 ± 3.7 GPa for bacterial nacre, $n = 6$, and bacterial $CaCO_3$,

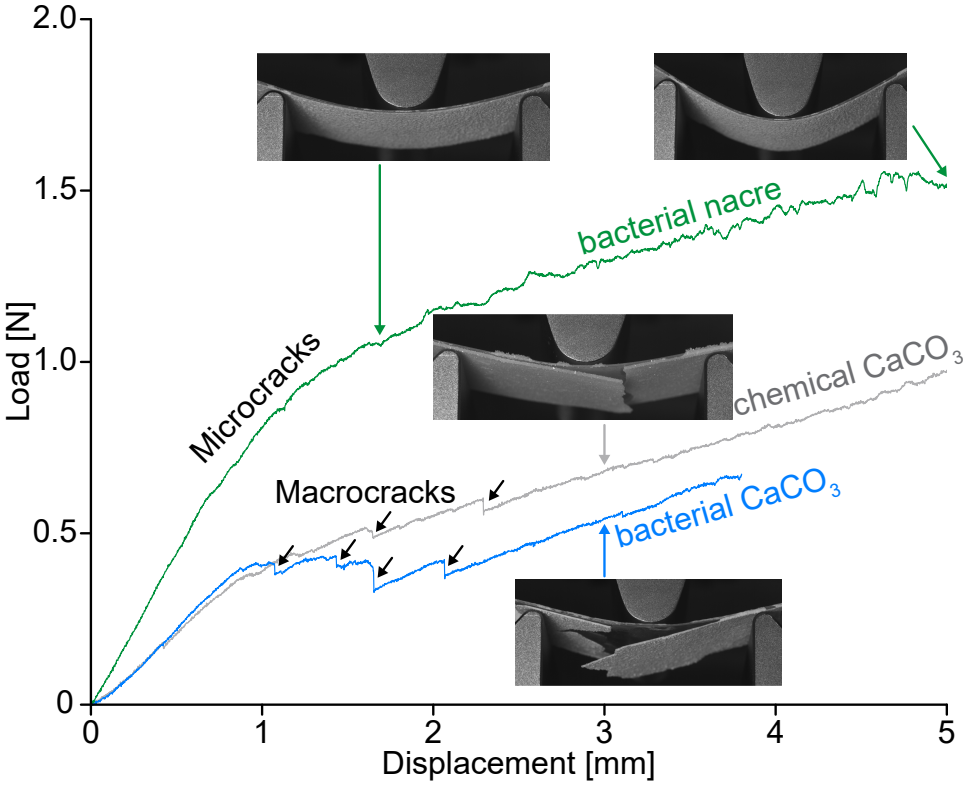


Figure 3.11: Bacterial nacre shows a distinct cracking behavior from both chemically and bacterially-produced $CaCO_3$. The figure depicts representative force-displacement curves acquired during 3-point bending experiments, as well as images of the samples. The first image of bacterial nacre shows the point where the mechanical response has transitioned to being governed by the PMMA substrate. The response until this point is likely reflective of microcracking behavior. The second image of bacterial nacre shows that even at a much higher displacement, no major cracks were observed. In contrast, distinct macrocracks could be observed in the responses of bacterially- and chemically-produced $CaCO_3$ (indicated by black arrows). Images of high extensions for chemical and bacterial $CaCO_3$ are included to demonstrate the complete breakage of the coating material and its detachment from the substrate. The curves of all samples are depicted in Figure 3.12.

$n$ = 4, respectively) and the chemically-produced samples (2.3 ± 1.4 GPa, $n$ = 3, Figure 3.12d), while the flexural strength was significantly higher in bacterial nacre (Figure 3.12e). The extensibility of the bacterial nacre (0.31 ± 0.05 %) was almost twice that of bacterial $CaCO_3$ and chemical $CaCO_3$ (0.16 ± 0.04 % and 0.18 ± 0.09 %, respectively, $p < 0.05$). The distinct cracking behaviors of the samples with and without PGA lead us to hypothesize that bacterial nacre might employ several toughening mechanisms, including crack deflection upon entering the layer interfaces, increased crack path length and energy absorption [26, 27], or nano-asperities [3]. Moreover, the organics might act as a viscoelastic adhesive, and the irregularity of the layers may enable layer interlocking [2, 3].



## 3.3. CONCLUSION

The bacterial nacre developed here demonstrates improved toughness and extensibility, without sacrificing stiffness, a combination of properties that is difficult to achieve in man-made materials [28]. These properties arise from a distinct failure mode, where microcracks instead of macrocracks occur. The exact mechanisms underlying these differences remain to be investigated, possible candidates are strain hardening through nano-asperities and the organic phase, as well as crack deflection at layer interfaces. The key advantage of our method of bio-inspired materials production is that it is performed exclusively with bacteria: under ambient conditions, using only ecologically-friendly and renewable components, and without producing toxic waste. Bacteria are readily available for genetic engineering, show an enormous diversity of metabolic activities, and are already used extensively in biotechnology and synthetic biology for the production of chemicals and materials [29]. Moreover, complex (3D printed) structures, made from e.g. PLA, can be easily covered with the composite material (Figure 3.3f). Our method demonstrates a first step towards the bacterial production of completely new composite materials that can be tailored towards a wide range of applications, e.g. as tough, lightweight biomimetic coatings for civil engineering or the automotive and aerospace industries.

## 3.4. METHODS

### 3.4.1. SUBSTRATE PREPARATION

All chemical reagents were obtained from VWR Netherlands or Sigma Aldrich Netherlands. PMMA sheets (Goodfellow ME303001, 0.38 mm thickness) were cut into 75 × 25 mm slides and stored in de-ionized water for 2 days for hydration. The slides were then sonicated at 37 kHz (Emmi-D30 sonicator, EMAG) in 50% 2-propanol solution for 15 min [30]. The surface hydrophilicity was increased by incubation at 40 °C in 10 M NaOH for 3 days. The slides were rinsed with de-ionized water and submerged in a solution of 30 mM $CaCl_2$, 90 mM $MgCl_2$, and 0.005% (w/v) polyacrylic acid. The submerged samples were placed into a desiccator alongside a 25 mL beaker containing a 1 cm-thick layer of freshly crushed $(NH_4)HCO_3$ powder and incubated for 3 days in order to produce a thin $CaCO_3$ film on the slides. Such prepared slides were stored in de-ionized water until used.

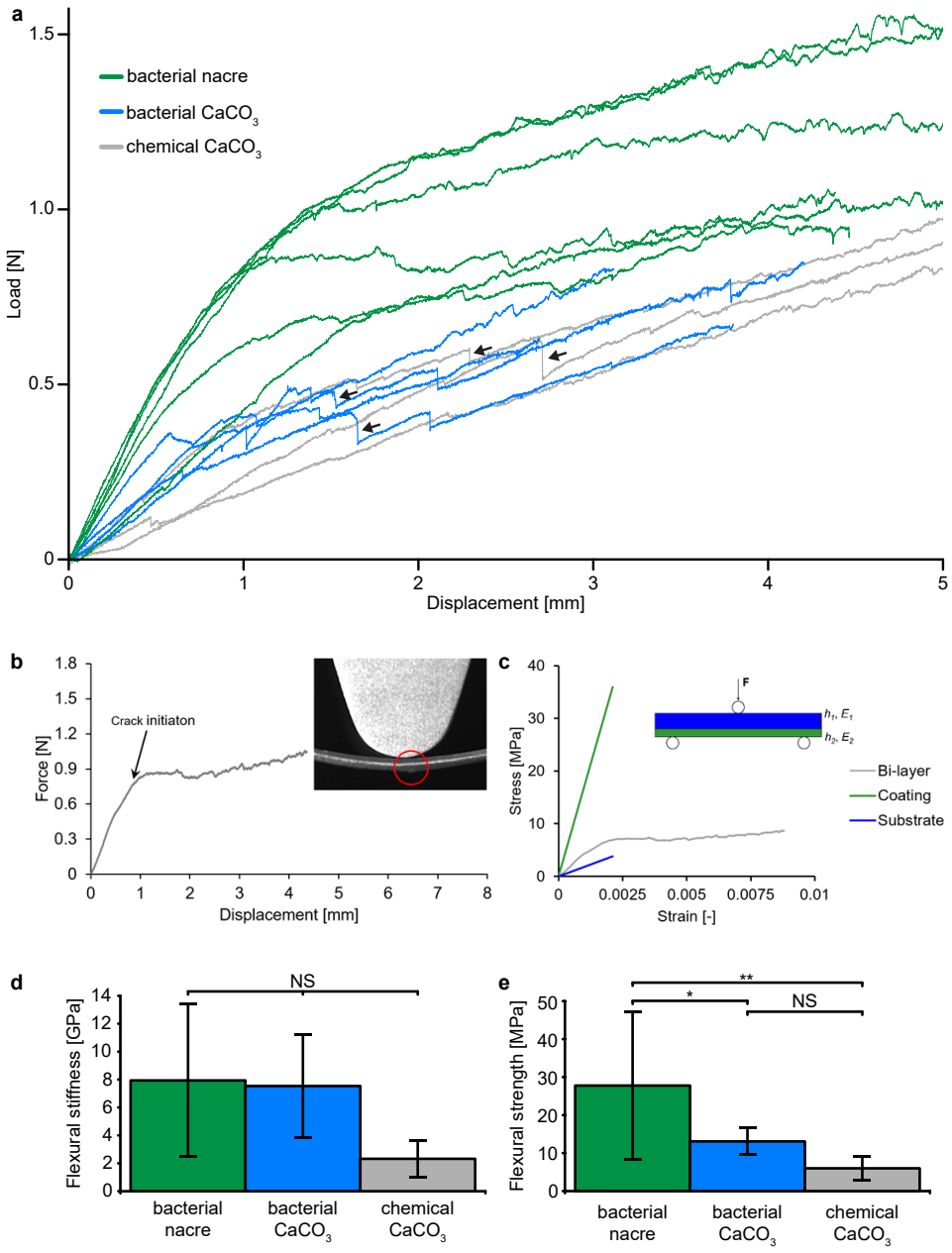


Figure 3.12: Bacterial nacre displayed a distinct cracking mechanism that resulted in improved flexural strength and toughness. (a) Force-displacement curves acquired during 3-point bending tests. Major cracking events are visible in the curves of bacterially and chemically-produced $CaCO_3$ (arrows), but absent in bacterial nacre. (b) The procedure of initial crack detection in cases where no distinct macroscopic crack could be detected in the video recordings: a moving average of the slope of the force-displacement curves was calculated to determine the point at which the stiffness of the coated PMMA slide equaled the slope of an empty PMMA slide tested in 3-point bending. Inset shows a crack detected from the video acquired during a three-point bending tests. (c) The analytical procedure for computing stresses in the elastic deformation region in the tested materials (a bi-layer (grey) composed of the substrate PMMA slide (blue), and the tested material (green): bacterially- or chemically-produced coating material). The details of this procedure are described in Section 3.4.11. Significant differences marked as * for $p < 0.05$, ** for $p < 0.01$, and NS for not significant.

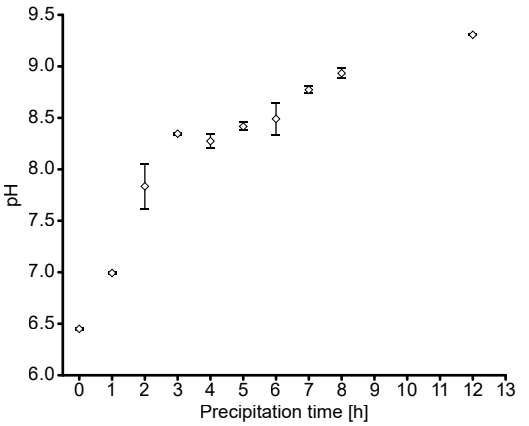


Figure 3.13: pH change of culture medium containing *Sporosarcina pasteurii*. *S. pasteurii* was grown in urea-containing crystallization medium for 12 h at 28 °C with monitoring of the pH changes over time. The data represent means with standard deviations ($n = 4$).

### 3.4.2. MICROORGANISM-INDUCED CALCIUM CARBONATE PRECIPITATION

Single colonies of *Sporosarcina pasteurii* DSM-33 (ATCC 11859, DSMZ, Germany) were inoculated into SP2 medium (10 g L$^{-1}$ $NH_4Cl$, 20 g L$^{-1}$ yeast extract, 10 µM $NiCl_2$, pH 8.5 with NaOH) and grown for 2 days at 28 °C with shaking at 180 rpm. The culture was pelleted by centrifugation (15 min at 1500 × *g*), re-suspended 1:1 in sterile 40% w/v glycerol and stored at −80 °C until used. To perform crystallization, PMMA slides with a $CaCO_3$ thin-film were clamped using a plastic clamp to glass microscope slides (Corning 2947, 75 × 25 mm) and placed into 800 mL glass beakers such that the initial thin film side was facing downwards, at about 5 mm distance above the bottom of the beaker. 100 mL of crystallization medium (10 g L$^{-1}$ tryptone, 5 g L$^{-1}$ yeast extract, 10 g L$^{-1}$ $NH_4Cl$, 60 mM $CaCl_2$, 20 g L$^{-1}$ urea; urea solution sterilized by filtering, the other components autoclaved) containing 1 mL L$^{-1}$ *S. pasteurii* glycerol stock was added to the beaker, and samples were incubated at 28 °C for 12 h without shaking, resulting in a shift of pH (Figure 3.13), which led to the crystallization of calcium carbonate. To produce the bacterial $CaCO_3$ samples, slides were then removed from the beakers, rinsed in de-ionized water, and placed in crystallization medium containing *S. pasteurii* to undergo the next round of crystallization. This procedure was repeated until 23 crystallization events had occurred.

### 3.4.3. PGA PRODUCTION

*B. licheniformis* (NBRC12107, NBRC, Japan) was grown in Medium E [31] for 48 h at 30 °C with shaking at 180 rpm. PGA was isolated from the growth medium by adding $CuSO_4$ to a concentration of 0.4 M and incubation at 4 °C for 12 h. The precipitated PGA (Figure 3.14) was isolated by centrifugation at 8200 × *g* for 10 min at 4 °C and re-dissolved in 1 L of 0.5 M EDTA solution. Cu-EDTA complexes were removed by dialysis against water at 4 °C for 10 days, after which the PGA was lyophilized (Christ Alpha 1-2 LD Plus freeze-drier) and stored dry at room temperature until use.

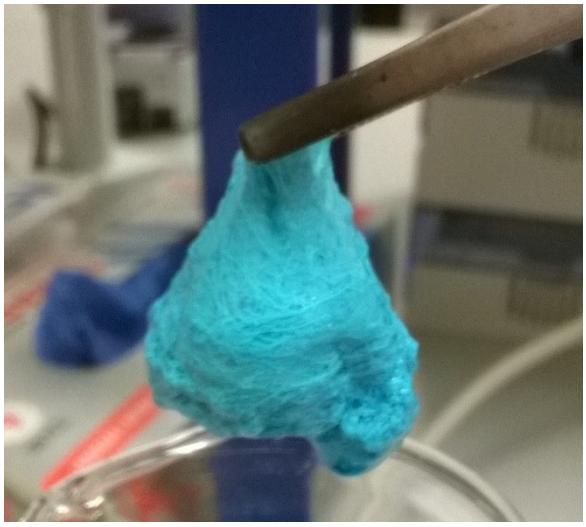

Figure 3.14: Macroscopic amounts of poly-γ-glutamate (PGA) produced with *Bacillus licheniformis*. *B. licheniformis* was grown in Medium E for 48 h at 30 °C with shaking at 180 rpm. The bacteria were removed by centrifugation, and the PGA was precipitated by addition of 0.4 M $CuSO_4$ (the blue color is caused by copper ions).



### 3.4.4. BACTERIAL NACRE

In order to cover the entire surface of a treated PMMA slide with calcium carbonate precipitate, three MICP crystallizations without PGA were performed as described above. PMMA slides were rinsed in de-ionized water after each crystallization event and then suspended horizontally in an 8 $gL^{-1}$ PGA solution (pH 13 with NaOH) at room temperature for 2 h. After rinsing in de-ionized water, the next crystallization event with *S. pasteurii* was performed. Samples underwent 20 crystallization events, alternating with 20 PGA application events. Slides were kept hydrated until the production procedure was completed. After the final crystallization event, slides were rinsed in de-ionized water, air-dried, and unclamped from the glass slides.

### 3.4.5. CHEMICAL CALCIUM CARBONATE CRYSTALLIZATION

Crystallization of calcium carbonate was performed in a desiccator with a diameter of 230 mm at room temperature. Treated PMMA slides were placed into a Petri dish containing 50 mL of 50 mM $CaCl_2$. This Petri dish was placed into the desiccator alongside a 25 mL beaker containing a 1 cm-thick layer of freshly crushed $(NH_4)HCO_3$ powder [15] and incubated at room temperature for 68 days. As $(NH_4)HCO_3$ degraded to $CO_2$ and ammonia, these gases diffused into the calcium chloride solution and caused calcium carbonate crystallize on the slide. The $CaCl_2$ solution was replaced with fresh $CaCl_2$ solution every 3 days.

### 3.4.6. SEM & EDX

Freshly crushed (with a hammer) cross-sections of samples were sputtered with an 8 nm-layer of gold-palladium using an ACE200 sputter coater (Leica) and imaged with a NovaNano SEM (FEI) using 5–15 kV voltage and 5 mm working distance. Measurements of sample and layer thicknesses ($n \geq 3$, at least ten SEM images per group, at least ten consecutive layers measured per image) and the diameters of nano-asperities ($n \geq 3$, at least three SEM images per group, at least five nano-asperities measured per image) in the SEM images were performed using ImageJ software (1.50i, National Institute of Health USA). Elemental analyses were performed using an energy dispersive X-ray spectrometer EDX (FEI) on non-sputtered samples at a voltage of 15 kV (Figure 3.5b). At least three specimens per group ($n \geq 3$) were tested for the elemental composition values presented.



### 3.4.7. XRD

X-ray diffraction samples were ground to a powder in a mortar and deposited manually as a thin layer onto a Si510 wafer in an L510 PMMA sample holder. Non-powdered flakes were also selected to be site-matched to the powdered samples. XRD was performed on both powdered and non-powdered samples using the Bruker D8 Advance diffractometer Bragg-Brentano geometry with a Lynxeye position-sensitive detector, Cu K$\alpha$ radiation, and sample spinning. Parameters used include divergence slit V12, scatter screen height 5 mm, 45 kV, 40 mA, and detector settings: LL 0.11, W 0.14. Measurements were performed via a coupled $\theta$-$2\theta$ scan 10–110 ° with step size 0.020° $2\theta$ and a counting time per step of 2 s. The diffractograms were analyzed using the Bruker software DiffracSuite.EVA v4.2. Crystalline structures were assigned through comparison of experimentally determined peak positions and intensities with the ICDD pdf4 database. Thereafter, results were refined using the Profex/BGMN Rietveld refinement software [32], for which complete XRD patterns were used. Scherrer's equation [18] was used to calculate crystallite sizes. At least three specimens per group ($n \geq 3$) were tested for the values presented.

### 3.4.8. TGA

Samples were powdered in a mortar, after which thermogravimetry was performed using an STA 449F5 simultaneous thermal analyzer (Netzsch). Analyses were performed in air, using a temperature range of 25–1000 °C and a heating rate of 10 °C min$^{-1}$. At least three specimens per group ($n \geq 3$) were tested for the values presented.

### 3.4.9. TEM

Transmission electron microscopy powdered samples were transferred onto an amorphous carbon-coated copper grid. TEM, HRTEM (high-resolution TEM), and SAED (selected area electron diffraction) analyses were carried out with a JEM3200 FSC transmission electron microscope operating at 300 kV. Jade software (Jade 6.5) was used to identify the polymorphs and crystalline lattice distances. At least two specimens per group ($n \geq 2$) were tested.

### 3.4.10. NANO- AND MICROINDENTATION

Specimens for nano- and microindentation were removed from PMMA slides, embedded in an epoxy resin (Epofix Cold-Setting Embedding Resin), and polished with decreasing grades of polishing papers (SiC foils #1200, #2000, and #4000, Struers) and diamond pastes (DP-Paste M 6, 3, and 1 µm, Struers) on a cloth to obtain a mirror surface. Samples were embedded such that layered structures (*M. edulis* nacre and bacterial nacre) were arranged perpendicularly to the indentation direction.

Indentations were performed using a Hysitron Triboindenter (nanoindentation, Berkovich tip) and a Anton Paar microindenter (microindentation, Berkovich, and spherical tip). The use of two types of indentation tips—Berkovich and spherical—allowed for cross-validation of results; the area of contact for the spherical tip (100 µm radius) was larger than for the Berkovich tip (apex approximately 150 nm) at the same indentation depth.



Trapezoidal load-controlled protocols with a 10 s holding phase at the maximal load were used in all indentations. Nanoindentation maximal load was 10 mN, resulting in a final indentation depth of approximately 300 nm depending on the sample stiffness. Microindentation maximal load was 1 N (spherical tip), resulting in a final indentation depth of approximately 6 µm depending on the sample group, and 100 mN (Berkovich and spherical tips), resulting in approximate final depths of 1.3 and 4 µm, respectively. At least three specimens per group were indented 20–90 times each (at least 60 indents per sample type) for the values presented.

The indentation modulus ($E_{it}$) was calculated from the unloading slope following the method given by Oliver and Pharr [33], via a tip area function calibrated on fused silica or BK-7 glass standard samples for Berkovich tips (for the Hysitron Triboindenter and Anton Paar microindenter) and using a perfect tip shape assumption of 100 µm radius for the spherical tip (Anton Paar microindenter):

$$E_{it} = \frac{1-(\nu_s)^2}{\frac{1}{E_r} - \frac{1-(\nu_i)^2}{E_i}}$$

Where $\nu_s$ is the Poisson's ratio of the sample, $\nu_i$ the Poisson's ratio of the indenter tip, and $E_i$ the stiffness modulus of the indenter tip. $E_r$ represents the reduced modulus resulting from the indentation data, related to the compliance of sample-indenter contact and the projected contact area [33].

### 3.4.11. THREE-POINT BENDING

Three-point bending tests were performed on an Instron (3365) universal testing machine using a 1 kN load cell. Un-notched samples with a length of 75 mm and a width of 25 mm deposited on PMMA slides (75 × 25 × 0.4 mm, sample facing downwards) were tested using a support span of 40 mm and a monotonic loading rate of 0.1 mm min$^{-1}$. Sandpaper (SiC foil #1200, Struers) was used to remove any possible mesoscopic roughness on sample surfaces. Due to technical difficulties in obtaining flat samples of natural *M. edulis* nacre with the required dimensions (75 × 25 mm), these were not tested with three-point bending. At least three specimens per group were tested for the values presented ($n \geq 3$). The average thickness of each sample was defined from SEM

images (from 10 zones each of 10 SEM images taken along the entire cross-section) using ImageJ software (1.50i, National Institute of Health, USA). The mechanical behavior of the bi-layer samples (substrate PMMA slides with deposited samples) was analyzed using classical lamination theory [34] and video data from the tests. The geometrical parameters of the bi-layer samples and the elastic modulus of the substrate PMMA slides ($E$ = 1800 MPa) were assessed, after which the elastic and failure properties of the deposited samples were determined from force-displacement curves (Figure 3.12). The initial slope ($m$) of the force-displacement curves was modeled as:



$$m = \frac{AD - B^2}{A}$$

where $A$, $B$, and $D$ are the extensional, coupling, and bending stiffness:

$$A = E_1 h_1 + E_2 h_2$$
$$B = h_1 h_2 (E_2 - E_1)/2$$
$$D = \frac{1}{12}[E_1(h_1^3 + 3h_1 h_2^2) + E_2(h_2^3 + 3h_1^2 h_2)]$$

and $h_1$, $h_2$, $E_1$, and $E_2$ are the thickness and elastic moduli of substrate and coating (the macroscopic flexural stiffness), respectively. Extensibility (strain at failure, $\epsilon_f$) was calculated as the maximum strain at the macroscopic failure crack in the bacterial $CaCO_3$ and chemically-produced samples, and the maximum strain at the initial fracture point in the bacterial nacre samples ($\epsilon_f = 6d(h_1 + h_2)/L^2$, where $d$ is the maximum deflection and $L$ the support span, respectively), where no macrocrack was clearly observed. The initial fracture point was defined to be the point at which the force-displacement slope equaled the slope of an empty PMMA slide tested under the same conditions; the points were confirmed by video analyses. Toughness was calculated as the total deformation energy [35] until the initial crack (bacterial nacre samples) and failure crack (bacterial $CaCO_3$ and chemically-precipitated samples).

### 3.4.12. STATISTICS

Statistical analyses were performed with Gnumeric software (v. 1.10.16). Sample normality was tested using Anderson-Darling tests and qq plots. Normally distributed samples are presented as means ± standard deviations. Samples for which normality could not be ensured are presented as medians ± interquartile range. Samples were compared using one-way (single factor) ANOVA tests and post-hoc Tukey's HSD (honest significant difference) tests, with a significance level of $\alpha = 0.05$.

## 3.5. AUTHOR CONTRIBUTIONS

E.M.S. and D.T.S. developed the methods for materials production, produced the samples, and performed data analyses. A.M.G. analyzed the 3-point bending experiments. K.L. contributed to samples preparation and analysis. J.S. performed the nano-indentation experiments. A.M.G., F.N., J.S., J.M., and S.J.G. provided technical and scientific advice and assisted in the manuscript preparation. M.-E.A.T. and A.S.M. supervised the

project and assisted in manuscript preparation. All authors have read and corrected the manuscript.

## 3.6. ACKNOWLEDGMENTS

We would like to acknowledge Ruud Hendrikx for X-ray analysis, Marlies Nijemeisland for assistance with thermogravimetry experiments, Wiel Evers for TEM analysis, Roland Kieffer for support with the experimental set-up, An-Wu Xu for comments, Nadine Bongaerts for the image of PGA, Daniel Tam for helpful suggestions and Koen Pieterse for help in schematic drawing.



## REFERENCES

[1] S. Weiner and L. Addadi, *Crystallization pathways in biomineralization,* Annual Review of Materials Research **41**, 21 (2011).

[2] P. Fratzl, O. Kolednik, F. D. Fischer, and M. N. Dean, *The mechanics of tessellations - bioinspired strategies for fracture resistance,* Chemical Society Reviews **45**, 252 (2016).

[3] U. G. K. Wegst, H. Bai, E. Saiz, A. P. Tomsia, and R. O. Ritchie, *Bioinspired structural materials,* Nature Materials **14**, 23 (2015).

[4] R. Z. Wang, Z. Suo, A. G. Evans, N. Yao, and I. A. Aksay, *Deformation mechanisms in nacre,* Journal of Materials Research **16**, 2485 (2001).

[5] J. R. Rodrigues, N. M. Alves, and J. F. Mano, *Nacre-inspired nanocomposites produced using layer-by-layer assembly: Design strategies and biomedical applications,* Materials Science and Engineering: C **76**, 1263 (2017).

[6] H.-L. Gao, S.-M. Chen, L.-B. Mao, Z.-Q. Song, H.-B. Yao, H. Cölfen, X.-S. Luo, F. Zhang, Z. Pan, Y.-F. Meng, Y. Ni, and S.-H. Yu, *Mass production of bulk artificial nacre with excellent mechanical properties,* Nature Communications **8**, 287 (2017).

[7] L.-B. Mao, H.-L. Gao, H.-B. Yao, L. Liu, H. Cölfen, G. Liu, S.-M. Chen, S.-K. Li, Y.-X. Yan, Y.-Y. Liu, and S.-H. Yu, *Synthetic nacre by predesigned matrix-directed mineralization,* Science (2016), 10.1126/science.aaf8991.

[8] S. Y. Choi, S. J. Park, W. J. Kim, J. E. Yang, H. Lee, J. Shin, and S. Y. Lee, *One-step fermentative production of poly(lactate-co-glycolate) from carbohydrates in escherichia coli,* Nature biotechnology **34**, 435 (2016).

[9] Y. Poirier, C. Nawrath, and C. Somerville, *Production of polyhydroxyalkanoates, a family of biodegradable plastics and elastomers, in bacteria and plants,* Nature Biotechnology **13**, 142 (1995).

[10] P. Anbu, C.-H. Kang, Y.-J. Shin, and J.-S. So, *Formations of calcium carbonate minerals by bacteria and its multiple applications,* SpringerPlus **5**, 250 (2016).

[11] F. Barthelat, *Growing a synthetic mollusk shell,* Science **354**, 32 (2016).

[12] C. Rodríguez-Navarro, E. Ruiz-Agudo, J. Harris, and S. E. Wolf, *Nonclassical crystallization in vivo et in vitro (ii): Nanogranular features in biomimetic minerals disclose a general colloid-mediated crystal growth mechanism,* JSB 50th Anniversary Issue **196**, 260 (2016).

[13] M. Morikawa, S. Kagihiro, M. Haruki, K. Takano, S. Branda, R. Kolter, and S. Kanaya, *Biofilm formation by a bacillus subtilis strain that produces gamma-polyglutamate,* Microbiology (Reading, England) **152**, 2801 (2006).

[14] R. Chettri, M. O. Bhutia, and J. P. Tamang, *Poly-gamma-glutamic acid (pga)-producing bacillus species isolated from kinema, indian fermented soybean food,* Frontiers in Microbiology **7**, 971 (2016).

[15] S.-S. Wang, A. Picker, H. Cölfen, and A.-W. Xu, *Heterostructured calcium carbonate microspheres with calcite equatorial loops and vaterite spherical cores,* Angewandte Chemie International Edition **52**, 6317 (2013).

[16] T. Kato, *Polymer/calcium carbonate layered thin-film composites,* Advanced Materials **12**, 1543 (2000).

[17] S. Wu, C.-Y. Chiang, and W. Zhou, *Formation mechanism of caco3 spherulites in the myostracum layer of limpet shells,* Crystals **7**, 319 (2017).

[18] Y.-Y. Kim, A. S. Schenk, J. Ihli, A. N. Kulak, N. B. J. Hetherington, C. C. Tang, W. W. Schmahl, E. Griesshaber, G. Hyett, and F. C. Meldrum, *A critical analysis of calcium carbonate mesocrystals,* Nature communications **5**, 4341 (2014).

[19] X. Qian, C. Fang, M. Huang, and V. Achal, *Characterization of fungal-mediated carbonate precipitation in the biomineralization of chromate and lead from an aqueous solution and soil,* Journal of Cleaner Production **164**, 198 (2017).

[20] F. C. Meldrum and H. Cölfen, *Controlling mineral morphologies and structures in biological and synthetic systems,* Chemical Reviews **108**, 4332 (2008).

[21] N. Spanos and P. G. Koutsoukos, *The transformation of vaterite to calcite: effect of the conditions of the solutions in contact with the mineral phase,* Journal of Crystal Growth **191**, 783 (1998).

[22] E. M. Spiesz, A. G. Reisinger, P. Roschger, and P. K. Zysset, *Experimental validation of a mean filed model of mineralized collagen fiber arrays at two levels of hierarchy,* Journal of Mechanics in Medicine and Biology **14**, 1450013 (2014).

[23] A. Finnemore, P. Cunha, T. Shean, S. Vignolini, S. Guldin, M. Oyen, and U. Steiner, *Biomimetic layer-by-layer assembly of artificial nacre,* Nature Communications **3**, 966 (2012).

[24] J. Malzbender and R. W. Steinbrech, *Mechanical properties of coated materials and multi-layered composites determined using bending methods,* Surface and Coatings Technology **176**, 165 (2004).

[25] I. Corni, T. J. Harvey, J. A. Wharton, K. R. Stokes, F. C. Walsh, and R. J. K. Wood, *A review of experimental techniques to produce a nacre-like structure,* Bioinspiration & Biomimetics **7**, 031001 (2012).

[26] X. Li, Z.-H. Xu, and R. Wang, *In situ observation of nanograin rotation and deformation in nacre,* Nano Lett **6**, 2301 (2006).

[27] S. Askarinejad and N. Rahbar, *Toughening mechanisms in bioinspired multilayered materials,* Journal of The Royal Society Interface **12** (2014), 10.1098/rsif.2014.0855.

[28] F. Natalio, T. P. Corrales, S. Wanka, P. Zaslansky, M. Kappl, H. P. Lima, H.-J. Butt, and W. Tremel, *Siliceous spicules enhance fracture-resistance and stiffness of pre-colonial amazonian ceramics,* Scientific Reports **5**, 13303 (2015).

[29] P. Q. Nguyen, *Synthetic biology engineering of biofilms as nanomaterials factories,* Biochemical Society Transactions **45**, 585 (2017).

[30] L. Brown, T. Koerner, Horton, J. Hugh, and R. D. Oleschuk, *Fabrication and characterization of poly(methylmethacrylate) microfluidic devices bonded using surface modifications and solvents,* Lab Chip **6**, 66 (2006).

[31] G. Kedia, D. Hill, R. Hill, and I. Radecka, *Production of poly-gamma-glutamic acid by bacillus subtilis and bacillus licheniformis with different growth media,* Journal of Nanoscience and Nanotechnology **10**, 5926 (2010).

[32] N. Doebelin and R. Kleeberg, *Profex: a graphical user interface for the rietveld refinement program bgmn,* Journal of applied crystallography **48**, 1573 (2015).

[33] W. C. Oliver and G. M. Pharr, *Measurement of hardness and elastic modulus by instrumented indentation: Advances in understanding and refinements to methodology,* Journal of Materials Research **19**, 3 (2004).

[34] S. Timoshenko, *Analysis of bi-metal thermostats,* Journal of the Optical Society of America **11**, 233 (1925).

[35] C. McGowan, *A practical guide to vertebrate mechanics* (Cambridge University Press, 1999).

# 4

# METHODS FOR THE PATTERNING OF BACTERIA

In the preceding chapters, a method for the production of bacterial nacre was demonstrated that is based on layer-by-layer assembly. However, this method is slow and labor-intensive, so that a procedure is desirable that mimics the natural growth of nacre in an organic matrix. To achieve this goal, bacteria have to be patterned in 3D space. Different methods have been described in the literature, from the direct deposition of bacteria by inkjet printing or stamps, over simple modification of surfaces that allow bacteria to adhere, to complex genetic engineering to control biofilm formation through chemical inducers and light. These different methods come all with their own sets of advantages and drawbacks, but all of them lack the ability to pattern bacteria in macroscopic structures in all three dimensions.

## 4.1. INTRODUCTION

Natural nacre is produced by a dedicated secretory epithelium in the extrapallial space [1]. The aragonite tablets grow under tight control in a pre-formed matrix [2]. Thus, the procedure to produce bacterial nacre demonstrated in Chapters 2 and 3 differs considerably from natural nacre growth, since bacterial nacre was produced in an LbL approach with planktonic bacteria. The LbL approach is relatively slow and work-intensive. If the natural method could be imitated, the procedure could be sped up considerably and potentially produce an improved material. The first step towards this goal is the controlled arrangement of bacterial cells in space, to mimic animal tissues. A subsequent differentiation of the bacteria to perform different tasks could be used to grow new composite materials. Alternatively, different bacteria (either different species or strains with different genetic modifications) could be arranged together in specified patterns. Different approaches for the patterning of bacteria have been developed and will be discussed here. In Chapters 5 and 6, a method based on 3D printing will be demonstrated.



## 4.2. MECHANICAL DEPOSITION OF BACTERIA

With the high precision of machines used in printing and microfabrication, the small size of bacteria becomes less of a confounding factor in patterning, allowing for approaches where bacteria can be placed directly by a pumping system or tiny, microfabricated structures. Xu *et al.* [3] employed commercial inkjet printers to deposit suspensions of *E. coli* onto agar-coated glass slides, reaching resolutions of 100 colonies/cm$^2$, and achieving single cells per droplet by adjusting the concentration of cells in the printed suspension. Despite the high temperatures used in the printheads to generate droplets, viable bacteria were printed. Zheng *et al.* [4] used the same method to print bacterial dots with a diameter of 100 µm and a density of 400 dots/cm$^2$ onto agar-coated glass slides. By printing gradients of antibiotic solutions, inkjet printing was used as a high-throughput replacement of the traditional disc diffusion method for the determination of the minimum inhibitory concentration. Inkjet printing is a compelling technique, due to the low cost of commercial printers, their high precision, the ability of control with standard software, and the ease of modification for biological purposes. Challenges arise from cross-contamination when more than one species/strain is printed, the difficulty of sterilization of e.g. the print head, and clogging through dried growth medium components or carrier substances.

Xu *et al.* [5] microfabricated PDMS stamps with pillars of down to 1 µm diameter to transfer cells from a lawn of *E. coli* onto an agarose substrate, producing arrays of groups of bacteria. By reducing the number of bacteria in the initial bacteria lawn, arrays of bacteria with single-cell resolution could be produced. Eun *et al.* [6] fabricated PDMS stencils to produce arrays of biofilms of several gram-positive and negative bacteria species on different substrates. The technique is suitable for batch culture, as well as culture in microfluidics devices. The smallest generated diameter of biofilm was 50 µm, but further down-scaling is expected to be possible. The maximum thickness of the biofilm measured was 40 µm. Microfabricated tools allow for very high resolutions, but scale-up and the use of different cells types can be a challenge. Furthermore, special microfabrication facilities and trained staff are required to produce the stamps and stencils.

## 4.3. SELECTIVE ADHESION OF BACTERIA TO MODIFIED SURFACES

Bacterial patterning can be achieved through selective modifications of a surface in contact with a liquid bacteria culture. Suo *et al.* [7] coated silicon and gold substrates with PEG and used $Ga^{2+}$ ion beam etching to expose specific areas for the attachment of a crosslinker. This crosslinker, in turn, bound antibodies specific to the CFA/I fimbriae of *Salmonella enterica* serovar Typhimurium. When the thus prepared substrates were incubated in a liquid culture of *S.* Typhimurium, the bacteria selectively attached to the antibody-coated areas and could be kept alive for at least 3 days on the substrate. The use of antibodies allows for a high selectivity of attachment, which was demonstrated by incubation of the substrate in a mixture of *Salmonella* and *E. coli*. *E. coli* was not bound by the immobilized antibody and could be washed away. The drawback of this method is the requirement of an antibody that binds efficiently to a surface structure of the bacterium.



If high selectivity is not required, simpler surface modifications can be employed. For example, Palacios-Cuesta *et al.* [8] cross-linked a mixture of polystyrene and an amphiphilic block copolymer with the help of UV light and a copper-grid mask on polystyrene surfaces. This procedure resulted in defined areas of increased surface hydrophilicity, which were bound selectively by *Staphylococcus aureus* when submerged in a liquid culture. Due to the high resolution of the technique (below the size of *S. aureus*), single bacteria could be immobilized on the surface, which is exceedingly hard due to *S. aureus*' tendency to form clusters.

The most important advantage of modifying surfaces is that substrates are modified, not cells. This fact allows for a large range of tools to be used, such as microfabrication techniques, UV light, and toxic chemicals, resulting in very high resolutions down to features of a single-cell width. Furthermore, no genetic engineering is required, and selectivity can be tuned depending on the application, from simple increase of surface hydrophilicity to the use of very selective antibodies, of which many are commercially available. Depending on the complexity and dimensions of the pattern, microfabrication techniques for the modification of the substrate or the production of the masks can be required. The ability to reliably pattern more than one species/strain of bacteria on the same substrate remains to be proven.

## 4.4. BACTERIAL PATTERNING WITH CHEMICAL INDUCERS AND GENETIC CIRCUITS

Initially-homogeneous groups of bacteria can be induced to express genes differentially under control of chemical inducers, either externally applied or self-produced. This approach opens the possibility to employ a large range of natural abilities in new ways, e.g. quorum sensing systems for inter-cell communication, sensors for chemical perception, and genetic logic gates for signal integration—resulting in emergent patterning that is comparable to the development of animal tissues.

Kong *et al.* [16] modified bacteria to form patterns under external control of the antibiotic nisin. *Lactobacillus lactis* was transformed with a plasmid for the constitutive

expression of the nisin-reactive two-component system NisKR, as well as the NisR-inducible expression of a fluorescent reporter. This genetic setup resulted in three different nisin-dependent activation states: in absence of nisin, the bacteria expressed no fluorescent protein, at medium induction levels fluorescent protein was produced, and at high induction levels, the cells were killed off by the antibiotic, preventing the development of fluorescence. Nisin-infused masks placed in proximity of thus engineered bacterial lawns were used to control pattern formation. The authors demonstrated the robustness of their method in different conditions (nutrient supply, pH, temperature, oxygen supply), as well as its tunability: the thickness of the fluorescent areas could be varied by changing the nisin concentration, as well as introducing a nisin resistance gene into the bacteria. Furthermore, bacteria engineered to produce nisin were co-seeded with the nisin-reactive cells, resulting in the production of different fluorescent shapes, such as lines and arrays of spots, depending on the original seeding shape.



Basu *et al.* [17] engineered *E. coli* to the express green fluorescent protein (GFP) in dependence of an acyl-homoserine lactone (AHL) gradient, detected by the transcriptional activator LuxR in combination with a genetic circuit containing three transcriptional inhibitors of different strengths. Only at intermediate AHL levels, GFP was derepressed, leading to a circular fluorescence pattern in a lawn of bacteria at a specific distance from AHL-producing bacteria. By employing LuxR variants of different sensitivities, the distance of the fluorescent pattern to the AHL-source was varied, and by mixing strains with two LuxR variants and two different fluorescent proteins, a bulls-eye pattern could be established. More complex patterns could be produced by addition of AHL sources at specific locations.

Liu *et al.* [18] engineered *E. coli* cells to grow in rings of alternating high and low cell density. A cell density-sensing module based on the quorum sensing system of *Vibrio fischeri* was used to control the expression of CheZ in a CheZ-deficient strain. At high cell concentrations, CheZ was repressed by the AHC-controlled inhibitor CI, leading to impaired cells movement and accumulation of cells, while at low densities, CI expression was stopped, allowing cells to maintain the ability to move. When seeded from a single point, cells grew out radially and developed alternating stripes of high and low cell density with a wavelength of 0.5 cm. The wavelength of the pattern could be tuned by introducing a second CI gene behind an anhydrotetracycline (ATC)-activated promoter, and the addition of ATC to the growth medium.

Boehm *et al.* [15] created a synthetic genetic circuit for *E. coli* that acts as an AND gate, reacting to the presence of two homoserine lactones, which are signaling molecules in the quorum sensing systems of *Vibrio fischeri* and *Pseudomonas aeruginosa*. The authors demonstrated a three-color expression system based on this circuit in both liquid culture and surface culture cells, where CFP was expressed in the presence of one lactone, YFP in the presence of the other, and RFP in presence of both.

Genetic engineering and control with chemicals were shown to be efficient at inducing bacterial patterning, and with the ever-increasing number of sequenced and examined genetic systems, it is likely that this technique is going to be used extensively in the future. However, some drawbacks remain, which might render this technique non-ideal in some circumstances. For example, the patterned bacteria need to be engineered, noisy logic gates might be needed, the number of variants of e.g. quorum sensing pro-

teins and sensors is limited, and control is realized by diffusing inducers. Together, these factors make fine-tuning and up-scaling of the patterning systems slow and laborious.

## 4.5. CONTROL OF BACTERIAL PATTERNING WITH LIGHT

Chemical inducers were shown to be useful tools in pattern formation, but they are subject to the laws of diffusion, resulting in slow spread over longer distances, loss of directionality, and difficult control over the induction strength in different regions of the culture. A promising alternative to chemical inducers is the control of pattern formation with light. For example, chemical bonds can be produced or dissolved, resulting in attachment to or detachment from a surface, or formation of an encasing gel. Alternatively, the expression of genes can be controlled with light-sensing systems from e.g. cyanobacteria or algae.



Connell *et al.* [19] developed a method to encapsulate wildtype bacteria in arbitrarily-shaped 3D micro-environments using a laser-based lithography technique. Bacteria were suspended in a solution containing gelatin, BSA and a photosensitizer at 37 °C, which formed a gel when cooled down to room temperature. Multiphoton lithography was then used to cross-link gelatin and BSA at the focus points of the laser, followed by a washing step with growth medium to remove non-crosslinked components. This technique allowed for the fabrication of compartments of different shapes, such as boxes, spheres, or combinations with micrometer resolution. While the structural components were permissive for e.g. nutrients and antibiotics, bacteria were reliably contained within the compartments. To demonstrate the application of thus-produced micro-compartments for the investigation of bacteria interactions on a species level, a colony of *Staphylococcus aureus* was surrounded by a colony of *Pseudomonas aeruginosa*, the latter of which effectively protected the *S. aureus* cells from the action of the beta-lactam antibiotic ampicillin.

Pu *et al.* [9] exploited the natural ability of bacteria to attach to surfaces through biofilm formation. The blue light sensing system pDawn was integrated into the genome of *Pseudomonas aeruginosa*, controlling the expression of a phosphodiesterase that degrades cyclic dimeric GMP (c-di-GMP), a central signaling molecule for biofilm formation. A biofilm formed in a flow cell from thus engineered bacteria could be dissolved efficiently by exposure with blue light. To achieve high-resolution bacterial patterning by light control, Huang *et al.* [10] refined this method by controlling both c-di-GMP formation, as well as degradation, with red and blue light, respectively. Cells were grown in a flow cell system under continuous culture, and a micromirror-based projector was employed to illuminate some areas with red light, and the complementary areas with blue light, resulting in selective biofilm formation in the red light areas within 6 hours of culture.

Jin and Riedel-Kruse [11] engineered *E. coli* to express adhesin 43 (Ag43) under blue light illumination by placing the *agn43* gene behind the light-inducible promoter pDawn. With the help of a mini-projector affixed to an incubator, control over *E. coli* biofilm formation in polystyrene well plates, as well as on PDMS and glass coupons was achieved with a maximum resolution of 25 µm. Modeling results suggested that expression of Ag43 led to the improved attachment of transiently attached cells to the substrate, instead of improved attachment of planktonic cells.

Chen and Wegner [12] used the reversible, photoswitchable interaction of the proteins nMag and pMag to control bacterial adhesion to surfaces. nMag and pMag form heterodimers under exposure of blue light, which dissociate in dark conditions. pMag was expressed as a surface-displayed protein in *E. coli* while isolated nMag was conjugated to PEG-coated glass-substrates with the help of a 6-His-tag. With a photomask, the authors induced the bacteria to adhere in controlled patterns to the substrates, a process which could be reversed and repeated several times. Furthermore, it was demonstrated that the number of bacteria and the adhesion/dissociation kinetics could be tuned by employing different mutants of pMag, and by varying the attachment time or light intensity.

Velema *et al.* [20] exploited the different antibiotic susceptibilities of *E. coli* and *Micrococcus luteus* to pattern the bacteria on agar plates. The agar was supplemented with a photo-activated antibiotic, which was selectively activated with a mask and a UV lamp, resulting in different antibiotic concentrations, depending on the length of UV exposure. A mixture of *E. coli* and *M. luteus* plated on these plates resulted in areas where *M. luteus* grew exclusively due to its high resistance to the antibiotic, and mixed areas where both bacteria survived.



Tabor *et al.* [13] created a genetic edge detection algorithm, which induced cells in a lawn of *E. coli* bacteria to express a gene when located at the dark-light edges of a projected image. Cells located in the dark areas generated the extracellular quorum sensing molecule AHL that activated the expression of the reporter gene, as well as the intracellular inhibitor CI, which strongly inhibits reporter gene expression. Consequently, cells in the dark did not express the reporter gene, but AHL could diffuse to cells in light conditions. Cells located in the light areas expressed neither AHL nor CI and were thus receptible to activation through AHL. As a result, illuminated cells close to unilluminated cells were induced by AHL to express the reporter gene, while the activation of more distant cells was limited by the diffusion speed of AHL. Later, Tabor *at al.* [14] combined the cyanobacterial green light sensing system CcaS/R with a red light-activated chimera of Cph1 and EnvZ, generating a four-state system that is controlled by exposure with green and/or red light, allowing for the light controlled genetic patterning of a lawn of bacteria.

Control with light allows for high-resolution patterning with stringent control, but much like all other methods described in this chapter, the absolute dimensions of the produced bacterial patterns are small, usually in the millimeter to centimeter range in one plane (x/y-plane), but only in the tens of micrometer range in the z-direction. Consequently, these methods are not suitable for patterning of bacteria in larger volumes—an important pre-requisite for producing bacterial nacre for practical applications. In the following two chapters, a possible solution is presented: the patterning of bacteria through additive manufacturing, i.e. 3D printing.

## REFERENCES

[1] F. Heinemann, M. Launspach, K. Gries, and M. Fritz, *Gastropod nacre: Structure, properties and growth — biological, chemical and physical basics,* Biophysical Chemistry **153**, 126 (2011).

[2] F. Nudelman, *Nacre biomineralisation: A review on the mechanisms of crystal nucleation,* Biomineralisation & Motorisation of pathogens **46**, 2 (2015).

[3] T. Xu, S. Petridou, E. H. Lee, E. A. Roth, N. R. Vyavahare, J. J. Hickman, and T. Boland, *Construction of high–density bacterial colony arrays and patterns by the ink–jet method,* Biotechnology and Bioengineering **85**, 29 (2004).

[4] Q. Zheng, J. Lu, H. Chen, L. Huang, J. Cai, and Z. Xu, *Application of inkjet printing technique for biological material delivery and antimicrobial assays,* Analytical biochemistry **410**, 171 (2011).

[5] L. Xu, L. Robert, Q. Ouyang, F. Taddei, Y. Chen, A. B. Lindner, and D. Baigl, *Microcontact printing of living bacteria arrays with cellular resolution,* Nano Lett **7**, 2068 (2007).

[6] Y.-J. Eun and D. B. Weibel, *Fabrication of microbial biofilm arrays by geometric control of cell adhesion,* Langmuir **25**, 4643 (2009).

[7] Z. Suo, R. Avci, X. Yang, and D. W. Pascual, *Efficient immobilization and patterning of live bacterial cells,* Langmuir **24**, 4161 (2008).

[8] M. Palacios-Cuesta, A. L. Cortajarena, O. García, and J. Rodríguez-Hernández, *Patterning of individual staphylococcus aureus bacteria onto photogenerated polymeric surface structures,* Polymer Chemistry **6**, 2677 (2015).

[9] L. Pu, S. Yang, A. Xia, and F. Jin, *Optogenetics manipulation enables to prevent biofilm formation of engineered pseudomonas aeruginosa on surfaces,* ACS Synthetic Biology **69**, 200 (2017).

[10] Y. Huang, A. Xia, G. Yang, and F. Jin, *Bioprinting living biofilms through optogenetic manipulation,* ACS Synthetic Biology **7**, 1195 (2018).

[11] X. Jin and I. H. Riedel-Kruse, *Biofilm lithography enables high-resolution cell patterning via optogenetic adhesin expression,* Proceedings of the National Academy of Sciences , 201720676 (2018).

[12] F. Chen and S. V. Wegner, *Blue light switchable bacterial adhesion as a key step toward the design of biofilms,* ACS Synthetic Biology **6**, 2170 (2017).

[13] J. J. Tabor, H. M. Salis, Z. B. Simpson, A. A. Chevalier, A. Levskaya, E. M. Marcotte, C. A. Voigt, and A. D. Ellington, *A synthetic genetic edge detection program,* Cell **137**, 1272 (2009).

[14] J. J. Tabor, A. Levskaya, and C. A. Voigt, *Multichromatic control of gene expression in escherichia coli,* Journal of Molecular Biology **405**, 315 (2011).

[15] C. R. Boehm, P. K. Grant, and J. Haseloff, *Programmed hierarchical patterning of bacterial populations,* Nature communications **9**, 776 (2018).

[16] W. Kong, A. E. Blanchard, C. Liao, and T. Lu, *Engineering robust and tunable spatial structures with synthetic gene circuits,* Nucleic Acids Research **45**, 1005 (2017).

[17] S. Basu, Y. Gerchman, C. H. Collins, F. H. Arnold, and R. Weiss, *A synthetic multicellular system for programmed pattern formation,* Nature **434**, 1130 (2005).

[18] C. Liu, X. Fu, L. Liu, X. Ren, C. K. Chau, S. Li, L. Xiang, H. Zeng, G. Chen, L.-H. Tang, P. Lenz, X. Cui, W. Huang, T. Hwa, and J.-D. Huang, *Sequential establishment of stripe patterns in an expanding cell population,* Science **334**, 238 (2011).

[19] J. L. Connell, E. T. Ritschdorff, M. Whiteley, and J. B. Shear, *3d printing of microscopic bacterial communities,* Proceedings of the National Academy of Sciences **110**, 18380 (2013).

[20] W. A. Velema, Berg, Jan Pieter van der, W. Szymanski, A. J. M. Driessen, and B. L. Feringa, *Bacterial patterning controlled by light exposure,* Organic & Biomolecular Chemistry **13**, 1639 (2015).

# 5

# A Straightforward Approach for 3D Bacterial Printing

**Benjamin A. E. Lehner, Dominik T. Schmieden, and Anne S. Meyer**

Sustainable and personally-tailored materials production is an emerging challenge to society. Living organisms can produce and pattern an extraordinarily wide range of different molecules in a sustainable way. These natural systems offer an abundant source of inspiration for the development of new environmentally-friendly materials production techniques. In this chapter, we describe the first steps toward the 3-dimensional printing of bacterial cultures for materials production and patterning. This methodology combines the capability of bacteria to form new materials with the reproducibility and tailored approach of 3D printing systems. For this purpose, a commercial 3D printer was modified for bacterial systems, and a bacterial bioink was developed. Printing temperature, printhead speed, and bioink extrusion rate were all adapted and customized to maximize bacterial health and spatial resolution of printed structures. Our combination of 3D printing technology with biological systems enables a sustainable approach for the production of numerous new materials. In combination with bacteria-induced biomineralization, 3D printing could be used to speed up the time-consuming layer-by-layer process described earlier to produce new materials such as bacterial nacre.

Parts of this chapter have been published in ACS Synthetic Biology 6.7 (2017): 1124–1130 [1].

## 5.1. INTRODUCTION

The development of more sustainable materials production is an urgent need for our current society. Traditional materials production processes can utilize massive quantities of polluting chemicals, and too often the products are not naturally degradable [2]. One newly emerging approach to solve this problem is the production of materials by bacteria, either genetically modified [3–5] or unmodified [6, 7]. Many bacteria can carry out advanced chemical reactions to produce materials, including amyloid-based adhesives [8], biobased electrical switches [9], and a variety of bioplastics [10], under ambient conditions without using or producing toxic compounds. However, current microbial materials production techniques do not allow the generation of bespoke material structures in a reliable or reproducible way. To allow for the production of complex patterned biomaterials, we have coupled bacterial materials production with 3D printing technology [11].

Additive manufacturing allows for the production of tailored products fulfilling individual needs and enables entrepreneurs and companies to produce small batches or only on-demand [12]. A wide variety of 3D printing approaches have been developed for additive manufacturing of non-biological materials, including stereolithography, selective laser sintering, electron beam melting, Laser Engineered Net Shaping, and PolyJet [13, 14]. The vast majority of current 3D printing techniques involve one or more steps that are deadly for cells. Therefore, new technologies have been developed for cellular printing with medical and biological applications including visualization, education, and transplantationb[15–17]. To date, these techniques are quite expensive ($5000–200 000 [18]) and not yet well adapted for bacteria.

The area of biological printing is primarily dominated by three different technologies. Thermal inkjet bioprinting uses CT or MRI images as guides to deploy fluid dots layer by layer, which solidify to a gel after a short heating phase in the extruder [19]. Direct write bioprinting utilizes print-heads made of syringes or needles that transport liquid bioink via mechanical or pneumatic systems and uses a low-melting-point scaffold material [20, 21]. Spheroid organ printing employs tiny tissue spheroids to assist the self-organizational and self-assembling character of real tissues [22]. A few efforts have been made to apply these technologies to bacterial printing, but all current approaches suffer limitations of poor spatial resolution [23] or require laborious clean-room fabrication of microstructures that shape the printed bacteria [24]. To achieve a cost-efficient technology for bacterial printing that is compatible with incubation of printed bacteria at elevated temperatures, a new technology must be developed that allows high printing resolution without the requirement for cleanroom facilities.

Our newly developed microbial 3D printer can deposit bacteria cells in specific three-dimensional patterns for the ultimate goal of materials production. Our printing platform uses a modified commercially available 3D printer to extrude a mixture of bacteria and alginate that solidifies into a gel upon contact with a calcium chloride-treated printing surface. This combination of straightforward chemistry and easy, readily available technology enabled us to print reproducible 3-dimensional samples with high spatial resolution. The combination of our straightforward technique to print 3D microbial structures with the material-modifying properties of bacteria will result in high-resolution deposition of bacteria and the fabrication of spatially patterned materials.

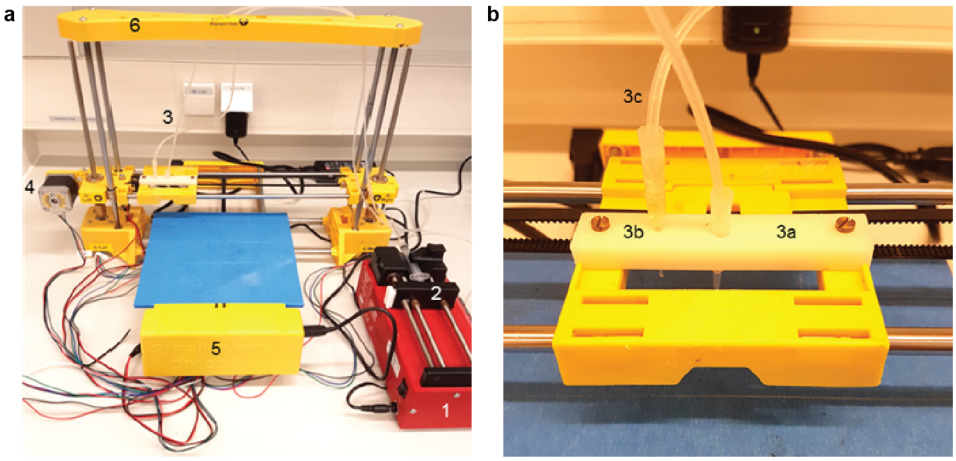


Figure 5.1: Bacterial 3D printing system (a) Overview of all bioprinter components. 1: syringe pump, 2: syringe filled with bioink, 3: extruder holder, 4: one of three step-motors for positioning, 5: breadboard and hardware of the printer, 6: frame of the printer. (b) Detailed view of the modified extruder. 3a: active pipette tip, 3b: secondary pipette tip for layering materials, 3c: tubing system.



## 5.2. RESULTS AND DISCUSSION

### 5.2.1. 3D PRINTER AND BIOINK

In order to create a straightforward bacterial 3D printer, multiple modifications were made to an inexpensive ($300) commercial 3D printer (Figure 5.1a). The extruder of the printer was removed and replaced with a pipette tip (Figure 5.1b, 3a) and a system of tubing (Figure 5.1b, 3c). This alteration allows the liquid biological ink ("bioink") to be transported under ambient temperatures that are amenable to microbes, rather than the elevated temperatures that are applied to melt plastic filament. A secondary pipette tip was affixed to the printhead (Figure 5.1b, 3b) to allow for rapid alternation between the deposition of different types of bioink. A syringe pump (Figure 5.1a, 1) was added to the system to generate continuous but adjustable flows of bioink through the sets of tubing into the pipette tips. Printed shapes are created through the flow of bioink through the movable printhead while it is in motion, the trajectory of which is programmably controlled by an external computer. The shape of printed objects can be created *in silico* through computer-aided design (CAD) software programs, then converted into printing instructions for the 3D printer using slicing and printer-specific software programs. These adaptations can be performed on all 3D printing systems that employ an accessible and removable extruder.

A custom bioink was developed that would allow bacteria and chemical substrates for materials production to flow through the printhead in liquid state, then rapidly solidify upon contact with the printing surface to form a stably patterned shape. The bioink consists of live bacteria mixed with dissolved alginate. When the bioink is extruded onto a surface containing calcium ions during the printing process, cross-linking of the alginate molecules is triggered, forming a stable, biocompatible hydrogel scaffold within seconds [25, 26]. In order to optimize the bioink composition, the alginate and calcium

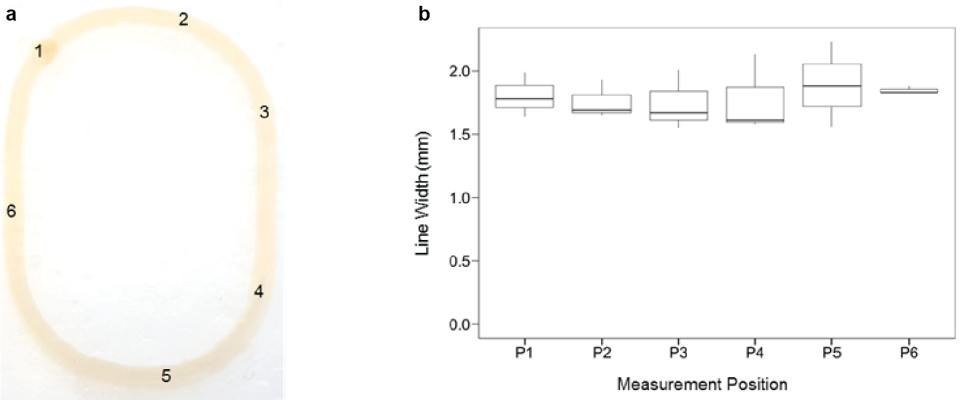


Figure 5.2: Reproducible printing of alginate structures (a) A representative printed elliptical structure. The numbers indicate the locations of the 6 measurement positions. (b) The distribution of measured line widths at 6 different positions within elliptical printed structures ($n = 3$). The tops and bottoms of the boxes represent the 75th and the 25th percentiles, respectively; the lines within the boxes are the median values; and the tops and bottoms of the vertical lines are the maximum and minimum values. No significant differences exist between the width distributions of any of the different positions (ANOVA, p-value: 0.036).



ion concentrations were systematically varied (from 0.5% w/v to 6% w/v alginate; and 0.0087 mol cm$^{-2}$ to 0.44 mol cm$^{-2}$ $CaCl_2$) and tested in the printing system. Insufficient concentrations of alginate and calcium ions resulted in poor gelation and low printing resolution, while excessive concentrations led to premature gelation of the bioink, blocking the pipette tip and preventing further printing. The optimal conditions were found to be 1 M $CaCl_2$ and 2.5% w/v alginate. With our printer system, each printed layer can only contain materials that are present in the active syringe; the mixture of materials from two different syringes within one layer is not possible due to the rate of scaffold formation. However, a wide range of different types of materials is compatible with alginate polymerization and may be admixed in the active syringe for inclusion in individual printed layers [21, 27].

### 5.2.2. PRINTING REPRODUCIBILITY AND RESOLUTION

The reproducibility and consistency of the printing process was assessed by analyzing patterned monolayers that were printed using the optimized bioink. An elliptical form with two long straight lines on each side was chosen as the printing object in order to test the performance of the printer in fabricating both curved and straight-edged structures (Figure 5.2a). Following printing, the width of each printed structure was measured at six different positions, sampling a variety of straight and curved portions. No statistically significant differences were seen among any of the widths measured at the same position in different prints (ANOVA, p-value: 0.964) (Figure 5.2b). These data indicate that our printer and bioink can fabricate printed structures of varying shapes in a consistently uniform manner.

In order to maximize the printer resolution, a range of printing parameters was tested. The two most critical factors affecting the printed line width were found to be the extru-

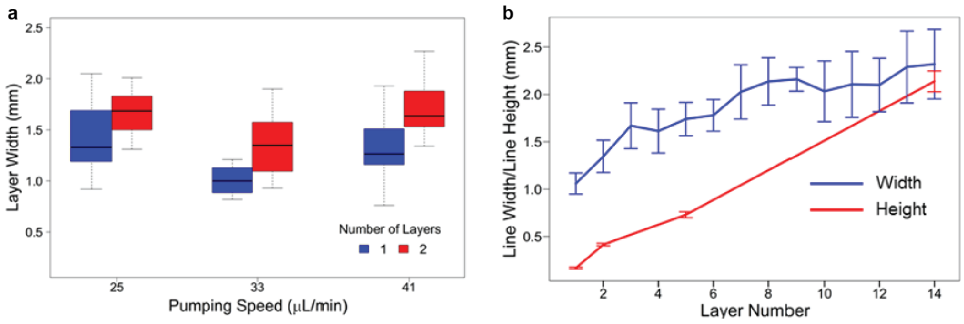


Figure 5.3: Printing at millimeter-scale resolution in three dimensions. (a) The distribution of widths of single- and double-layered structures printed at different syringe pump speeds ($n$ = 4). The printhead movement speed was 200 mm min$^{-1}$ in all cases. The tops and bottoms of the boxes represent the 75th and the 25th percentiles, respectively; the lines within the boxes are the median values; and the tops and bottoms of the vertical lines are the maximum and minimum values. (b) The line width (blue) and line height (red) of printed structures containing up to 14 layers ($n$ = 3). Error bars indicate the standard error.

5

sion rate of the syringe pump and the movement speed of the printhead, in agreement with previous work [28]. A range of printhead movement speeds (100–500 mm min$^{-1}$) and syringe pump extrusion rates (17–50 µL min$^{-1}$) were applied to print straight lines of bioink. In general, increased printing resolution could only be achieved by adjusting both parameters in parallel: e.g. slower printhead movement speeds required slower syringe pump rates. Other less-critical factors contributing to printer resolution were the distance between the printhead and the printing surface, as well as the uniformity of the printing surface. The narrowest line width obtainable was 1.00 ± 0.15 mm, achieved with a printhead movement speed of 200 mm min$^{-1}$ and a syringe pump extrusion rate of 33 µL min$^{-1}$ (Figure 5.3a).

The printer can be directed to deposit bioink directly on top of previously printed material to create multi-layered structures. A second hydrogel layer can be printed on top of a base layer at a range of different syringe pump extrusion rates, with no modification of the printing commands (Figure 5.3a). Fabrication of structures taller than two layers in height requires an increase of the z-position of the printhead by 0.15 mm/layer. Stacked layers of bioink are able to solidify due to interaction with calcium ions that have diffused from the printing surface up through the first printed layer(s). Each additional printed layer resulted in a fractional increase in the width of the final structure, due to the time required for the new layer to gelate (Figure 5.3a, b). No significant change in the final width was observed when the time between printing of successive layers was varied between 40 and 240 s (Student's t test, p-value: 0.037, CV40s: 18.36, CV240s: 20.82), indicating that multi-layered structures can be printed at different paces with no loss of resolution. The total time required to print a 14-layered ellipse with a pause of 40 s between printing successive layers was 15 min.

To characterize the spatial resolution of 3-dimensional printed structures, 14-layered elliptical structures were printed. The structures' widths were measured following deposition of each layer. The heights of the structures were measured for only a subset of layers, since each height measurement required removal of the gel from the printing

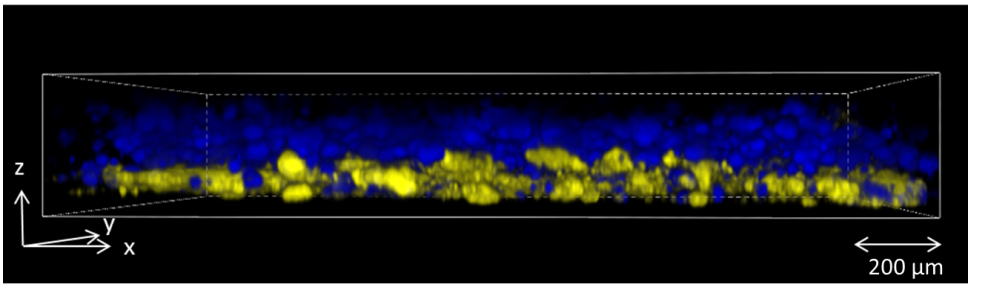


Figure 5.4: Internal structure of printed layers. Modified strains of *E. coli* expressing two different fluorescent proteins were printed one on top of the other in a 2-layered square. After 24 h of incubation, the internal structure of the printed bacterial layers was inspected by confocal microscopy. The bottom layer contained 81% ± 5% blue fluorescent cells, while the top layer contained 93% ± 5% yellow cells.



surface, halting the printing process. The average line width increased significantly but incrementally for the first six layers, with an average increase of 0.14 ± 0.01 mm/layer between layers 1 and 6 (Figure 5.3b). Following the sixth layer, the line widths approached a plateau; no significant differences were observed between the line widths of any of the layers between layers 6 and 14 (ANOVA + Tukey *post hoc* test, p-value: 0.995). The height of the printed material was observed to increase continually, by an average of 0.16 ± 0.02 mm/layer. The final 14-layered structures were 2.14 ± 0.11 mm in height, with a width of 2.32 ± 0.37 mm. These measurements indicate that our printing system is capable of fabricating 3-dimensional structures at submillimeter-scale precision in all dimensions. Further improvements in resolution may be possible by rebuilding our system using a commercial 3D printer employing more accurate printhead positioning [15].

Since some applications may require the printing of multi-layered structures containing spatially separated bacterial strains, the internal structure of multi-layered printed bacteria was analyzed. Bi-layered structures were printed containing engineered *Escherichia coli*, in which the bacteria in bottom layer of bioink expressed the yellow fluorescent protein mVenus, and the bacteria in the top layer expressed the blue fluorescent protein mCerulean. Each layer was printed using separate tubing and pipette tips to prevent contamination of the top layer by bacteria printed in the previous layer. After 24 h of incubation, the structure was imaged at different depths using confocal microscopy, and the extent of bacterial mixing between the layers was quantified through image analysis. The bottom layer was 81% ± 5% homogeneous, while the top layer was 93% ± 5% homogeneous (Figure 5.4). This analysis indicates good separation of bacteria between adjacent printed layers, even after extensive periods of incubation. The lower layer may have been less pure due to incomplete solidification before printing of the top layer, which could be improved via an increased waiting time between printing of layers.

### 5.2.3. SURVIVAL AND METABOLIC ACTIVITY OF PRINTED BACTERIA

In order for our alginate-based printing system to be successfully applied to microbial materials production, bacteria must be able to survive well within the alginate gel. To test this property, *E. coli* was incorporated into alginate hydrogels, and gels were incu-

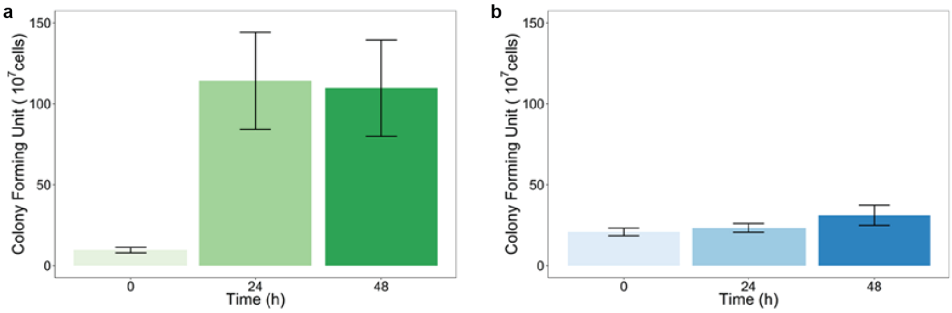


Figure 5.5: Robust bacterial survival within printed alginate gels and planktonic bioink. The number of colony forming units is shown for *E. coli* printed within alginate gels (a) or as a planktonic sample (b), incubated for varying amounts of time ($n = 6$). Error bars indicate the standard error.

bated for varying amounts of time from 0–48 h at 37 °C. The gels were then added to a solution of sodium citrate to chelate the calcium ions and dissolve the gel. The samples were grown on LB-agar plates to determine the number of viable cells (colony forming units). An increase in colony forming units observed between the first two data points may indicate that bacterial growth occurs within the alginate gel during the first 24 h after gel production (Figure 5.5a). Thereafter, colony forming units remained fairly constant for up to 48 h. Comparison with bacteria that were incubated in non-printed, liquid bioink indicated that the printing process initially reduces the viability of *E. coli* by approximately 50% (Figure 5.5b). Thereafter, the levels of viable bacteria in the non-printed bioink remained nearly constant, likely due to nutrient limitation. The dramatic increase in the number of viable bacteria in the printed gel resulted in an overall increase in viability of approximately 200% in comparison to the nonprinted bioink, which may be due to the additional nutrients in the agar printing substrate and the lower bacterial density after printing. Bacteria can thus remain viable within the alginate gel of our bioink for at least 2 days following gel formation, providing sufficient time for microbial-mediated materials production or patterning to occur.

Both survival and metabolic activity of the printed bacteria are key factors to demonstrate the applicability of our printing system. To assess the ability of our printed bacteria to create a product, *E. coli* containing the rhamnose-inducible red fluorescent protein RFP were printed onto an agar plate containing the rhamnose inducer. The gel was incubated, and the color of the gel was monitored over 48 h. After 8 h of incubation, the induced bioink showed a noticeable red color, which became very intense after 48 h (Figure 5.6). This experiment demonstrates that our printed bioink is able to support the production of bacterially made materials over short periods of time. Our printing system could be readily applied to the patterned production of bacterially created materials in a variety of different formats. Bioink containing both active bacteria and material precursors could be printed onto a neutral surface, to create a three-dimensionally patterned hydrogel within which the bacteria chemically convert the precursors to the desired final product. The thorough commingling of bacteria and chemical substrates within the gel in this configuration would lead to high efficiency of material production. Alternately, alginate gel containing only the chemical precursor could be printed and then immersed

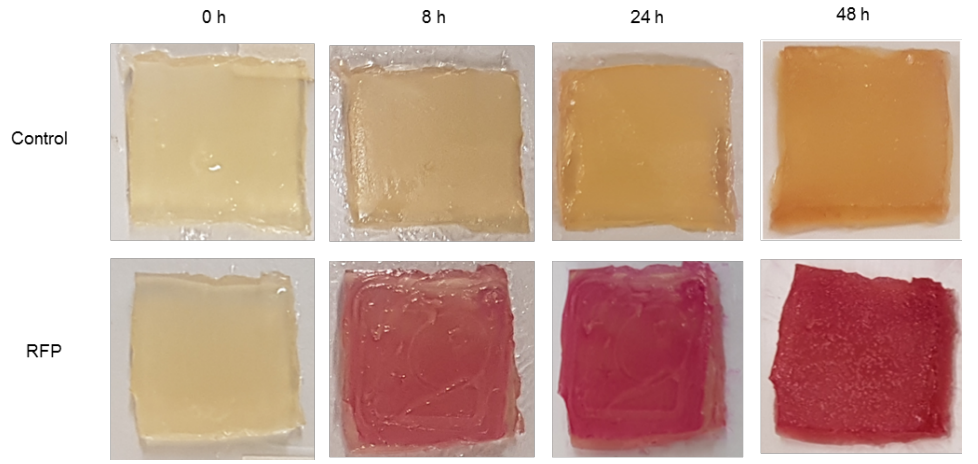


Figure 5.6: Metabolic activity within printed alginate gels. *E. coli* with and without a rhamnose-inducible RFP plasmid were printed onto a substrate containing rhamnose. Printed gels were incubated at 37 °C, and color changes were observed over time.



within a liquid bacterial culture to create a final 3D-patterned material that is largely bacteria-free. In a third scenario, bacteria-containing bioink could be printed onto a surface that is coated with material precursors, which the bacteria could then convert into a two-dimensionally patterned final product. This approach has the appealing feature that the alginate gel could be dissolved away after the fact, leaving behind only the final material.

## 5.3. CONCLUSION

The work shown here demonstrates the development of macroscopic material printing with millimeter-scale resolution using removable hydrogels and bacterial chemistry. This approach enables us also to print precursor or supportive material directly with the bacteria. Our printing technique is inexpensive, straightforward, and can produce bacterial structures of a wide variety of three-dimensional shapes without requiring printing scaffolds, excepting structures that contain internal bridges or enclosed hollow spaces. Furthermore, bacteria in printed gels remain accessible to the experimenter e.g. through the use of chemical inducers. Our technology is well-suited for the use of wild-type organisms or synthetically modified bacteria, which could be designed to carry out new combinations of microbial reactions to create a great number of different types of materials, such as new nacre-inspired composites. Connecting our novel and straightforward bacteria printing techniques with approaches of synthetic biology will further improve its value as a “green” material production process and patterning methodology. The ease and simplicity of our printing approach will allow any interested research group to adapt and improve this process at low cost for multiple possible applications.

## 5.4. METHODS

### 5.4.1. PRINTING SYSTEM

The extruder and heater of a standard 3D printer (CoLiDo DIY) were removed and replaced by a pipette tip, a tubing system, and a syringe pump. Silicon tubing (VWR DENE 3100103/25) with an inner diameter of 1 mm and an outer diameter of 3 mm was used to connect a 200 µL pipette tip to a 10 mL syringe. The syringe was loaded with 10 mL of bioink and mounted in a syringe pump (ProSense B.V. NE-300). A secondary 200 µL pipette tip was affixed to the printhead and connected to silicon tubing to allow for rapid exchange of the pipette tip to deposit a second type of material. Printed objects were drawn in the free online CAD program Tinkercad, sliced via the RepRap Slic3r software, and manually adapted and implemented for printing using CoLiDo software.

### 5.4.2. BACTERIAL STRAINS, PLASMIDS, AND CULTURE

*Escherichia coli* K12 MG1655 was transformed with an SB101 plasmid containing RFP under the control of a rhamnose-inducible promoter. *Escherichia coli* Top10 cells were transformed with plasmids AM420 or AM421. Cells were cultured overnight in LB media supplemented with the appropriate antibiotic (25 $\mu g\,mL^{-1}$ ampicillin or kanamycin) at 37 °C with continuous shaking at 250 rpm.

Plasmid AM420 is a p15A-derived plasmid carrying an ampicillin resistance gene, a constitutively expressed *lacI* gene, and the gene for the blue fluorescent protein Cerulean (gene sequence originally from pZS2–123 [29], Addgene plasmid # 26598) behind an IPTG-inducible promoter.

Plasmid AM421 is a pSC101-derived plasmid carrying a kanamycin resistance gene, a constitutively expressed *tetR* gene, and the gene for the yellow fluorescent protein mVenus (gene sequence originally from mVenus N1 [30], Addgene plasmid # 27793) behind an anhydrotetracycline-inducible promoter.

### 5.4.3. PRINTER BIOINK

To obtain 10 mL of bioink containing *E. coli*, 10 mL of overnight bacterial culture ($OD_{600}$ of approximately 2.5) were spun down at 400 rpm for 3 min and the supernatant discarded. The cells were resuspended in 5 mL of sterile LB medium (Sigma-Aldrich). A 5 mL mixture of sodium alginate (5% w/v, Sigma-Aldrich) was added to the solution, followed by vortexing.

### 5.4.4. PRINTING SUBSTRATE

A Petri dish (150 mm × 15 mm) was filled with 20 mL of agar (1.5% w/v) dissolved in LB medium. The printing surface was prepared by the equally distributed application of 500 µL 1 M $CaCl_2$ onto the agar surface.

### 5.4.5. RESOLUTION AND HEIGHT MEASUREMENTS

Printing resolution was determined by measuring the width and height of printed samples with a digital caliper (GEDORE No. 711) three times per position for each layer. Prior to the start of printing, the Petri dish lid containing the agar printing surface was affixed to the printer platform using double-faced adhesive tape to prevent changes in the po-

sition of the substrate during measurements. Width measurements were recorded for successive layers printed onto the same base layer. Measurement positions within printed ellipses were selected prior to printing: two random points within curved end regions, two random points in straight-edged side regions, and two random points in the transitional area between curved and straight regions. To determine the height of printed samples, the printed structure was removed from the agar printing surface, therefore additional printed layers could not be added post measurement.

### 5.4.6. PRINTING AND IMAGING OF LAYERED ALGINATE GELS CONTAINING FLUORESCENT BACTERIA

Printing substrate including inducers (1 mM IPTG to induce mCerulean expression, 50 ng mL$^{-1}$ anhydrotetracycline to induce mVenus expression) was prepared in a Petri dish. A sheet of dialysis membrane (Spectra/Por 2 Dialysis Tubing, 12–14 kDa MWCO, Spectrum Europe B.V., The Netherlands) was placed on the agar prior to printing, to ensure diffusion of nutrients and inducers from the agar substrate to the printed gel while facilitating the eventual transfer of the gel onto a microscope slide. A single rectangular layer of bioink was printed containing *E. coli* with AM421, then a second rectangular layer of bioink containing *E. coli* with AM420 was printed on top of the first layer, using separate tubing and pipet tips to avoid bacterial cross-contamination.

After 24 h of incubation at 37 °C, the printed gels and underlying dialysis membranes were sliced with a scalpel. Samples were transferred onto a microscope slide and imaged with a Nikon A1+ fluorescence confocal microscope (magnification 200×, excitation wavelengths 457 or 514 nm, detected wavelengths 482/540 nm for Cerulean and mVenus, respectively).

### 5.4.7. BACTERIAL SURVIVAL

To determine bacterial survival, 5 mL of an overnight culture of *E. coli* K12 MG1655 ($OD_{600}$ of approximately 2.5) was spun down at 4000 rpm for 3 min and the supernatant discarded. The bacterial pellet was resuspended in 5 mL of fresh LB medium containing 2% w/v sodium alginate by vortexing until all ingredients were entirely dissolved. A portion of the bioink was used to print a 6-layered rectangular quadrangle. The gel was allowed to solidify for 30 min before the first sample was taken. The remainder of the bioink was incubated in un-solidified liquid form at 37 °C as a positive control showing planktonic growth. After 0, 24, or 48 h of incubation at 37 °C, 0.3 g of the gel was removed and dissolved in 1.75 mL of 1 M sodium citrate solution. For planktonic samples, 200 µL samples were removed, containing approximately the same volume of bioink as that sampled from the printed gel. Colony forming units (CFU) were determined following the protocol of Karas *et al.* [31]. In short, each sample was serially diluted three times (in 10-fold increments from $10^{-1}$ to $10^{-8}$), and 5 µL of each dilution was pipetted in triplicate onto a LB-agar plate. The plates were incubated at 37 °C for 24 h, and visible colonies were counted.

### 5.4.8. PRODUCTION OF RFP BY PRINTED BACTERIA

Two 6-layered, square-shaped gels were printed on an LB-agar plate containing 0.2% rhamnose. One gel contained *E. coli* with a rhamnose-inducible RFP-producing plas-

mid, and the other one contained wild-type *E. coli* K12 MG1655. The agar around the printed gel was removed to increase its visibility. The printed gels were photographed under constant light conditions over a 48 h period.

### 5.4.9. STATISTICAL METHODS

R-Studio was used to perform the statistical analyses. All data sets were assumed to be normally distributed and were checked for outliers with a Dixon's Q-Test. Unless noted, no outliers were removed from the data sets. One-way ANOVA was used to compare multiple data sets, and two-sample Student's t test was used for comparing two data sets. In cases where the ANOVA test showed a significant difference, a Tukey's *post hoc* test was used to obtain an overview of all significant differences occurring within the data set.

### 5.4.10. ACKNOWLEDGEMENTS

Our thanks to Roland Kieffer for helping us to develop the 3D printer and to Stan Brouns and Rebecca McKenzie for donating the RFP-producing *E. coli* strain. The plasmids AM420 and AM421 were constructed and graciously provided by Ferhat Büke.



## REFERENCES

[1] B. A. E. Lehner, D. T. Schmieden, and A. S. Meyer, *A straightforward approach for 3d bacterial printing,* ACS Synthetic Biology **6**, 1124 (2017).

[2] T. Hiraishi, *Poly(aspartic acid) (paa) hydrolases and paa biodegradation: current knowledge and impact on applications,* European journal of applied microbiology and biotechnology **100**, 1623 (2016).

[3] B. C. Stanton, A. A. K. Nielsen, A. Tamsir, K. Clancy, T. Peterson, and C. A. Voigt, *Genomic mining of prokaryotic repressors for orthogonal logic gates,* Nature Chemical Biology **10**, 99 (2013).

[4] J. Bonnet, P. Yin, M. E. Ortiz, P. Subsoontorn, and D. Endy, *Amplifying genetic logic gates,* Science **340**, 599 (2013).

[5] A. Prindle, J. Selimkhanov, H. Li, I. Razinkov, L. S. Tsimring, and J. Hasty, *Rapid and tunable post-translational coupling of genetic circuits,* Nature **508**, 387 (2014).

[6] R. Verlinden, D. J. Hill, M. A. Kenward, C. D. Williams, and I. Radecka, *Bacterial synthesis of biodegradable polyhydroxyalkanoates,* Journal of Applied Bacteriology **102**, 1437 (2007).

[7] I. Sulaeva, U. Henniges, T. Rosenau, and A. Potthast, *Bacterial cellulose as a material for wound treatment: Properties and modifications. a review,* Biotechnology Advances **33**, 1547 (2015).

[8] C. Zhong, T. Gurry, A. A. Cheng, J. Downey, Z. Deng, C. M. Stultz, and T. K. Lu, *Strong underwater adhesives made by self-assembling multi-protein nanofibres,* Nature Nanotechnology **9**, 858 (2014).

[9] A. Y. Chen, Z. Deng, A. N. Billings, Seker, Urartu O. S., M. Y. Lu, R. J. Citorik, B. Zakeri, and T. K. Lu, *Synthesis and patterning of tunable multiscale materials with engineered cells,* Nature Materials **13**, 515 (2014).

[10] P. Höfer, P. Vermette, and D. Groleau, *Introducing a new bioengineered bug: Methylobacterium extorquens tuned as a microbial bioplastic factory,* Bioengineered Bugs **2**, 71 (2011).

[11] Guanyun Wang, Lining Yao, Wen Wang, Jifei Ou, Chin-Yi Cheng, and Hiroshi Ishii, *xprint: A modularized liquid printer for smart materials deposition,* in *Proceedings of the 2016 CHI Conference on Human Factors in Computing Systems* (ACM, San Jose, California, USA, 2016) pp. 5743–5752.

[12] E. Matias and B. Rao, eds., *3D printing: On its historical evolution and the implications for business: 2015 Portland International Conference on Management of Engineering and Technology (PICMET)* (2015).

[13] K. V. Wong and A. Hernandez, *A review of additive manufacturing,* ISRN Mechanical Engineering **2012**, 1 (2012).

[14] K. G. Cooper, *Rapid prototyping technology: Selection and application / Kenneth G. Cooper*, Mechanical engineering, Vol. 133 (M. Dekker, New York, 2001).

[15] S. V. Murphy and A. Atala, *3d bioprinting of tissues and organs,* Nature Biotechnology **32**, 773 (2014).

[16] F. Pati, D.-H. Ha, J. Jang, H. H. Han, J.-W. Rhie, and D.-W. Cho, *Biomimetic 3d tissue printing for soft tissue regeneration,* Biomaterials **62**, 164 (2015).

[17] F. Pati, J. Jang, D.-H. Ha, S. Won Kim, J.-W. Rhie, J.-H. Shim, D.-H. Kim, and D.-W. Cho, *Printing three-dimensional tissue analogues with decellularized extracellular matrix bioink,* Nature communications **5**, 3935 (2014).

[18] D. Sher, *The top 15 bioprinters,* (2015).

[19] X. Cui, T. Boland, D. D.D'Lima, and M. K. Lotz, *Thermal inkjet printing in tissue engineering and regenerative medicine,* Recent Patents on Drug Delivery & Formulation **6**, 149 (2012).

[20] C. M. Smith, A. L. Stone, R. L. Parkhill, R. L. Stewart, M. W. Simpkins, A. M. Kachurin, W. L. Warren, and S. K. Williams, *Three-dimensional bioassembly tool for generating viable tissue-engineered constructs,* Tissue engineering **10**, 1566 (2004).

[21] Armstrong, James P. K., M. Burke, B. M. Carter, S. A. Davis, and A. W. Perriman, *3d bioprinting using a templated porous bioink,* Advanced Healthcare Materials **5**, 1724 (2016).

[22] V. Mironov, R. P. Visconti, V. Kasyanov, G. Forgacs, C. J. Drake, and R. R. Markwald, *Organ printing: tissue spheroids as building blocks,* Biomaterials **30**, 2164 (2009).

[23] Dosier, Ginger, and Krieg, *Methods for making construction material using enzyme producing bacteria,* (2011).

[24] J. L. Connell, E. T. Ritschdorff, M. Whiteley, and J. B. Shear, *3d printing of microscopic bacterial communities,* Proceedings of the National Academy of Sciences **110**, 18380 (2013).

[25] C. K. Kuo and P. X. Ma, *Ionically crosslinked alginate hydrogels as scaffolds for tissue engineering: Part 1. structure, gelation rate and mechanical properties,* Biomaterials **22**, 511 (2001).

[26] K. F. Almqvist, *Culture of chondrocytes in alginate surrounded by fibrin gel: characteristics of the cells over a period of eight weeks,* Annals of the Rheumatic Diseases **60**, 781 (2001).

[27] S. Kim, Y. Yoo, H. Kim, E. Lee, and J. Y. Lee, *Reduction of graphene oxide/alginate composite hydrogels for enhanced adsorption of hydrophobic compounds,* Nanotechnology **26**, 405602 (2015).

[28] D. Hernandez, *Factors affecting dimensional precision of consumer 3d printing,* International Journal of Aviation, Aeronautics, and Aerospace (2015), 10.15394/ijaaa.2015.1085.

[29] R. S. Cox, M. J. Dunlop, and M. B. Elowitz, *A synthetic three-color scaffold for monitoring genetic regulation and noise,* Journal of Biological Engineering **4**, 10 (2010).

[30] S. V. Koushik, H. Chen, C. Thaler, Puhl III, Henry L., and S. S. Vogel, *Cerulean, venus, and venusy67c fret reference standards,* Biophysical Journal **91**, L99 (2006).

[31] V. O. Karas, I. Westerlaken, and A. S. Meyer, *The dna-binding protein from starved cells (dps) utilizes dual functions to defend cells against multiple stresses,* Journal of bacteriology **197**, 3206 (2015).

# 6

# PRINTING OF PATTERNED, ENGINEERED *E. coli* BIOFILMS WITH A LOW-COST 3D PRINTER

**Dominik T. SCHMIEDEN, Samantha J.BASALO VÁZQUEZ, Héctor SANGÜESA, Marit VAN DER DOES, Timon IDEMA, Anne S. MEYER**

Biofilms can grow on virtually any surface available, with impacts ranging from endangering the lives of patients to degrading unwanted water contaminants. Biofilm research is challenging due to the high degree of biofilm heterogeneity. A method for the production of standardized, reproducible, and patterned biofilm-inspired materials could be a boon for biofilm research and allow for completely new engineering applications. Here, we present such a method, combining 3D printing with genetic engineering. We prototyped a low-cost 3D printer that prints bioink, a suspension of bacteria in a solution of alginate that solidifies on a calcium-containing substrate. We 3D-printed *Escherichia coli* in different shapes and in discrete layers, after which the cells survived in the printing matrix for at least one week. When printed bacteria were induced to form curli fibers, the major proteinaceous extracellular component of *E. coli* biofilms, they remained adherent to the printing substrate and stably spatially patterned even after treatment with a matrix-dissolving agent, indicating that a biofilm-mimicking structure had formed. This work is the first demonstration of patterned, biofilm-inspired living materials that are produced by genetic control over curli formation in combination with spatial control by 3D printing. These materials could be used as living, functional materials in applications

Parts of this chapter have been published in ACS Synthetic Biology 7.5 (2018): 1328–1337 [1].

such as production of nacre-inspired materials, water filtration, metal ion sequestration, or civil engineering, and potentially as standardizable models for certain curli-containing biofilms.

## 6.1. INTRODUCTION

Biofilms are aggregates of microbial cells surrounded by a self-produced matrix [2]. The formation of a biofilm allows pathogenic bacteria to resist medical treatment [3] or to colonize surfaces such as catheters or implants [4–6], posing a serious risk to patients. Biofilm research thus frequently focuses on combatting nefarious biofilms [7, 8], control of biofilm formation[9], patterning of model biofilms [10, 11], and biofilm-induced corrosion [12]. Conversely, biofilms are used for beneficial applications such as wastewater treatment [13], bioleaching [14, 15], or as living materials for potential applications like bioremediation [16]. Biofilms are highly heterogeneous, leading to uneven distributions of e.g. biomass, nutrients, or metabolic products [13], which in turn leads to physiological heterogeneity of the constituent cells. Genetically variant sub-populations and persister cells have been identified that allow biofilms to re-grow after treatments that largely destroy the biofilm, for example by the immune system or disinfectants [17]. Even genes closely involved in biofilm formation are not necessarily expressed in all cells of the biofilm. DePas *et al.* [18] observed two populations of cells in rugose (wrinkled) biofilms of uropathogenic *E. coli* UTI89: one population expressing an extracellular matrix of amyloid fibers and cellulose at the biofilm surface, while the second population in the inner regions of the biofilm did not express extracellular matrix components. In order for biofilm-inspired living materials to be useful tools for engineering and research, a tight control over the spatial arrangement of the cells, as well as formation of extracellular matrix components, will be required. In this chapter, we demonstrate a method that combines 3D printing with genetic control over biofilm formation as a first step in this direction.



While 3D printers are widely used in tissue engineering to arrange eukaryotic cells in arbitrary shapes [19, 20], the first bacterial 3D printers for macroscale structures have only recently been developed. Lehner *et al.* [21] suspended bacteria in a solution of alginate, a polymer that forms a gel upon complexation of calcium ions. When this solution was printed onto calcium-containing agar plates with a 3D printer adapted for bacterial cells, multilayered bacteria gels in various shapes could be produced with sub-millimeter precision. Diffusion of nutrients from the substrate allowed the cells to survive for at least two days, and controllable expression of a gene was achieved with a chemical inducer (Chapter 5). Thereafter, Schaffner *et al.* [16] created 3D-printed gels containing *Pseudomonas putida* to generate a living material for the degradation of phenol. *Acetobacter xylinum* was also printed to produce bacterial cellulose on a three-dimensional surface, demonstrating a new strategy of materials production with the potential to be used in personalized medicine. However, while these methods excel at arranging cells in a 3D polymeric matrix, the development of a biofilm by the bacteria is uncontrolled, and the stability of the printed bacteria is limited by the chemistry of the matrix polymers [22].

Here, we solve these problems by printing engineered *E. coli* cells that form biofilms in the presence of an inducer. In nature, the switch from planktonic to biofilm growth occurs when *E. coli* faces stress conditions, such as nutrient or salt limitation, or low temperatures [23]. Amyloid fibers called curli [24] form the major proteinaceous component of the extracellular matrix, which can also include cellulose and other polysaccharides, depending on strain and growth conditions [23]. Curli fibers consist of the secreted pro-

tein CsgA, which self-assembles [25] on the membrane nucleator protein CsgB [26] to form fibers that interconnect biofilm cells and adhere to surfaces. Curli gene expression is complex, involving proteins encoded in two operons: *csgBAC* and *csgDEFG* [27]. CsgD acts as a positive regulator of curli formation and other biofilm components, while CsgE, F, and G are involved in the export and folding of CsgA and CsgB [28].

In this chapter, we demonstrate a novel method for 3D printing patterned biofilm-inspired materials of engineered *E. coli* cells. When engineered cells were induced to express the CsgA protein after printing, they formed artificial biofilms that protected the cells from being washed away with a gel-dissolving agent. Furthermore, we prototyped a cost-effective 3D printer for bacteria made from K'NEX parts that is capable of printing our engineered bacteria in stable, layered 3D structures. The combination of biofilm-forming bacteria with 3D printing could lead to the development of reproducible, standardized biofilms for research and testing to complement existing in vitro methods [29]. 3D printing could also allow for the precise patterning of mixed cultures in a hydrogel environment, for example, to study interactions between pathogens and eukaryotic cells. Furthermore, when combined with genetic or protein engineering, this technique could be used to print completely new, living materials for bio-engineering applications in biotechnology, medicine, or civil engineering.



## 6.2. RESULTS AND DISCUSSION

### 6.2.1. THE BIOLINKER, A COST-EFFECTIVE 3D PRINTER FOR BACTERIA

In order for engineered biofilms to serve as living materials for engineering applications, precise control over biofilm spatial patterning is needed, which can be achieved by 3D printing. 3D printers built or refitted for high-resolution cell printing have previously been developed successfully [19, 21, 30, 31]. Here, we aimed at building a 3D printer ("The Biolinker") that could serve both as a scientific instrument and as an educational tool, while being cost-effective and consisting of easily obtainable parts. Modular toy construction systems such as Lego or K'NEX are inexpensive and known to many students from their own childhood, and their component pieces are frequently already available to educators, potentially further lowering the price. We developed the Biolinker using K'NEX parts, since K'NEX offers many combinable pieces for building structures with moving parts, such as beams, connectors, gears, chains, and DC motors.

We assembled K'NEX parts to build a frame containing a printhead located overtop of a 2D-stage, which can hold printing substrates. The K'NEX structure was combined with standard electronic components allowing for the controllable motion of the printing stage (Figure 6.1a). While commercial 3D printers typically use stepper motors to actuate the stage, we employed K'NEX DC motors for the ease of interfacing the motors with the K'NEX frame. The chains connecting the stage to the motors must be installed under sub-maximal tension to prevent breaking the connections between the K'NEX parts of the stage frame, which leads to a delay of about 1 s between switching on the motor and the start of the stage movement (Figure 6.2). This delay can be compensated for by delaying the start of the pump that extrudes the bacteria. The speed and direction of rotation of the stage motors and the pump are controlled in an automated, coordinated manner by two Arduino boards, and commands are sent by an external computer

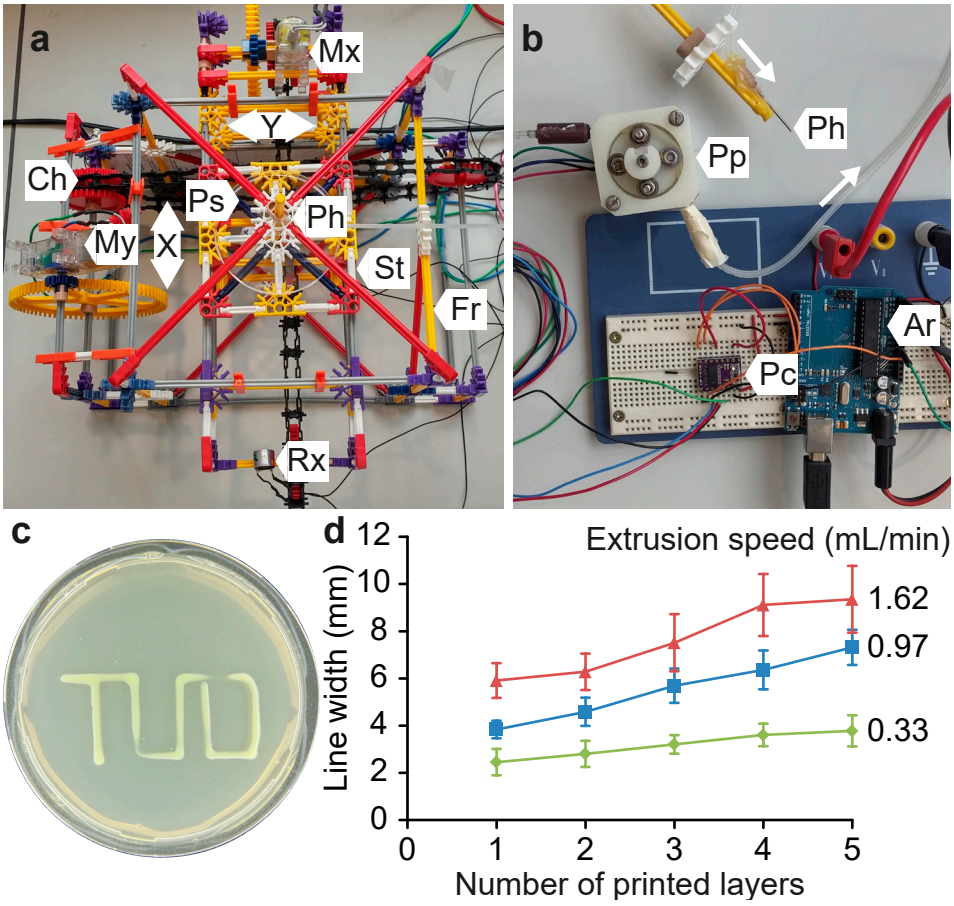


Figure 6.1: The Biolinker: a 3D printer for bacteria built with K'NEX and electronic parts. (a) Printing stage with frame seen from above, Mx: motor x-axis, My: motor y-axis, Ch: chain, Ps: printing substrate, Ph: printhead, St: printing stage, Fr: frame, Rx: receiver of x-axis ultrasound sensor. Double-headed arrows indicate axis orientation. (b) Printer pump and print head, Pp: peristaltic pump, Ph: printhead (detached), Pc: pump controller, Ar: Arduino board. Arrows indicate flow direction. (c) Bioink containing green-fluorescing bacteria printed with the Biolinker onto an LB-agar plate. (d) Lines containing up to five layers of alginate gel were printed onto agar plates with three different extrusion speeds. Error bars represent the standard deviation.

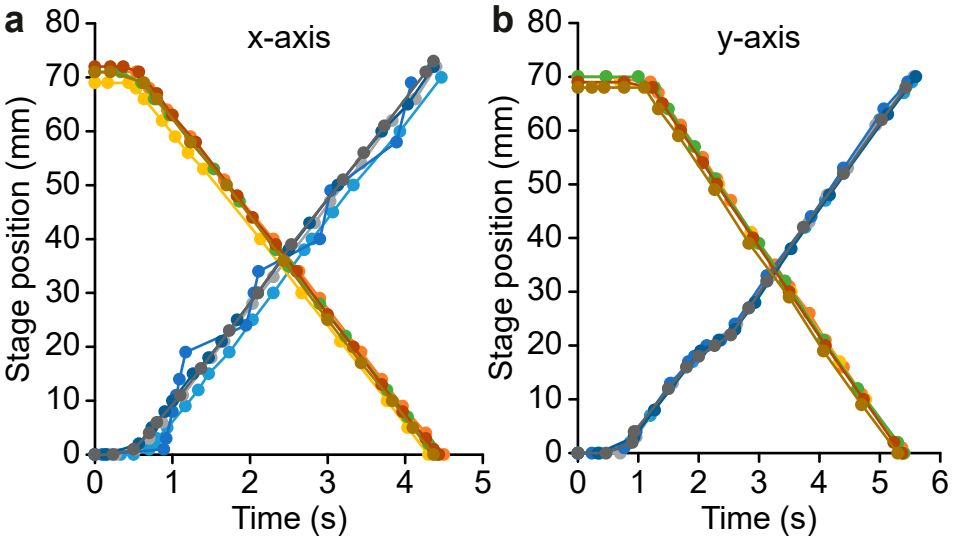


Figure 6.2: Biolinker stage movement along the x- and y-axis. The stage was filmed during movement in both directions in the (a) x-orientation and (b) y-orientation, traversing the entire possible length of movement. A ruler attached to the Biolinker frame was used to track the stage position. An LED light bulb attached to the Biolinker frame was switched on/off at the same time that the command to start/stop the stage movement was sent, to indicate the precise timing of the start- and stop-commands relative to the stage position. Stage position over 20 separate trajectories is represented here.



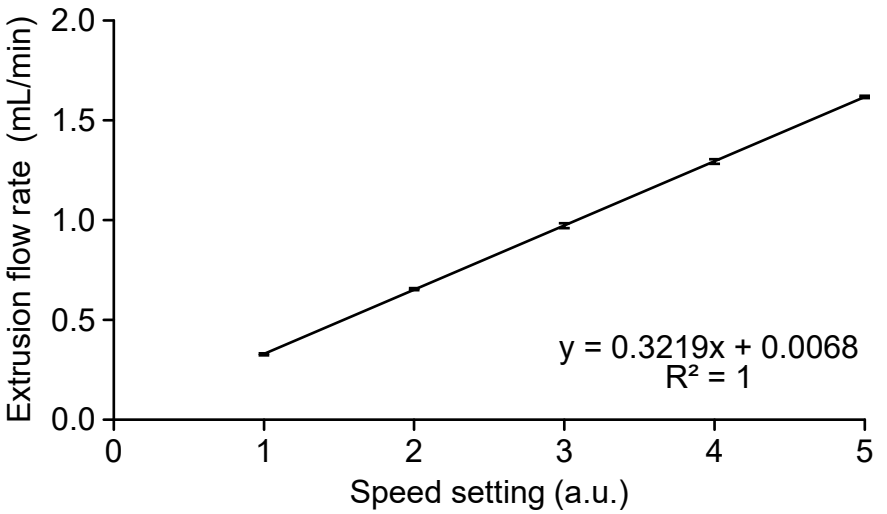


Figure 6.3: Extrusion flow rate of the Biolinker pump at each speed setting. Water was pumped for 10 min at pump speed settings ranging from 1 to 5 and weighed. Errors represent the standard deviation, $n = 3$.

running our self-written control software. For improved spatial precision of bacterial deposition, ultrasound sensors report to the control software on the stage position in both the x- and y-directions.

In order to 3D print with bacteria, we need an extrusion mechanism that is non-lethal to cells. In accordance with our aim of affordability, we constructed a DIY peristaltic pump by using publicly available design specifications. This peristaltic pump moves liquids through the printhead (Figure 6.1b) with precise control over the extrusion flow rate (Figure 6.3). However, without a shape-preserving agent that transforms the extruded liquid into a gel, the printed shapes would quickly lose resolution upon spreading of the liquid on the substrate surface. The Biolinker pump thus extrudes "bioink," which is a mixture of bacteria, liquid growth medium, and alginate. Agar plates serve as printing substrates. Prior to printing, a calcium chloride solution is spread onto the plates. Upon printing of the bioink onto the calcium-impregnated printing surface, the alginate molecules of the bioink complex with the calcium ions, polymerizing the bioink into a solid hydrogel that holds the bacteria in place [21].

The Biolinker allows for the printing of simple bioink shapes in 2D (outlines or filled), e.g. rectangles, triangles, or even letters such as "T" or "U" (Figure 6.1c). Printed 2D shapes can be extended into layered 3D shapes after manually raising the syringe tip of the printhead. Different line widths can be produced by changing the pumping speed, allowing a minimum line width of approximately 2 mm (Figure 6.1d). While the pump can run arbitrarily slowly, a minimum flow rate of approximately 0.33 mL min$^{-1}$ was required to produce continuous printing. The width of a multilayered line increased fractionally with each layer added, by an average of approximately 14% (Figure 6.1d). This increase in width is likely caused by a decrease in calcium ion concentration with higher distance from the printing substrate, allowing the printed bioink to spread out for a longer period of time before gelation occurs. Along the length of printed lines, the width can vary due to different distances between the syringe tip and the agar surface since it is difficult to produce agar plates with completely level surfaces (see thinner sections in Figure 6.1c).

The Biolinker combines classical engineering, electronics, and biology in a cost-effective DIY manner, making it an interdisciplinary educational tool. Toy kits such as K'NEX or Lego have already been used successfully at the school- and university-level to enable the hands-on teaching of natural science subjects or architecture [32, 33]. Excluding the external computer, the components of the Biolinker cost about €350 (of which €220 for non-K'NEX parts), making it, to our knowledge, the cheapest 3D printer for cells to date. All printer experiments in this work were performed with the Biolinker, but for applications requiring higher precision, the K'NEX components could easily be replaced with a commercial, albeit more expensive, DIY 3D printing kit (Chapter 5).

### 6.2.2. BACTERIA CAN SURVIVE FOR EXTENDED PERIODS OF TIME IN ALGINATE GELS

In order to produce printed biofilms, the deposited bacteria have to survive in the alginate gels for extended periods of time to allow for biofilm formation. Furthermore, depending on the application, the generation of bacterial products should be sustainable over a longer duration and controllable with chemical inducers added to the printing

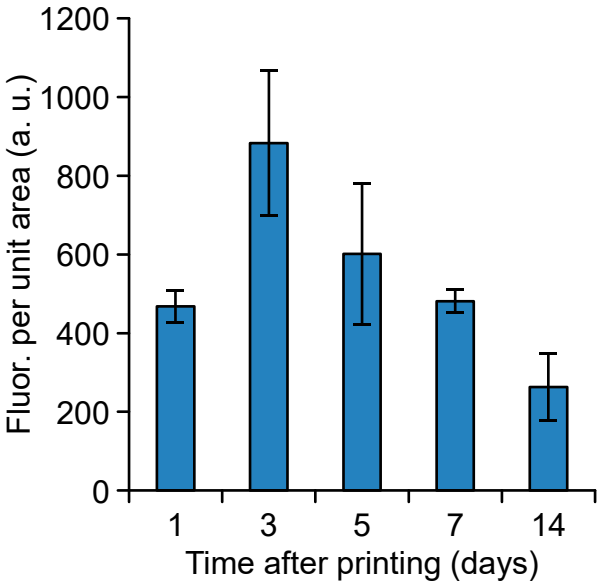


Figure 6.4: Bacterial fluorescence in bioink gels is detectable for roughly two weeks. A layer of bioink containing *E. coli* carrying a plasmid for inducible Cerulean expression was printed onto an LB-agar plate containing chemical inducer and allowed to solidify. Plates were incubated for two weeks at 37 °C. Samples were taken at different time points and imaged using confocal microscopy to measure fluorescence per unit area along the z-axis. Error bars represent the standard deviation. $n \geq 3$



substrate. When printing multiple stacked layers of bioink on a calcium-containing substrate, we saw gelation of the ink within seconds for the first layer and up to 5 min for the fifth layer, showing that calcium ions can diffuse freely from the substrate to the upper layers. To investigate whether printed bacteria can also be furnished effectively with nutrients and inducers diffusing from the printing substrate, we printed bacteria expressing an inducible blue fluorescent protein onto LB-agar plates. The agar contained the appropriate inducer for production of the fluorescent protein, while the bioink contained none. We monitored the fluorescence of the bacteria-containing gel over a timespan of two weeks using confocal microscopy, revealing robust fluorescence during the first week after the printing (Figure 6.4). This result demonstrates that gene expression in printed bacteria can be controlled by inducers present in the substrate.

To gauge the effect of gel encapsulation on bacterial survival, we determined the number of colony forming units (CFU) in printed bioink over a time span of 12 days by dissolving samples with citrate solution and incubating on LB-agar plates (Figure 6.5). In order to compare the viability in gel cultures to liquid cultures, we also printed bioink onto LB-agar plates that did not contain calcium, so that gelation was not triggered. Prior to CFU determination, these liquid cultures were treated with either citrate or PBS, allowing for observation of the influence of the citrate treatment on viability. The number of colony forming units in gels remained stable within approximately one order of magnitude for 7–8 days after printing before declining sharply. Liquid cultures showed the highest number of colony forming units one day after the print, after which the number

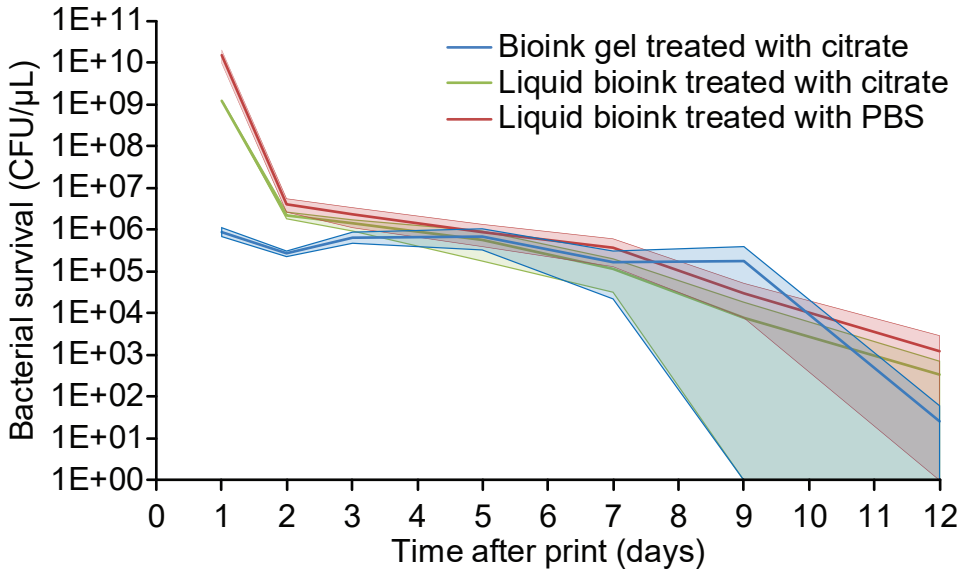


Figure 6.5: Bacteria in bioink gels remain viable for 7–9 days. Bioink containing *E. coli* AM401 (constitutive GFP) was printed onto LB-agar plates either supplemented with $CaCl_2$, to create solidified bioink gel (blue line), or without $CaCl_2$, to keep the bioink in liquid form on the agar surface (red and green lines). Bioink samples were incubated at 37 °C for 12 days, during which samples were taken and colony forming units determined. Prior to CFU determination, gel samples were dissolved by treatment with sodium citrate solution, and liquid samples were either treated with citrate (green line) or PBS (red line). Shaded areas represent the standard deviations, shown with a lower boundary of 1. $n = 3$.



of CFUs declined to approximately the level of the gel samples. The viability of these liquid cultures remained stable at a level comparable to the gel cultures for the following 6 days before dying off. Citrate-treated cultures consistently showed fewer CFUs than non-treated ones, suggesting a mildly toxic effect from the 10-minute citrate treatment.

From the fluorescence and viability experiments, we conclude that, in this setup, printed bacteria are useful for experimentation and applications for roughly one week after printing. The main limiting factors of bacterial survival are likely nutrient depletion, accumulation of waste products, and drying of the gels and plates. Drying can be delayed by sealing the plates with plastic wrap and supplementation of water. If bacteria would have to be kept alive in bioink gels for a longer time, fresh nutrients could be supplied and waste products could be removed by submerging the printed gels in growth medium, supplied with calcium chloride to avoid gel dissolution [22].

### 6.2.3. BACTERIA CAN BE 3D-PRINTED IN DISCRETE LAYERS

Depending on the application, printed 3D structures should retain their layering, and only minimal mixing of bacteria should occur between the layers. In order to observe the mixing behavior of structures printed with the Biolinker, we printed a layer of bioink containing yellow fluorescing bacteria on top of a layer of bioink containing blue fluorescing bacteria. To facilitate imaging, a glass coverslip served as the printing substrate

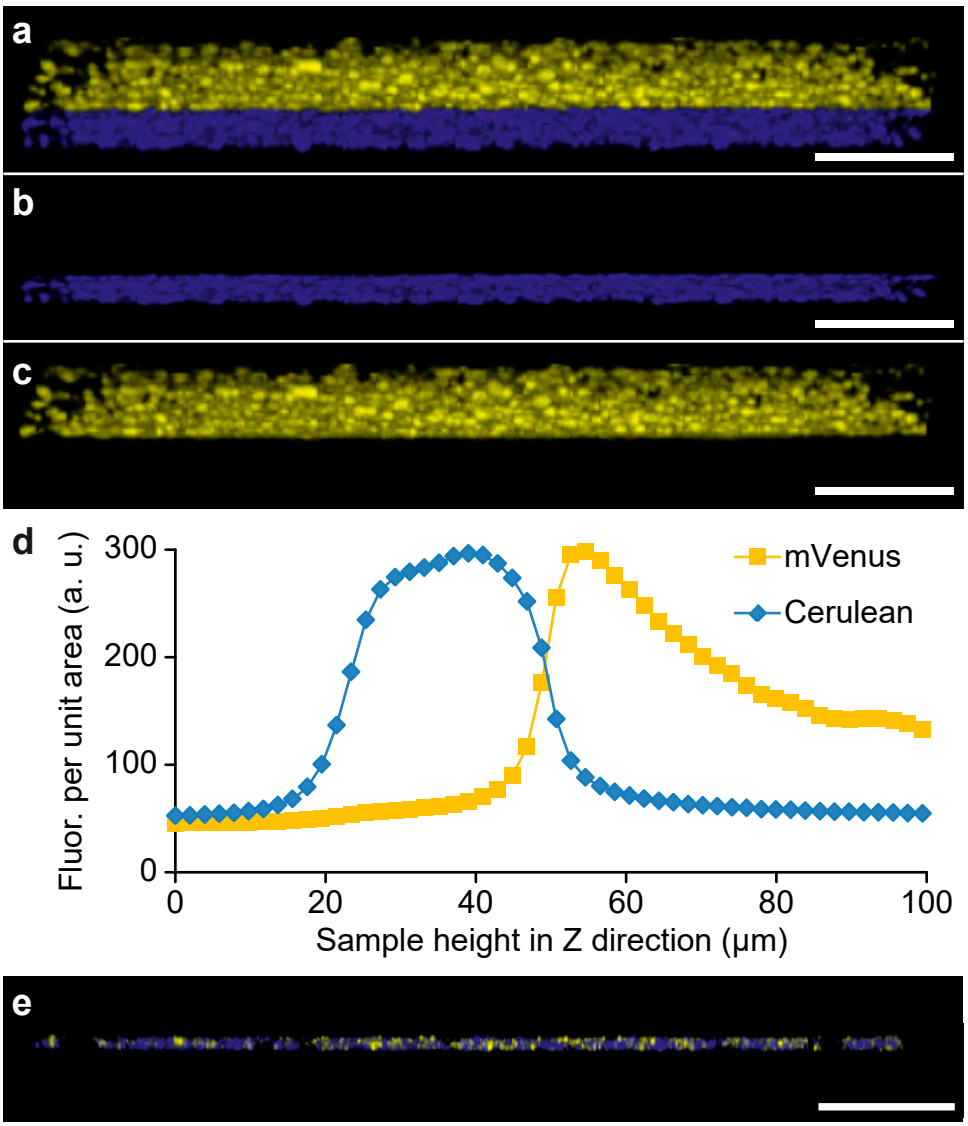


Figure 6.6: The Biolinker can print bacterial layers with spatial separation in the z-direction. A layer of bioink containing blue fluorescing bacteria was printed on a glass coverslip, followed by a layer of bioink containing yellow fluorescing bacteria. The interface between the layers was examined by confocal microscopy. (a-d) The bioink was solidified with $Ca^{2+}$ after each printed layer. (a) Composite image of blue and yellow detection channels. (b) Blue channel only. (c) Yellow channel only. (d) Fluorescence per area of (a) measured along the z-axis for each channel separately. (e) Bioink layers were printed and imaged as in (a) but without the addition of $Ca^{2+}$ ions (composite image). Scale bars are 100 µm.

instead of an agar plate. After each printing cycle, we added calcium chloride solution to solidify the alginate in the bioink. Thirty minutes after solidification of the second layer, we imaged the printed material along the z-axis using fluorescent confocal microscopy (Figure 6.6a–c). Quantification of the distributions of the different colors of bacterial fluorescence revealed that the bacteria mixed on a stretch of approximately 16 µm along the z-axis (maximum to maximum, Figure 6.6d). When the bioink layers were not solidified with calcium ions, the two types of bacteria were thoroughly intermixed, and a 3D structure failed to form (Figure 6.6e). The alginate bioink chemistry is thus an essential prerequisite to produce layered 3D structures.

### 6.2.4. CSGA EXPRESSION IS RATE-LIMITING FOR CURLI FORMATION

In order to 3D-print biofilms using the Biolinker, we wished to engineer our printed cells to inducibly overexpress curli fiber proteins. Curli fibers are constructed outside the cell from CsgA monomers [25]. Each fiber is attached to a CsgB outer membrane protein [26]. We applied a mathematical modeling approach to determine whether both CsgA and CsgB would need to be overexpressed in order to promote robust, inducible curli fiber growth. We used a simple kinetic model to estimate the growth rate of the fibers, from which we could estimate the extracellular CsgA production rate $r$. We have:

$$\begin{aligned} \frac{dM}{dt} &= nP - \gamma_M M - \mu M, \\ \frac{dC}{dt} &= k_t M - \gamma_C C - \mu C - k_e C, \\ r &= k_e C \end{aligned}$$

where $M$ and $C$ are the number of *csgA* mRNA and CsgA protein molecules per cell, $n$ the copy number of the (plasmid containing the) *csgA* gene, $P$ the promoter activity, $\gamma_M$ and $\gamma_C$ the degradation rate of *csgA* mRNA and CsgA protein, $\mu$ the growth rate of the cells, $k_t$ the translation rate, and $k_e$ the CsgA export rate constant, which we assumed to be constant since the CsgA transporter CsgG is ATP-independent [34]. Under steady-state conditions, the time derivatives and the growth rate are equal to zero. We then solved for the extracellular CsgA production rate as a function of the promoter activity and the various constants:

$$r = \frac{k_e}{k_e + \gamma_C} \frac{n k_t}{\gamma_M} P \approx \frac{n k_t}{\gamma_M} P$$

where we made the approximation that the export rate constant is significantly larger than the degradation rate of CsgA protein. We estimated the CsgA production rate by adding a GFP reporter to a rhamnose-inducible CsgA construct and measuring the steady-state bacterial fluorescence upon rhamnose induction (Section 6.4.13). For a rhamnose concentration of 0.2%, we determined an extracellular CsgA production rate of 2 molecules per second for a cell, with $n \approx 200$ copies of the *csgA* plasmid. When we raised the rhamnose concentration to 0.5%, the production rate increased to 3 molecules per second. Since the number of CsgB anchors on the outer membrane is in the range of $10^2$–$10^3$ [35], we concluded that the CsgA production is the rate-limiting step for the

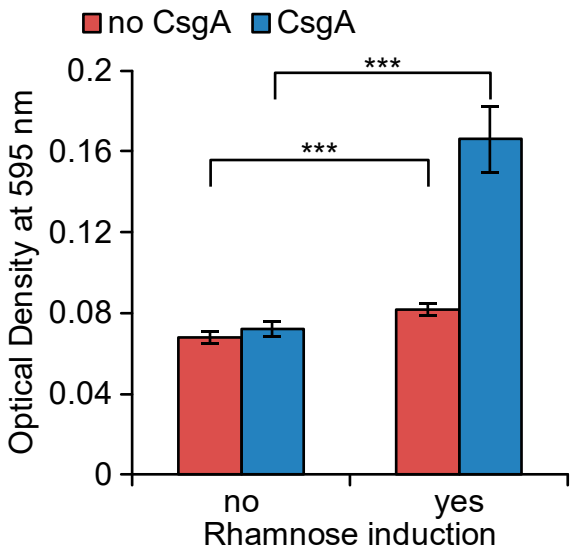


Figure 6.7: *E. coli ΔcsgA* forms biofilms in solution when induced to express CsgA. *E. coli ΔcsgA* expressing GFP (red) or GFP and rhamnose-inducible CsgA (blue) was grown for five days in the presence or absence of the inducer rhamnose and stained with Crystal Violet. Crystal Violet staining was detected by measuring absorption at $OD_{595}$ with a spectrophotometer. *** = significant difference ($p < 0.0005$), error bars represent the standard deviation, $n = 64$.



curli formation and that placing the csgA gene behind an inducible promoter will allow us to control the curli growth rate.

### 6.2.5. BIOFILM FORMATION CAN BE CONTROLLED BY EXOGENOUS EXPRESSION OF CSGA

Our modeling results suggested that control over biofilm formation can be achieved by genetic control of the *csgA* gene alone, while all other proteins involved in biofilm formation can be left untouched. To validate this result experimentally, we transformed a *csgA* knockout strain (*E. coli ΔcsgA*) with either a plasmid for inducible expression of CsgA or a control plasmid without the *csgA* gene. Due to the lack of genomically-encoded CsgA, these strains are not able to form biofilms naturally [36]. We tested these strains for biofilm formation in a microtiter plate assay [37]. Overnight bacteria cultures were diluted 1:100 with LB medium and grown in 96-well microtiter plates for five days at room temperature in the presence of the inducer rhamnose or the non-inducing sugar glucose. Planktonic cells were washed away, and remaining biofilm was stained with Crystal Violet. The Crystal Violet dye was then dissolved in ethanol and detected via optical density at 595 nm. For both strains, we measured a significantly higher amount of biofilm when the bacteria were grown in the presence of the inducer (Mann-Whitney U-test, $p < 0.0005$). Bacteria not expressing CsgA showed a 20% increase in biofilm formation in the presence of the inducer, while bacteria containing the plasmid for CsgA production showed a robust 131% increase in biofilm formation upon induction (Figure 6.7). These

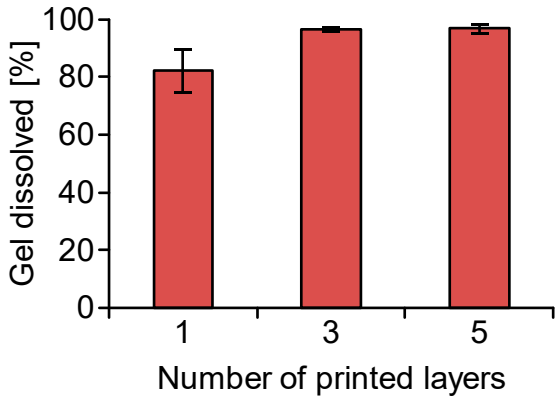


Figure 6.8: Sodium citrate can dissolve multi-layer printed alginate gels. Alginate (2% w/v) solutions were printed in varying numbers of layers with the Biolinker onto agar plates and allowed to form gels. The alginate was then submerged in 0.5 M sodium citrate. Dissolution efficiency was determined by weighing. Error bars represent the standard deviation, $n = 3$.

results confirm that our plasmid encoding for inducible control of CsgA expression alone was indeed sufficient to induce the formation of engineered *E. coli* biofilms in solution.



### 6.2.6. CSGA-EXPRESSING BACTERIA ALLOW THE PRODUCTION OF PATTERNED BIOFILMS

In order to create useful model biofilms, printed bacteria should form a biofilm-like structure in the alginate matrix that stably links the printed bacteria cells together, even when the alginate is dissolved. The gelation process of alginate is reversible; calcium can be washed out or removed by strong calcium-complexing agents such as citrate, dissolving the gels [38]. To test the efficiency of dissolution of 3D-printed alginate gels, we printed samples with different numbers of layers onto agar plates and compared their weight before and after dissolution with sodium citrate (Figure 6.8). We observed dissolution of 82.1% ± 7.9% (SD) of one-layered gels, 96.5% ± 1.1% of three-layered gels, and 96.8% ± 2.1% of five-layered gels, indicating that printed alginate gel can be dissolved nearly completely.

If our printed *E. coli* cells were able to efficiently form curli fibers in an alginate matrix, we would expect that the fibers would stabilize the matrix and take over the role of the alginate, keeping the cells in place upon dissolution of the alginate gel. To test the effect of CsgA expression, *E. coli ΔcsgA* containing either a plasmid for constitutive GFP expression, or a plasmid for constitutive GFP as well as inducible CsgA expression, was added to bioink and printed onto LB-agar plates containing the inducer rhamnose. The bioink was incubated for three days to allow for curli production, and then the total fluorescence of the plates was measured. Subsequently, the alginate gels were treated with sodium citrate solution for an extended period (2 hours) to thoroughly dissolve the alginate matrix, and the total fluorescence of the plates was measured again (Figure 6.9). Before citrate treatment, both printed gels showed strong fluorescence of similar intensity. After citrate treatment, the total fluorescence of the plate containing printed bac-

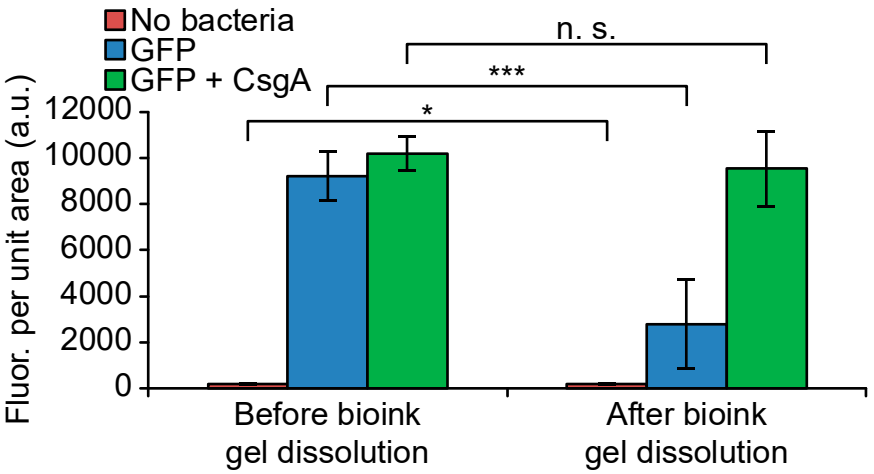


Figure 6.9: Printed bacteria that express CsgA are protected from alginate gel dissolution. Bioink was printed onto LB-agar plates and allowed to solidify. We printed bioink containing no bacteria (red bars), *E. coli ΔcsgA* expressing only GFP (blue bars), or *E. coli ΔcsgA* expressing both GFP and CsgA (green bars). The bioink gels were dissolved, and the average plate fluorescence both before and after dissolution was measured with a fluorescence scanner. * = significant difference ($p = 0.014$), *** = significant difference ($p < 0.0005$), n. s. = non-significant difference, error bars represent the standard deviation, $n = 10$.



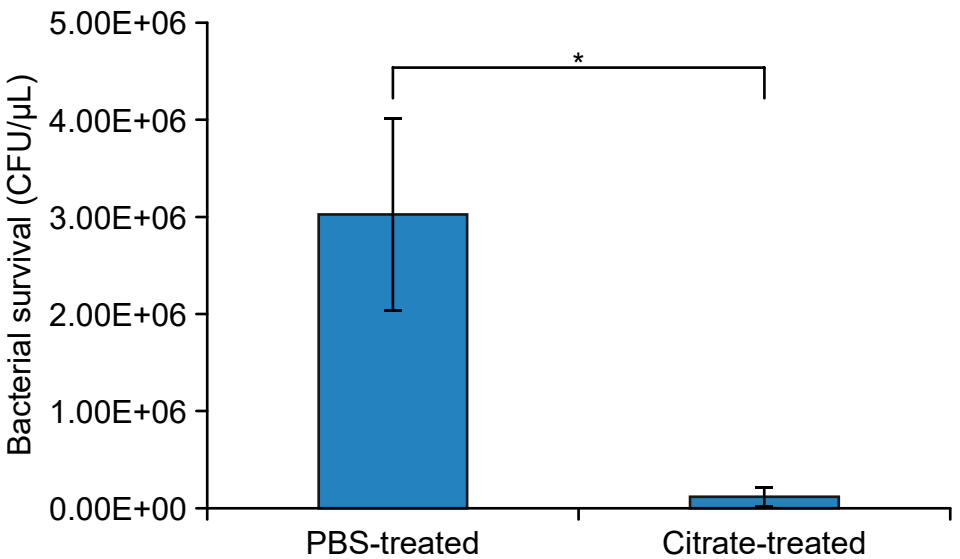


Figure 6.10: Citrate solution shows a cytotoxic effect when used to dissolve bioink for two hours. 2 mL bioink containing *E. coli* AM401 (constitutive GFP) was printed onto LB-agar plates containing $CaCl_2$ (resulting in a bioink gel) or not (resulting in a liquid culture on the agar surface). After 3 days of incubation at 37 °C, 20 mL of 0.5 M sodium citrate solution (pH 7 with NaOH) was added to the bioink gel and 20 mL of PBS to the liquid culture. The plates were incubated for 2 h on a rotatory shaker at 60 rpm to dissolve the bioink gel. Samples were taken and serial dilutions plated on agar plates to determine colony forming units per microliter of bioink. Error bars represent the standard deviation, * = significant difference ($p = 0.01$), $n = 6$.

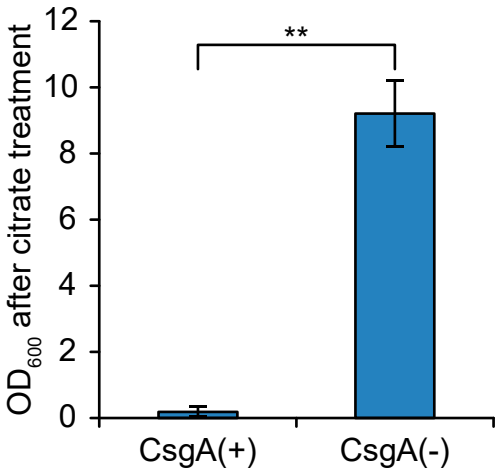


Figure 6.11: Citrate treatment of bioink gels causes release of non-CsgA-producing bacteria, but not CsgA-producing bacteria. Identical lines of bioink containing *E. coli* AM404 (constitutive GFP, inducible CsgA, left) or *E. coli* AM401 (constitutive GFP, right) were printed onto LB-agar plates containing the inducer rhamnose. After 8 days of incubation at room temperature, the gels were treated with 10 mL 0.5 M sodium citrate solution (pH 7 with NaOH) and incubated for 2 h on a rotatory shaker at 30 rpm. The optical density of the citrate solution at 600 nm was determined, and the average $OD_{600}$ of 0.02 obtained from treating bacteria-free bioink was subtracted from the results. Error bars represent the standard deviation, ** = significant difference ($p$ = 0.004), $n = 6$.



teria lacking CsgA had decreased significantly (paired t-test, $t(9) = -13.2$, $p < 0.0005$), indicating that the bacteria had been largely washed away. In contrast, the fluorescence intensity of plates containing printed CsgA-expressing bacteria was not significantly affected by the citrate treatment ($t(9) = -1.75$, $p = 0.114$). Although this harsh, extended citrate treatment resulted in a significant decrease in bacterial viability (Figure 6.10, independent samples t-test, $t(10) = 6.44$, $p = 0.01$), removal of printed alginate gel for engineering applications could be achieved through milder and less cytotoxic strategies such as the use of lower citrate concentrations, alternative chemicals such as EDTA, or submersion of the gel in low-calcium solutions.

To measure the physical stability of printed *E. coli* in a fluorescence-independent manner, we measured the optical density of citrate solutions used for bioink dissolution in order to detect the release of bacteria from printed bioink gels. Following citrate treatment of bioink gels containing CsgA-deficient bacteria, we found that the citrate solution had a mean optical density of $9.2 \pm 1.0$ (SD), which was approximately 50 times higher compared to citrate solutions used to treat bioink gels containing CsgA-expressing cells (Figure 6.11, Mann-Whitney U-test, $p = 0.004$). These data indicate that CsgA-deficient cells were released into suspension in large numbers due to the citrate treatment, while CsgA-expressing cells were stably and homogeneously anchored within the bioink gel. These results show that curli fibers can take over the function of alginate as fixation agents for printed bacteria, while at the same time mimicking the extracellular matrix of certain natural *E. coli* biofilms.

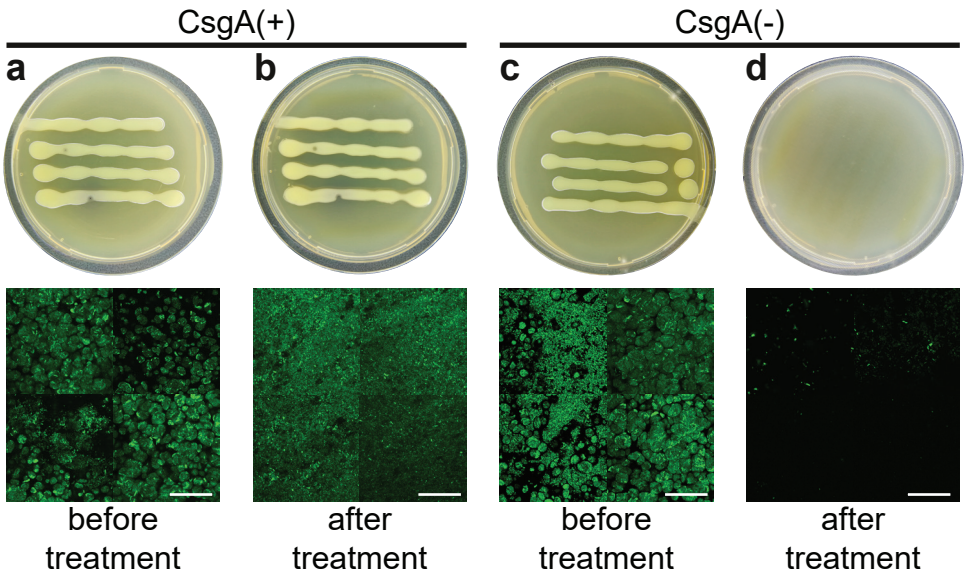


Figure 6.12: 3D-printed *E. coli* that express CsgA form patterned biofilms that are resistant to the gel-dissolving agent citrate. Bioink containing *E. coli ΔcsgA* either expressing GFP and CsgA (a, b) or only GFP (c, d) was printed in parallel lines by the Biolinker onto LB-agar plates and allowed to solidify. After incubation for three days at room temperature, the plates were treated with 0.5 M citrate for 2 h to dissolve the alginate gel. (upper row) Macroscopic images depicting the entire petri dish. (lower row) Representative confocal images, scale bars are 50 µm.



We next tested whether CsgA expression would allow our printed bacteria to retain a specific spatially patterned shape. We printed parallel stripes of bioink containing *E. coli* expressing CsgA, as well as stripes of bioink containing *E. coli* not expressing CsgA. After incubation for three days to allow the production of curli fibers, we attempted to dissolve the stripes with a sodium citrate solution. Stripes of bioink containing CsgA-producing *E. coli* maintained their striped pattern (Figure 6.12a, b, upper panels; Figure 6.13), while stripes of CsgA-deficient cells dissolved gradually from the bioink gel surface towards the printing surface until they were largely obliterated (Figure 6.12c, d, upper panels; Figure 6.13). When imaging printed bioink gels using confocal microscopy, we found the bacteria of both genotypes arranged in clusters of varying sizes, ranging from approximately 5–35 µm in length along the longest axis (Figure 6.12a, c, lower panels). Following citrate treatment, bioink containing CsgA-expressing bacteria appeared more homogeneous than before treatment, with fewer apparent bacteria clusters (Figure 6.12b, lower panel). Citrate-treated bioink containing CsgA-deficient cells had retained only a small number of cells directly in contact with the agar surface (Figure 6.12d, lower panel). The formation of bacteria clusters seen in untreated bioink might have been caused by microcolony growth under spatial constriction by the alginate gel or the developing curli network, with larger clusters potentially arising from the merging of smaller, neighboring clusters. The more homogeneous distribution of cells in citrate-treated bioink containing CsgA-expressing cells may have been due to a loss of integrity of the printed gel

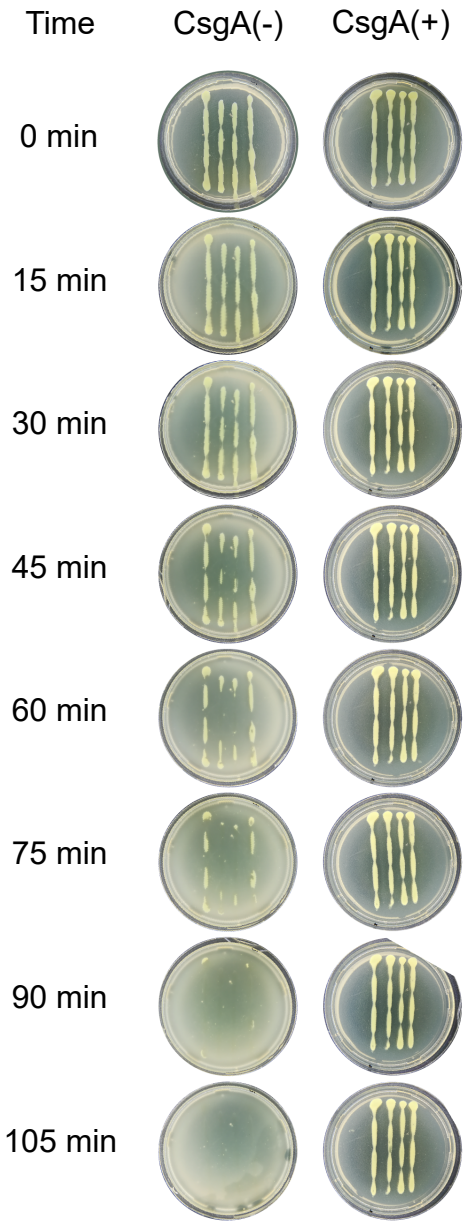


Figure 6.13: Bioink containing bacteria expressing CsgA resists dissolution with citrate. Bioink containing *E. coli* AM401 (constitutive GFP, left column) and *E. coli* AM404 (constitutive GFP, inducible CsgA, right column) were printed onto LB-agar plates containing the inducer rhamnose. After 3 days of incubation at room temperature, the gels were treated with 20 mL 0.5 M sodium citrate solution (pH 7 with NaOH) and incubated for 105 min on a rotatory shaker at 60 rpm. Images were taken every 15 min. The lighter color of the plates in the left column is likely caused by GFP-expressing bacteria going into suspension during the dissolution of the gel (see Figure 6.11).

following alginate removal, so that the pressure of a microscope cover slip might have introduced imaging artifacts by disturbing the microstructure of the film. In conclusion, these results show that printed engineered biofilms of *E. coli* can remain stably spatially patterned on a macroscopic level even when treated with a strong gel-dissolving agent.

## 6.3. CONCLUSION

We have developed a new method for the 3D printing of stable, patterned bacterial biofilm-inspired materials. While our engineered biofilms do not reproduce every feature of natural biofilms, our method allows for precise control over certain biofilm characteristics, such as spatial arrangement, species composition, and bacterial density. 3D printing could be used to produce standardized, reproducible biofilms for the evaluation of protective anti-biofilm coatings on medical devices, or for the testing of treatments against curli-forming pathogens. Further research is required to establish which features of biofilms of curli-forming bacteria are reproduced by our artificial biofilms, and how printed biofilms compare to other biofilm model systems such as the Calgary biofilm device and others [29, 39]. Schaffner et al. have demonstrated that oxygen limitation impacts the metabolic activity of bacteria in 3D-printed gels [16]. To deal with limitations in nutrient and oxygen supply, 3D printing could be used to arrange bacteria in combination with water channels, such as those found in natural biofilms [40]. We would like to note that while we did not observe the emergence of bacteria sub-populations in printed bioink, our results do not necessarily preclude physiological heterogeneity of the cells.



An important feature of 3D printing not available in other biofilm fabrication methods is the possibility to print and arrange different types of bacteria in a controlled fashion in 3D space. Synthetic microbial consortia are increasingly used to investigate bacterial interactions or to create complex synthesis pathways spanning several distinct types of bacteria [41–43]. The controlled spatial arrangement of these interacting bacteria groups could lead to further optimization in interaction-dependent processes [44], for which 3D printing has already been shown to be a promising tool [45]. In foundational research, biofilms can be modeled as layered structures to account for biofilm heterogeneity [46]. 3D printing of biofilms in layers according to model parameters could be a way to validate these models. Finally, curli fibers functionalized with peptide tags [36, 47] have recently emerged as new tools for the production of new nanomaterials [48], with diverse potential applications such as electronics [36, 49] or bioremediation [50]. 3D printing could make a valuable contribution to these approaches by providing a means of patterning and scale-up of materials production to the micro- and macroscale. When combined with calcium carbonate-producing bacteria, 3D-printed biofilms could be used to grow structures such as buildings [51], and to speed up the production of bacterial nacre considerably.

## 6.4. METHODS

Chemicals were purchased from VWR Netherlands or Sigma Netherlands unless otherwise indicated.

### 6.4.1. BACTERIAL STRAINS, PLASMIDS, AND CULTURE

*Escherichia coli* MG1655 *PRO ΔcsgA ompR234* [36, 52], henceforth called *E. coli ΔcsgA*, served as the experimental strain for experiments with inducible CsgA expression.

Liquid cultures of *E. coli* Top 10 and *E. coli ΔcsgA* cells were grown at 37 °C under continuous shaking in LB medium unless otherwise indicated. When carrying plasmids, appropriate antibiotics were added to the growth medium (25 μg mL$^{-1}$ ampicillin, 25 μg mL$^{-1}$ kanamycin, 34 μg mL$^{-1}$ chloramphenicol). For chemical induction of genes, inducer concentrations were 1 mM IPTG, 50 ng mL$^{-1}$ anhydrotetracycline, and 0.2% (w/v) or 0.5% (w/v) rhamnose or 0.5% (w/v) glucose (for non-inducing conditions).

Plasmid AM420 is a p15A-derived plasmid carrying an ampicillin resistance gene, a constitutively expressed *lacI* gene, and the gene for the blue fluorescent protein Cerulean (gene sequence originally from pZS2-12351, Addgene plasmid # 26598) behind an IPTG-inducible lac UV5 promoter [53].

Plasmid AM421 is a pSC101-derived plasmid carrying a kanamycin resistance gene, a constitutively expressed *tetR* gene, and the gene for the yellow fluorescent protein mVenus (gene sequence originally from mVenus N153, Addgene plasmid # 27793) behind an anhydrotetracycline-inducible promoter [54].

Plasmid pSB1C3 is the standard iGEM shipping backbone, which contains a ColE1 origin and a chloramphenicol resistance gene. The copy number per cell is between 100 and 300 copies (`http://parts.igem.org/Part:pSB1C3`).

Plasmid BBa_K1583112 was assembled from pSB1C3 and a rhamnose-inducible promoter from BBa_K914003 which controls the *csgA* gene from BBa_K1583000 and the *GFPmut3b* [55] gene from BBa_E0040.

Plasmid AM401 was constructed by inserting the biobrick BBa_I20270 (encoding for GFP behind a constitutive promoter) into plasmid pSB1C3.

Plasmid AM404 was assembled by inserting the BBa_I20270-part of AM401 into BBa_K1583100 (plasmid pSB1C3 containing a rhamnose-inducible promoter followed by the *csgA* gene).

Sequences of plasmids constructed in this work are accessible online (Table 6.1). iGEM plasmid sequences (plasmids pSB1C3 and BBa_plasmids) can be found in the iGEM Registry of Standard Biological Parts (`http://parts.igem.org`).

Table 6.1: Plasmid sequences have been deposited in the Inventory of Composable Elements (`https://acs-registry.jbei.org/login`) under the following accession numbers:

| Number | Plasmid |
|---|---|
| ACS_000669 | AM401 |
| ACS_000668 | AM404 |
| ACS_000667 | BBa_K1583112 |
| ACS_000666 | AM421 |
| ACS_000665 | AM420 |

Table 6.2: K'NEX parts of the Biolinker.

| Component | Amount | Cost per part | Total |
|---|---|---|---|
| Rods | | | |
| 19.2 cm gray | 12 | €0.49 | €5.88 |
| 13 cm red | 11 | €0.26 | €2.86 |
| 8.6 cm | 31 | €0.07 | €2.17 |
| 5.4 cm | 8 | €0.16 | €1.28 |
| Connectors | | | |
| 8 way white | 6 | €0.49 | €2.94 |
| 5 way yellow | 11 | €0.09 | €0.99 |
| 3 way red | 19 | €0.06 | €1.14 |
| 2 way orange | 16 | €0.22 | €3.52 |
| 4 way corner purple/gray | 44 | €0.17 | €7.48 |
| 8 way corner blue | 8 | €0.38 | €3.04 |
| Clips | | | |
| gray 1 pin | 11 | €0.03 | €0.33 |
| Special | | | |
| Motor | 2 | €10.80 | €21.60 |
| XL gear | 2 | €12.98 | €25.96 |
| M gear | 6 | €1.81 | €10.86 |
| S gear | 2 | €0.81 | €1.62 |
| Other | 4 | €1.00 | €4.00 |
| Chain members | 76 | €0.07 | €5.32 |
| Total (excl. tax ) | | | €103.72 |
| Total (including 21% tax) | | | €125.50 |

### 6.4.2. THE BIOLINKER

The frame and stage of the Biolinker were built from various K'NEX and electronic parts (Tables 6.2, 6.3), including two 5 V DC K'NEX motors to move the stage along the x- and y-axes (Table 6.4, Figure 6.2). These K'NEX motors must run at full speed in order to produce enough torque to prevent unexpected stalling of the stage. The motors are controlled by an Arduino Mega 2560 equipped with an Adafruit Motor Shield (V1). The Biolinker is controlled by sending commands in the form of G-codes (Table 6.5) via a USB serial interface from a computer. A graphical user interface (GUI) was programmed in Processing. Source codes for the Arduino drivers and the GUI have been deposited on Github (`https://github.com/dominikschmieden/biolinker`).

The senders and receivers of ultrasound sensors (HC SR-04) were detached, connected to their original circuit boards by cables, and attached facing each other to the stage and the frame (Figure 6.14). This modification allows direct transmission of the

Table 6.3: Electronic parts of the Biolinker.

| Component | Amount | Cost per part | Total |
|---|---|---|---|
| Arduino mega | 1 | €45.00 | €45.00 |
| Arduino uno | 1 | €25.00 | €25.00 |
| Ultrasound sensor | 2 | €12.00 | €24.00 |
| Adafruit motor shield | 1 | €20.00 | €20.00 |
| Power supply 9 V | 1 | €25.00 | €25.00 |
| Power supply 5 V | 1 | €25.00 | €25.00 |
| Stepper motor Nema 17 | 1 | €10.00 | €10.00 |
| Motor control chip | 1 | €12.00 | €12.00 |
| Misc. parts (cables etc.) | 1 | €30.00 | €30.00 |
| Total (including 21% tax) | | | €216.00 |

Table 6.4: The speed of the printer stage and overshoot of the stage after the motor is turned off. The speeds were calculated from the linear regions of the curves in Figure 6.2. The overshoots were measured as stage distance traveled after STOP command. Errors represent the standard deviation.

| X axis | |
|---|---|
| Speed forward [mm/s] | $18.61 \pm 0.14$ |
| Speed backward [mm/s] | $18.23 \pm 0.25$ |
| Overshoot forward [mm] | $1.80 \pm 0.75$ |
| Overshoot backward [mm] | $2.00 \pm 0.63$ |
| **Y axis** | |
| Speed forward [mm/s] | $15.74 \pm 0.07$ |
| Speed backward [mm/s] | $16.40 \pm 0.07$ |
| Overshoot forward [mm] | $2.20 \pm 0.40$ |
| Overshoot backward [mm] | $112.20 \pm 0.75$ |



ultrasound signal from sender to receiver without reflection on a surface. This setup was used to determine the position of the stage in x- and y-direction.

The printhead consists of a syringe tip (Sterican, 19G × 1.5") glued to a K'NEX holder in a central position above the stage's area of movement. The tip was blunted by shortening with pliers and filing down to the un-deformed region of the tube. Bioink is pumped through silicon tubing (VWR DENE 3100103/25, 1 mm inner diameter) by an open-source peristaltic pump (`http://www.thingiverse.com/thing:529863`). The pump rotor and stator were 3D-printed with a Form 1+ 3D printer (Formlabs). The pump stepper motor is controlled by a separate Arduino Uno board and a DRV8824 motor control chip. Commands from the Arduino Mega board to the pump board are sent via the SCA/SCL ports.

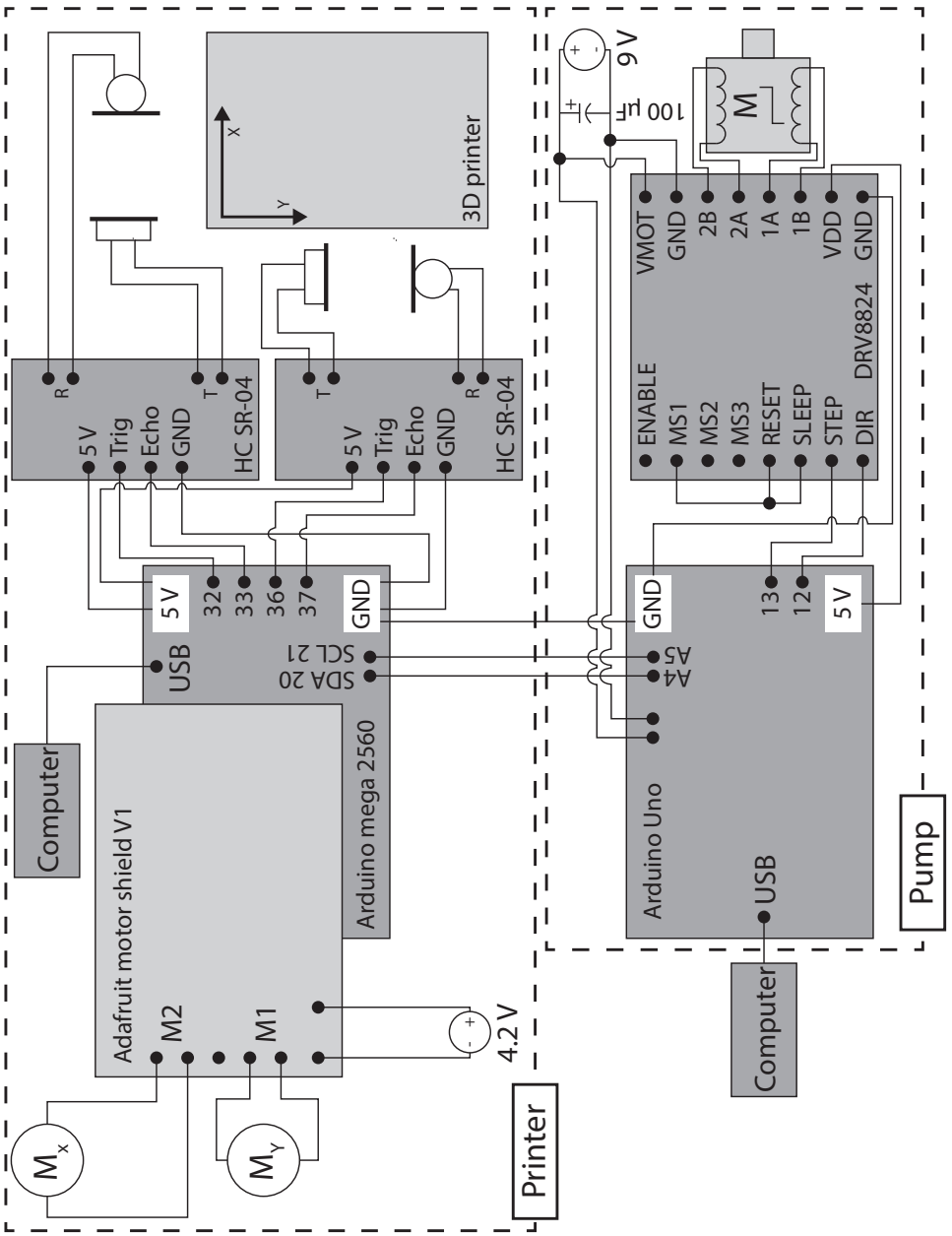


Figure 6.14: Circuit diagram of the Biolinker.

Table 6.5: Biolinker commands sent from the graphical user interface to the Arduino Uno of the printer.

| Command | Example | Explanation |
|---|---|---|
| G0 x y z | G0 50 40 10 | Moves the stage to the specified coordinates (in millimeters), ranging from 0 to the maximum value determined by calibration. |
| G1 x y z | G1 50 40 10 | As G0 x y z, but the pump runs at the same time. |
| G4 t | G4 3000 | Wait for t milliseconds. |
| M114 | M114 | Output the current coordinates (mm) to the serial interface. |
| T1 d s | T1 0 100 | Turn on pump 1: d=direction (1 or 0), s=speed (0–40 ). Use "T1 0 0" to switch off pump. |
| T3 m d s | T3 0 0 255 | Direct motor control: m=motor (0 or 1), d=direction (1 or 0), s=speed (can range from 0–255 0-255, but motors stall at lower speeds). |
| T5 | T5 | Switch off all motors and pumps. |
| T10 | T10 | Calibration: set the current stage position to zero X and Y. |
| T11 | T11 | Calibration: set the current stage position to maximum X and Y. |



### 6.4.3. BIOINK PREPARATION

Bioink was prepared by growing bacteria overnight in 50 mL LB medium with appropriate antibiotics and inducers, then centrifugation for 5 min at 3600 × *g*. The cell pellet was re-suspended in 10 mL LB medium and 10 mL sodium alginate (3% w/v). Sodium alginate solutions were heated to their boiling point three times after production and stored at 4 °C to prevent the growth of contaminants. For experiments without bacteria, alginate solutions were dyed with 5 mg mL$^{-1}$ of Methylene Blue prior to printing to allow imaging and measurements.

### 6.4.4. PRINTING SUBSTRATES

The printing of bacteria was performed on LB-agar plates (1% w/v), supplemented with appropriate antibiotics and inducers. Liquid agar was poured into plates standing on level surfaces to promote a level agar surface after cooling. Plates were dried overnight at room temperature with the lid half-open. To allow alginate gel solidification, a solution of 0.1 M $CaCl_2$ was spread on the plates prior to printing (1 mL for diameter=135 mm plates, 444 µL for diameter=90 mm plates). $CaCl_2$ was added to solid rather than to liquid agar since addition immediately before printing resulted both in better alginate gelation during the printing process, as well as better dissolution of the alginate gel in calcium removal experiments. For experiments without bacteria, printing substrates were prepared by dissolving 1% agar in water. After pouring, solidification, and drying, the $CaCl_2$ solution was spread on the plates as described above.

### 6.4.5. CHARACTERIZATION OF LINE WIDTHS

The width of alginate gel lines printed with the Biolinker was determined by printing dyed alginate onto agar plates (1% in $H_2O$) along the printer's y-axis at different speed settings. Between prints of different layers, the plates were incubated at 4 °C for 10 min to allow for gel solidification while limiting dye diffusion into the agar. After printing, the plates were imaged, and the layer width was measured at fixed-distance intervals along the lines.

### 6.4.6. CONFOCAL MICROSCOPY

Bioink gels were imaged with a Nikon A1+ fluorescence confocal microscope (For analyzing spatial separation in the z-direction: magnification 200×, 1.95 µm Z direction step size, excitation wavelengths 457/514 nm, detected wavelengths 482/540 nm for Cerulean and mVenus, respectively. For imaging of bacteria spatial distribution within printed bioink stripes: magnification 1000×, oil immersion, excitation wavelength 488 nm, detected wavelength 540 nm for GFP). Quantification of fluorescence along the Z-axis was performed image by image with the software ImageJ [56].

### 6.4.7. PRINT AND MICROSCOPY OF LAYERED BIOINK STRUCTURES

Bioink was prepared containing Top10 strains carrying plasmids AM420 (inducible Cerulean) or AM421 (inducible mVenus, 5 mL overnight culture with inducers, 500 µL LB medium, 2 mL 2% (w/v) alginate). Bioink containing AM420 was printed with the Biolinker (extrusion speed 1.6 mL min$^{-1}$) onto an oxygen plasma-treated glass coverslip (30% power for 25 s, Plasma Preen I) and solidified by application of 5 M $CaCl_2$ solution with a pipette on the edges of the alginate gel, allowing for slow diffusion into the gel from the sides without disturbing the gel structure. Before deposition of the second layer of bioink, unbound $CaCl_2$ was removed by flushing the slide with at least 100 mL of tap water. A second layer of bioink containing AM421 was then generated on top of the first layer, using the same technique. The coverslip carrying the gel was placed on a microscope slide, and the gel was sealed with nail polish. Solidification steps with $CaCl_2$ were omitted in the non-gel control. Imaging by confocal microscopy was performed 30 min after solidification of the second layer.

### 6.4.8. BIOFILM FORMATION UPON EXPRESSION OF CSGA IN MICROTITER PLATES

Biofilm formation was measured with a microtiter plate assay [37]. *E. coli ΔcsgA* carrying plasmids AM401 (constitutive GFP) or AM404 (constitutive GFP and rhamnose-inducible CsgA) were grown overnight at 37 °C with shaking at 250 rpm in LB medium supplemented with 34 µg mL$^{-1}$ chloramphenicol. Cultures were then diluted 1:100 into 200 µL LB low salt medium (10 g L$^{-1}$ tryptone, 5 g L$^{-1}$ yeast extract, supplemented with 0.5% (w/v) rhamnose or glucose and 34 µg mL$^{-1}$ chloramphenicol) per well of 96-well transparent, flat bottom microtiter plates (Greiner Bio-One 655185). Plates were incubated at 30 °C for five days in a sealed container (with a layer of water below the plates to prevent drying out) to allow biofilm formation. Planktonic cells were removed by washing the plates three times via submerging in tap water and shaking off of the water. Biofilms were stained with 210 µL/well Crystal Violet solution (0.1% w/v in water) for 15 min

at room temperature. The dye was removed and the wells washed another three times with water. Residual water was removed by tapping the inverted plate vigorously onto paper towels and air drying. The wells were then filled with 200 µL/well 99% ethanol, covered, and incubated at room temperature for 15 min with shaking at 30 rpm. 100 µL of the ethanol solution was transferred from each well to a new microtiter plate, and $OD_{590}$ was measured with a Tecan Infinite M200 Pro plate reader. The data were analyzed with Mann-Whitney U tests.

### 6.4.9. ALGINATE GEL DISSOLUTION

Calcium ion-permissible dialysis membranes (Spectra/Por 2 Dialysis Tubing, 12–14 kDa MWCO, Spectrum Europe B.V., The Netherlands) were placed onto agar plates (1% in $H_2O$), and the Biolinker was used to print a layer of 2% alginate onto the membrane. After solidification of the alginate, additional layers of alginate were printed on top. For 5-layer samples, 1 mL of $CaCl_2$ solution was layered onto the gels after 3 layers.

To determine gel mass before and after dissolution, the membrane with the alginate gel was lifted off the agar plate, dried briefly with paper tissues, weighed, and replaced onto the dish. The gels were then submerged in 30 mL 0.1 M sodium citrate (adjusted to pH = 7 with NaOH) and incubated at room temperature on a rotary shaker at 30 rpm for 30 min. After incubation with sodium citrate, the membrane was lifted off again, dried, and weighed as before.



### 6.4.10. BACTERIAL SURVIVAL IN PRINTED BIOINK

Bioink was prepared containing *E. coli ΔcsgA* transformed with plasmid AM401 (constitutive GFP). 2 mL of this bioink was printed onto LB-agar plates (30 mL LB agar per plate, supplemented with chloramphenicol and $CaCl_2$). The plates were sealed with plastic wrap to reduce evaporation and incubated for twelve days at 37 °C. 1 mL of deionized water was added daily to all samples and spread evenly over both the agar and the bioink gel to compensate for the evaporative loss of liquid. No change of water level over the duration of the experiment was observed, so no dilution was assumed. Samples of the gel were taken with a scalpel at different time points. Due to the greater stability of the agar substrate compared to the bioink gel, the bioink could be removed without agar contamination. The extracted gels were weighed, and gel mass was correlated with pumped volume via a pre-determined calibration curve. The gel samples were transferred into 0.5 M sodium citrate solution (pH 7 with NaOH) and adjusted to a concentration of 50 µL pumped bioink per 1 mL gel-citrate mixture. The gels were dissolved by incubation for 10 min at room temperature with occasional vortexing and serially diluted with phosphate-buffered saline (PBS) in 1:10 increments. Samples from these dilutions were plated onto LB plates and incubated overnight at 37 °C. Colonies were counted to determine colony forming units per microliter of pumped bioink.

To investigate the influence of gelation and 10-minute citrate treatment on bacterial survival, 2 mL of bioink was printed as described above, but onto substrate plates containing no $CaCl_2$, leading to a liquid culture on top of the agar surface. These plates were incubated and supplied with water in the same way as the gel samples. Samples were removed by shaking the plates for 1 h at 100 rpm on a rotatory shaker following water addition to re-suspend any sedimented bacteria, and 50 µL of the solution was trans-

ferred into 950 µL PBS or into 950 µL 0.5 M sodium citrate solution. After incubation for 10 min, serial dilutions of the samples were prepared and plated as described for the gel samples.

To determine the effect of a two-hour citrate treatment on bacterial survival, 2 mL of bioink containing *E. coli* AM401 (constitutive GFP) was printed onto LB-agar plates containing $CaCl_2$ (resulting in a bioink gel) or not (resulting in a liquid culture on the agar surface). After 3 days of incubation at 37 °C, 20 mL of 0.5 M sodium citrate solution (pH 7 with NaOH) was added to the bioink gel, and 20 mL of PBS was added to the liquid culture. The plates were incubated for 2 h on a rotatory shaker at 60 rpm to dissolve the bioink gel. 50 µL of the solution was transferred into 950 µL PBS. After incubation for 10 min, serial dilutions of the samples were prepared and plated as described above.

### 6.4.11. BIOFILM FORMATION IN ALGINATE GELS

Bioink was prepared containing *E. coli ΔcsgA* transformed with AM404 (constitutive GFP, rhamnose-inducible CsgA) or *E. coli ΔcsgA* with plasmid AM401 (constitutive GFP). For the bacteria-free control, only LB medium, alginate, and rhamnose were mixed.

This bioink was printed in a filled, single-layer polygon shape (extrusion speed 2.3 mL$\,$min$^{-1}$) onto LB-agar plates (supplemented with $CaCl_2$, 0.5% rhamnose, and chloramphenicol). The plates were incubated for three days at room temperature in darkness. Plate fluorescence was measured with a GE Typhoon Trio fluorescence scanner (excitation wavelength 488 nm, PMT 450 V, emission filter 520 BP 40, high sensitivity) and averaged over the printed area. The alginate gel was dissolved by the addition of 20 mL 0.5 M sodium citrate (adjusted to pH = 7 with NaOH) for 2 h with 30 rpm shaking at room temperature in darkness. The liquid was discarded, and plate fluorescence was measured again as before. The significance of differences was analyzed with paired t-tests.

### 6.4.12. RELEASE OF BACTERIA INTO CITRATE SOLUTION

Bioink was prepared containing *E. coli ΔcsgA* transformed with AM404 (constitutive GFP, rhamnose-inducible CsgA) or *E. coli ΔcsgA* with plasmid AM401 (constitutive GFP). For a bacteria-free control, only LB medium, alginate, and rhamnose were mixed.

Identical parallel lines of these bioinks were printed onto LB-agar plates (supplemented with $CaCl_2$, 0.5% rhamnose, and chloramphenicol). The plates were incubated for 8 days at room temperature, after which the gels were submerged in 10 mL 0.5 M sodium citrate solution (adjusted to pH = 7 with NaOH) for 2 h with 30 rpm shaking at room temperature. Samples of the liquid were taken, and the optical density at 600 nm determined with an Ultrospec 10 Cell Density Meter (Biochrom, US). 20× dilutions of CsgA(-) samples were measured to reach measurements of $OD_{600} < 0.5$. The mean $OD_{600}$ of cell-free bioink (0.02) was subtracted from the $OD_{600}$ values of the other bioinks.

### 6.4.13. ESTIMATES OF THE RATES USED IN THE KINETIC MODEL

In Section 6.2.4, we use a kinetic model to estimate the extracellular CsgA production rate $r$ as a function of the activity of the promoter, for which we find $r = nk_tP/\gamma_M$. Here $n = 200$ is the copy number of the plasmid, $k_t$ the translation rate of the *csgA* mRNA, $P$ the promoter activity, and $\gamma_M$ the degradation rate of the mRNA. To obtain an esti-

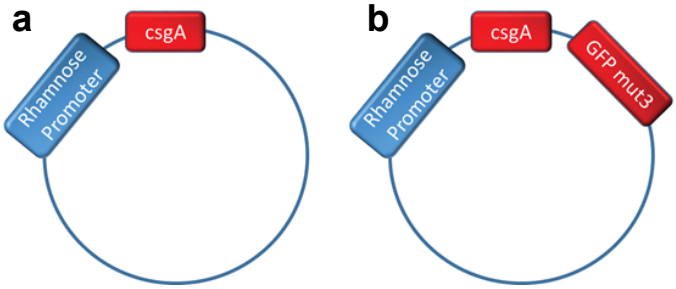


Figure 6.15: (a) Plasmid AM404, containing a rhamnose promoter controlling the expression of the *csgA* gene. (b) Plasmid BBa_K1583112 used in determining the promoter activity and transcription rate. This plasmid contains the *csgA* and *gfpmut3* genes under control of a rhamnose-inducible promoter.

mate for the production rate $r$, we used the plasmid BBa_K1583112, which, in addition to containing the csgA gene under control of a rhamnose promoter, also contains *gfpmut3* (coding for modified GFP variant with stronger fluorescent signal) under control of the same, rhamnose-inducible promoter (Figure 6.15). This plasmid contains the same rhamnose-inducible csgA gene as found in plasmid AM404, which was used to produce inducible curli fibers in the biofilm-production experiments throughout this work (Figure 6.15).

We transformed plasmid BBa_K1583112 into *E. coli ΔcsgA*. The resulting strain was grown in LB medium (supplemented with chloramphenicol) overnight at 37 °C at 250 rpm, diluted 50 times with LB medium, grown to exponential phase ($OD_{600}$ 0.4–0.6 ), and diluted again to $OD_{600}$ 0.05. Wells of a 96-well microtiter plate were filled with 180 µL of the bacterial culture and supplemented with rhamnose or water to concentrations of 0, 0.2, or 0.5% rhamnose. The plate was placed in a Tecan Infinite M200 Pro plate reader and incubated at 30 °C for 18 h. We measured both $OD_{600}$ and green fluorescence at 510 nm to obtain a fluorescence signal normalized by the number of cells (Figure 6.16).

We determined the fluorescence versus mass amount of purified GFPmut3 with a Tecan Infinite M200 Pro plate reader, using the same settings as for the kinetic experiment in Figure 6.15. By converting the measured fluorescence per $OD_{600}$ (Figure 6.16) to number of GFPmut3 molecules per cell, the GFP steady-state concentrations were determined to be $[GFP]^{SS} = 1.9 \times 10^4$ GFP molecules/cell at 0.2% rhamnose induction and $[GFP]^{SS} = 3.3 \times 10^4$ GFP molecules/cell at 0.5% rhamnose induction.

To relate the steady-state concentration of GFP to the various rates in our model, we replaced the CsgA protein with the GFP protein ($G$). The only difference between these proteins for the purpose of our modeling is that GFP is not transported out of the cell, so the number of GFP proteins can only decrease through degradation. We have:

$$\frac{dM}{dt} = nP - \gamma_M M - \mu M,$$
$$\frac{dG}{dt} = k_t M - \gamma_G G - \mu G.$$

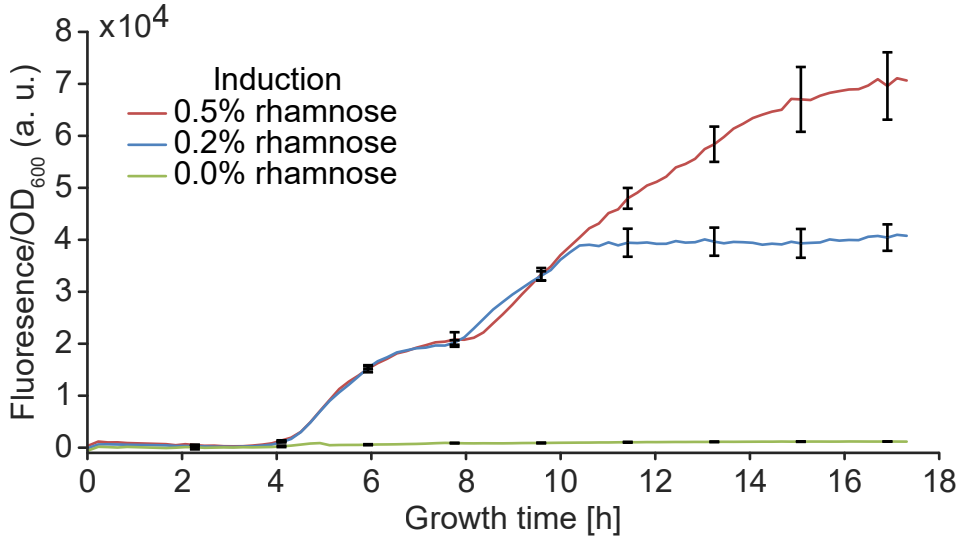


Figure 6.16: Fluorescence over time normalized by cell density of a culture of *E. coli ΔcsgA* containing BBa_K1583112, expressing both CsgA and GFP under control of a rhamnose-inducible promoter. $n = 3$



In steady-state conditions, the time derivatives and growth rate are equal to zero. The equilibrium concentration of G is therefore given by:

$$G^{SS} = \frac{k_t n P}{\gamma_g \gamma_M} = \frac{1}{\gamma_G} \frac{k_t n P}{\gamma_M} = \frac{1}{\gamma_G} r,$$

where $r$ is the extracellular CsgA production rate that we ultimately want to estimate. Since we have measured the steady-state concentration of GFP, all we need is the degradation rate of GFP. The value of this parameter turns out to be surprisingly hard to find in the literature. In *E. coli*, it is frequently assumed that GFP is effectively stable, at least compared to mRNA, for which the degradation rate has been measured to be $4.8 \times 10^{-3}$ s$^{-1}$ [57]. The degradation rate of YFP in yeast has been measured to be approximately $1.0 \times 10^{-4}$ s$^{-1}$ (Supporting Information of [58]). Using this value, we estimated an export rate for CsgA of about 2 molecules per second for the case if we induce with 0.2% rhamnose, rising to 3 molecules per second if we induce with 0.5% rhamnose.

## 6.5. STATISTICAL ANALYSES

### BIOFILM FORMATION CAN BE CONTROLLED BY EXOGENOUS EXPRESSION OF CSGA

Bacteria expressing CsgA or not expressing CsgA were tested for biofilm formation in a microtiter plate assay (Figure 6.7). Levene's test revealed inequality of error variances ($p < 0.0005$), and boxplots showed several outliers. For this reason, ANOVA was not used. Instead, a Mann-Whitney U test was run on the different bacterial genotypes separately

to determine if there were differences in biofilm formation between induced and uninduced cultures. The significance level was adjusted accordingly to 2.5%.

#### BACTERIA EXPRESSING GFP

Distributions of the optical densities were similar, as assessed by visual inspection. Accordingly, the U test was used to determine differences in median optical densities between the two groups. Median optical densities in induced cultures (0.08) were statistically significantly higher than in uninduced cultures (0.07), $U = 4091$, $z = 9.739$, $p < 0.0005$.

#### BACTERIA EXPRESSING GFP AND CSGA

Distributions of the optical densities were not similar, as assessed by visual inspection. Accordingly, the U test was used to determine differences in the distribution between the two groups. Optical densities for induced cultures (mean rank = 96.50) were statistically significantly higher than for uninduced cultures (mean rank = 32.50), $U = 4096$, $z = 9.760$, $p < 0.0005$.

### CSGA-EXPRESSING BACTERIA ALLOW THE PRODUCTION OF PATTERNED BIOFILMS

Fluorescence of alginate gels containing either no bacteria, bacteria expressing only GFP, or bacteria expressing both GFP and CsgA was measured before and after treatment with citrate (Figure 6.9). Outliers were identified by inspection of a box plot for values greater than 1.5 box-lengths from the edge of the box. One outlier was removed from the analysis (GFP-expression, fluorescence before/after: 12033.481/7343.035). Outliers in the no-bacteria samples were retained due to their low magnitude compared to the bacteria-containing samples. The remaining data points were normally distributed, as assessed by a Shapiro-Wilk's normality test ($p > 0.05$). Levene's test revealed inequality of error variances between before- and after-treatment measurements ($p < 0.0005$), preventing the use of a mixed ANOVA test. Instead, a pairwise t-test was performed for each genotype to assess fluorescence before/after citrate treatment. The level of significance was accordingly adjusted to 1.67%. Data are mean ± standard deviation unless otherwise stated.



#### NO BACTERIA

The difference scores for before/after treatment were normally distributed, as determined by Shapiro-Wilk's test ($p = 0.293$). Bacteria-free gels showed a fluorescence of $203.15 \pm 19.34$ before citrate treatment and a fluorescence of $186.78 \pm 18.47$ after treatment, representing a significant difference of $16.36 \pm 16.92$, $t(9) = -3.058$, $p = 0.014$, $d = 0.97$. The drop of fluorescence is likely due to loss of auto-fluorescence of the alginate gel that was washed away. Due to the low magnitude of the auto-fluorescence compared to the bacterial fluorescence, this change was neglected for the remainder of the analysis.

#### BACTERIA EXPRESSING GFP

The difference scores for before/after treatment were normally distributed, as determined by Shapiro-Wilk's test ($p = 0.682$). Gels containing GFP-expressing bacteria showed

a fluorescence of 9198.82±1161.88 before citrate treatment and a fluorescence of 2806.13± 2098.95 after treatment, representing a significant difference of 6392.69 ± 1527.69, $t(9) = -13.23$, $p < 0.0005$, $d = 4.18$.

#### BACTERIA EXPRESSING GFP AND CSGA

The difference scores for before/after treatment were normally distributed, as determined by Shapiro-Wilk's test ($p = 0.411$). Gels containing GFP- and CsgA-expressing bacteria showed a fluorescence of 10200.54 ± 842.03 before citrate treatment and a fluorescence of 9530.99 ± 1784.46 after treatment, representing a non-significant difference of 669.55 ± 1207.99, $t(9) = -1.75$, $p = 0.114$.

### PRINTED BIOINK GELS DISSOLVE IN CITRATE SOLUTION IF NO CSGA IS EXPRESSED

Bioink containing cells either expressing CsgA or not was printed onto LB-agar plates and incubated for 8 days. Thereafter, the gels were treated with citrate solution for two hours, and the $OD_{600}$ of the solution was determined as a measure of the number of bacteria cells suspended in solution. The data were not normally distributed, as determined by Shapiro-Wilk's normality test ($p < 0.05$). Consequently, a Mann-Whitney U Test was used. Distributions of the optical densities were not similar, as assessed by visual inspection. Accordingly, the U test was used to determine differences in the distribution between the two groups. Optical densities for CsgA-expressing bacteria (mean rank = 3.50) were statistically significantly lower than for CsgA-deficient bacteria (mean rank = 21.00), $U < 0.0005$, $z = -2.892$, $p = 0.004$.

### EXTENDED CITRATE TREATMENT HAS A CYTOTOXIC EFFECT ON PRINTED BIOFILMS

*E. coli ΔcsgA* transformed with AM401 (constitutive GFP) was grown as a liquid culture or in the form of printed bioink on agar plates. The liquid culture was treated with PBS, while the bioink was dissolved with citrate, and bacterial survival was measured as colony forming units. The data points for both conditions were normally distributed, as revealed by Shapiro-Wilk's normality test ($p > 0.05$). Levene's test revealed inequality of error variances between PBS- and citrate-treated samples ($p = 0.005$). An independent samples t-test revealed that the difference between both groups was significant ($t(10) = 6.44$, $p = 0.01$).

## 6.6. AUTHOR CONTRIBUTIONS

D.T.S. designed and performed all experiments except for the measurement of CsgA expression; performed the data analysis; designed, built, programmed, and characterized the Biolinker; and wrote the manuscript except for the modeling sections. S.J.B.V. and M.v.d.D. conceived of the initial idea and design of a K'NEX 3D bioprinter. S.J.B.V. performed and wrote the modeling sections throughout. H.S. and M.v.d.D. measured and analyzed the CsgA expression. T.I. and A.S.M. supervised the project and assisted in the writing of the chapter. All authors read and corrected the manuscript.

## 6.7. ACKNOWLEDGMENTS

*Escherichia coli* MG1655 *PRO ΔcsgA ompR2341* was gifted to us by Timothy K. Lu (Department of Biological Engineering, Massachusetts Institute of Technology). Plasmids AM420 and AM421 were constructed and gifted to us by Ferhat Büke. We thank Roland Kieffer, Simon Lindhoud, Victor Marin and Benjamin Lehner for helpful discussions about the printer design, as well as Ilja Westerlaken for assistance in the lab. We acknowledge Jeremie Capoulade for assistance with the confocal microscopy, as well as Jakob Söhl and Ewa Spiesz for help with statistical analyses. For the project idea and initial experiments, we thank the TU Delft 2015 iGEM team: Max van't Hof, Stefan Marsden, Tudor Vlas, Michelle Post, Liana Uilecan, Anne Rodenburg, Esengül Yildirim, Jorine Eeftens, and Helena Shomar Monges.

## REFERENCES

[1] D. T. Schmieden, S. J. Basalo Vázquez, H. Sangüesa, M. van der Does, T. Idema, and A. S. Meyer, *Printing of patterned, engineered e. coli biofilms with a low-cost 3d printer,* ACS Synthetic Biology **6**, 1124 (2018).

[2] L. Hall-Stoodley, P. Stoodley, S. Kathju, N. Høiby, C. Moser, J. William Costerton, A. Moter, and T. Bjarnsholt, *Towards diagnostic guidelines for biofilm-associated infections,* FEMS Immunology & Medical Microbiology **65**, 127 (2012).

[3] S. L. Percival, L. Suleman, C. Vuotto, and G. Donelli, *Healthcare-associated infections, medical devices and biofilms: risk, tolerance and control,* Journal of Medical Microbiology **64**, 323 (2015).

[4] Donlan, R. M., *Biofilms on central venous catheters: Is eradication possible?* in *Bacterial Biofilms*, edited by T. Romeo (Springer, Berlin, Heidelberg, 2008) pp. 133–161.

[5] T. T. Bauer, A. Torres, R. Ferrer, C. M. Heyer, C. Schultze-Werninghaus, and K. Rasche, *Biofilm formation in endotracheal tubes. association between pneumonia and the persistence of pathogens,* Monaldi archives for chest disease **57**, 84 (2002).

[6] I. Francolini and G. Donelli, *Prevention and control of biofilm-based medical-device-related infections,* FEMS Immunology & Medical Microbiology **59**, 227 (2010).

[7] X.-H. Li and J.-H. Lee, *Antibiofilm agents: A new perspective for antimicrobial strategy,* J. Microbiol. **55**, 753 (2017).

[8] G. Sharma, S. Sharma, P. Sharma, D. Chandola, S. Dang, S. Gupta, and R. Gabrani, *Escherichia coli biofilm: development and therapeutic strategies,* Journal of Applied Microbiology **121**, 309 (2016).

[9] E. Nagar and R. Schwarz, *To be or not to be planktonic? self-inhibition of biofilm development,* Environmental Microbiology **17**, 1477 (2015).

[10] L. Pu, S. Yang, A. Xia, and F. Jin, *Optogenetics manipulation enables to prevent biofilm formation of engineered pseudomonas aeruginosa on surfaces,* ACS Synthetic Biology **69**, 200 (2017).

[11] F. Chen and S. V. Wegner, *Blue light switchable bacterial adhesion as a key step toward the design of biofilms,* ACS Synthetic Biology **6**, 2170 (2017).

[12] K. Li, M. Whitfield, and Van Vliet, Krystyn J, *Beating the bugs: roles of microbial biofilms in corrosion,* Corrosion Reviews **31**, 73 (2013).

[13] Z. Lewandowski and J. P. Boltz, *4.15 - biofilms in water and wastewater treatment a2 - wilderer, peter,* in *Treatise on Water Science*, edited by T1 - 4.15 - Biofilms in Water and Wastewater Treatment A2 - Wilderer, Peter (Elsevier, Oxford, 2011) pp. 529–570.

[14] M. Vera, A. Schippers, and W. Sand, *Progress in bioleaching: fundamentals and mechanisms of bacterial metal sulfide oxidation—part a,* Applied Microbiology and Biotechnology **97**, 7529 (2013).

[15] A. Olivera-Nappa, C. Picioreanu, and J. A. Asenjo, *Non-homogeneous biofilm modeling applied to bioleaching processes,* Biotechnology and bioengineering **106**, 660 (2010).

[16] M. Schaffner, P. A. Rühs, F. Coulter, S. Kilcher, and A. R. Studart, *3d printing of bacteria into functional complex materials,* Science Advances **3** (2017), 10.1126/sciadv.aao6804.

[17] P. S. Stewart and M. J. Franklin, *Physiological heterogeneity in biofilms,* Nature Reviews Microbiology **6**, 199 (2008).

[18] W. H. DePas, D. A. Hufnagel, J. S. Lee, L. P. Blanco, H. C. Bernstein, S. T. Fisher, G. A. James, P. S. Stewart, and M. R. Chapman, *Iron induces bimodal population development by escherichia coli,* Proceedings of the National Academy of Sciences **110**, 2629 (2013).

[19] S. V. Murphy and A. Atala, *3d bioprinting of tissues and organs,* Nature Biotechnology **32**, 773 (2014).

[20] J. P. K. Armstrong, M. Burke, B. M. Carter, S. A. Davis, and A. W. Perriman, *3d bioprinting using a templated porous bioink,* Advanced Healthcare Materials **5**, 1724 (2016).

[21] B. A. E. Lehner, D. T. Schmieden, and A. S. Meyer, *A straightforward approach for 3d bacterial printing,* ACS Synthetic Biology **6**, 1124 (2017).

[22] C. K. Kuo and P. X. Ma, *Maintaining dimensions and mechanical properties of ionically crosslinked alginate hydrogel scaffolds in vitro,* Journal of Biomedical Materials Research Part A **84A**, 899 (2008).

[23] M. M. Barnhart and M. R. Chapman, *Curli biogenesis and function,* Annual review of microbiology **60**, 131 (2006).

[24] O. A. McCrate, X. Zhou, C. Reichhardt, and L. Cegelski, *Sum of the parts: Composition and architecture of the bacterial extracellular matrix,* Journal of Molecular Biology **425**, 4286 (2013).

[25] X. Wang, D. R. Smith, J. W. Jones, and M. R. Chapman, *In vitro polymerization of a functional escherichia coli amyloid protein,* Journal of Biological Chemistry **282**, 3713 (2007).

[26] M. Hammar, Z. Bian, and S. Normark, *Nucleator-dependent intercellular assembly of adhesive curli organelles in escherichia coli,* Proceedings of the National Academy of Sciences **93**, 6562 (1996).

[27] M. Hammar, A. Arnqvist, Z. Bian, A. Olsén, and S. Normark, *Expression of two csg operons is required for production of fibronectin- and congo red-binding curli polymers in escherichia coli k-12,* Molecular microbiology **18**, 661 (1995).

[28] M. L. Evans and M. R. Chapman, *Curli biogenesis: Order out of disorder,* Biochimica et Biophysica Acta (BBA) - Molecular Cell Research **1843**, 1551 (2014).

[29] T. Coenye and H. J. Nelis, *In vitro and in vivo model systems to study microbial biofilm formation,* Journal of Microbiological Methods **83**, 89 (2010).

[30] D. Singh, D. Singh, and S. S. Han, *3d printing of scaffold for cells delivery: Advances in skin tissue engineering,* Polymers **8**, 19 (2016).

[31] K. Markstedt, A. Mantas, I. Tournier, H. Martínez Ávila, D. Hägg, and P. Gatenholm, *3d bioprinting human chondrocytes with nanocellulose–alginate bioink for cartilage tissue engineering applications,* Biomacromolecules **16**, 1489 (2015).

[32] L. C. Gerber, A. Calasanz-Kaiser, L. Hyman, K. Voitiuk, U. Patil, and I. H. Riedel-Kruse, *Liquid-handling lego robots and experiments for stem education and research,* PLOS Biology **15**, e2001413 (2017).

[33] A. C. Estes and C. Baltimore, *Using k'nex to teach large scale structures to architects and construction students,* 121st ASEE Annual Conference & Exposition Proceedings: Indianapolis, IN (2014).

[34] N. van Gerven, P. Goyal, G. Vandenbussche, M. de Kerpel, W. Jonckheere, H. de Greve, and H. Remaut, *Secretion and functional display of fusion proteins through the curli biogenesis pathway,* Molecular microbiology **91**, 1022 (2014).

[35] X. Wang, Y. Zhou, J.-J. Ren, N. D. Hammer, and M. R. Chapman, *Gatekeeper residues in the major curlin subunit modulate bacterial amyloid fiber biogenesis,* Proceedings of the National Academy of Sciences **107**, 163 (2010).

[36] A. Y. Chen, Z. Deng, A. N. Billings, Seker, Urartu O. S., M. Y. Lu, R. J. Citorik, B. Zakeri, and T. K. Lu, *Synthesis and patterning of tunable multiscale materials with engineered cells,* Nature Materials **13**, 515 (2014).

[37] Y. Zhou, D. R. Smith, D. A. Hufnagel, and M. R. Chapman, *Experimental manipulation of the microbial functional amyloid called curli,* Methods in molecular biology (Clifton, N.J.) **966**, 53 (2013).

[38] D. Byrom, *Biomaterials: novel materials from biological sources* (Springer, 1991).

[39] H. Ceri, M. E. Olson, C. Stremick, R. R. Read, D. Morck, and A. Buret, *The calgary biofilm device: New technology for rapid determination of antibiotic susceptibilities of bacterial biofilms,* Journal of Clinical Microbiology **37**, 1771 (1999).

[40] T. Bjarnsholt, M. Alhede, M. Alhede, S. R. Eickhardt-Sørensen, C. Moser, M. Kühl, P. Ø. Jensen, and N. Høiby, *The in vivo biofilm,* Trends in Microbiology **21**, 466 (2013).

[41] H. Song, M.-Z. Ding, X.-Q. Jia, Q. Ma, and Y.-J. Yuan, *Synthetic microbial consortia: from systematic analysis to construction and applications,* Chemical Society Reviews **43**, 6954 (2014).

[42] K. Zhou, K. Qiao, S. Edgar, and G. Stephanopoulos, *Distributing a metabolic pathway among a microbial consortium enhances production of natural products,* Nature Biotechnology **33**, 377 (2015).

[43] S. G. Hays, W. G. Patrick, M. Ziesack, N. Oxman, and P. A. Silver, *Better together: engineering and application of microbial symbioses,* Current Opinion in Biotechnology **36**, 40 (2015).

[44] N. Jagmann and B. Philipp, *Design of synthetic microbial communities for biotechnological production processes,* Journal of Biotechnology **192**, 293 (2014).

[45] J. L. Connell, E. T. Ritschdorff, M. Whiteley, and J. B. Shear, *3d printing of microscopic bacterial communities,* Proceedings of the National Academy of Sciences **110**, 18380 (2013).

[46] Z. Lewandowski and H. Beyenal, *Biofilm monitoring: a perfect solution in search of a problem,* Water Science and Technology **47**, 9 (2003).

[47] P. Q. Nguyen, Z. Botyanszki, Tay, Pei Kun R., and N. S. Joshi, *Programmable biofilm-based materials from engineered curli nanofibres,* Nature Communications **5**, 4945 (2014).

[48] P. Q. Nguyen, *Synthetic biology engineering of biofilms as nanomaterials factories,* Biochemical Society Transactions **45**, 585 (2017).

[49] D. R. Lovley, *e-biologics: Fabrication of sustainable electronics with "green" biological materials,* mBio **8**, e00695 (2017).

[50] P. K. R. Tay, P. Q. Nguyen, and N. S. Joshi, *A synthetic circuit for mercury bioremediation using self-assembling functional amyloids,* ACS Synthetic Biology **6**, 1841 (2017).

[51] M. Dade-Robertson, A. Keren-Paz, M. Zhang, and I. Kolodkin-Gal, *Architects of nature: growing buildings with bacterial biofilms,* Microbial Biotechnology **10**, 1157 (2017).

[52] C. Prigent-Combaret, E. Brombacher, O. Vidal, A. Ambert, P. Lejeune, P. Landini, and C. Dorel, *Complex regulatory network controls initial adhesion and biofilm formation in escherichia coli via regulation of the csgd gene,* Journal of Bacteriology **183**, 7213 (2001).

[53] J. E. Stefano, J. W. Ackerson, and J. D. Gralla, *Alterations in two conserved regions of promoter sequence lead to altered rates of polymerase binding and levels of gene expression,* Nucleic Acids Research **8**, 2709 (1980).

[54] A. Skerra, *Use of the tetracycline promoter for the tightly regulated production of a murine antibody fragment in escherichia coli,* Gene **151**, 131 (1994).

[55] B. P. Cormack, R. H. Valdivia, and S. Falkow, *Facs-optimized mutants of the green fluorescent protein (gfp),* Gene **173**, 33 (1996).

[56] C. A. Schneider, W. S. Rasband, and K. W. Eliceiri, *Nih image to imagej: 25 years of image analysis,* Nature Methods **9**, 671 (2012).

[57] J. R. Kelly, A. J. Rubin, J. H. Davis, C. M. Ajo-Franklin, J. Cumbers, M. J. Czar, K. de Mora, A. L. Glieberman, D. D. Monie, and D. Endy, *Measuring the activity of biobrick promoters using an in vivo reference standard,* Journal of Biological Engineering **3**, 4 (2009).

[58] A. Colman-Lerner, T. E. Chin, and R. Brent, *Yeast cbk1 and mob2 activate daughter-specific genetic programs to induce asymmetric cell fates,* Cell **107**, 739 (2001).

# 7

# CONCLUSION

This study was set out to investigate if bacteria can be used to produce nacre-inspired materials, mimicking both some of the morphological and mechanical features while maintaining an eco-friendly production method. Current methods for the production of nacre-mimicking materials focus on achieving nacre's structures and mechanical properties, while the very efficient, biological production process is largely ignored. Bacteria are well-established in biotechnology for the production of diverse compounds and materials since they show a very large number of metabolic abilities and are easy to handle and manipulate. This study sought to answer four main research questions pertaining to the goal of producing bacterial nacre. The main empirical findings are presented in Chapters 2, 3, 5 and 6. Here, the most important results are summarized to answer the research questions:

1. **Can bacterial products be combined to produce a new composite material that shares morphological features with nacre?**

   When bacterial calcium carbonate and polyglutamate were alternately deposited on substrates to produce bacterial nacre, layered structures could be observed in the material's cross-sections, suggesting that polyglutamate has a templating effect on calcium carbonate crystallization. The calcium carbonate was found to be a mixture of calcite and vaterite, as opposed to aragonite in natural nacre. Up to 50% of bacterial nacre's cross-sectional areas showed layers, with a thickness of approx. 8 µm. Furthermore, the produced layers where not completely parallel ("wavy") and showed asperities in the interlayer space. The organic content of bacterial nacre was estimated to be approx. 4.5%, which is comparable to natural nacre with 5%. Thus, the bacterial nacre shared some morphological features with the much more complex natural nacre (wavy layers, asperities, and organic content), but differed in other aspects (crystal structure, un-layered parts, composition of the organic matrix).

2. **Does this composite show improved mechanical properties compared to its constituents, and if yes, what are probable mechanisms?**

While bacterially and chemically-produced calcium carbonate coatings developed macrocracks during deformation, no such cracks were visible in bacterial nacre, suggesting that the material failed with a series of microcracks. The distinct cracking behavior might be the cause for the improved mechanical properties: bacterial nacre displayed a four-fold higher toughness and double strain at failure compared to bacterial $CaCO_3$, while maintaining a similar macroscopic flexural stiffness. Since bacterial nacre shares structural features with natural nacre, some of the same toughening mechanisms might be involved, e.g. interlocking of layers, local strain-hardening through nano-asperities, and the organic phase acting as a viscoelastic glue.

3. **Can bacteria be arranged efficiently and in a cost-effective way in a 3D space, while maintaining metabolic activity and the possibility of external control?**

   Bacteria suspended in bioink were printed with re-purposed or self-built, low-cost 3D printers. The resulting millimeter- to centimeterscale structures showed submillimeter resolution and mixing of bacteria of neighbor layers was very limited. The expression of genes could be controlled effectively with diffusible inducers, as evidenced by the expression of RFP or the biofilm protein CsgA. The bacteria displayed robust survival for one week after the print on an agar plate.

4. **Can control of biofilm formation be used to stabilize bacteria in 3D-printed hydrogels towards the production of organic matrices for bioengineering applications?**

   Gels produced by 3D printing alginate-based bioinks are susceptible to dissolution. *Escherichia coli* was 3D-printed and induced to produce curli fibers that form the main extracellular component of *E. coli* biofilms. The resulting gels were resistant to dissolution with citrate, demonstrating that a stable biofilm had formed in the printed structures.



This study has shown that bacteria can be used to produce new nacre-inspired materials, which share some morphological features, and possibly toughening mechanisms, with natural nacre. 3D printing was used to pattern bacteria on the macroscale. Future research should focus on improving and combining these methods:

- **Biomineralization through modified microorganisms**

  In this study, *Sporosarcina pasteurii* was used to generate calcium carbonate. To produce nacre-mimicking materials with bacteria, additional metabolic activities will likely be required, e.g. the production of curli fibers for matrix stabilization, or expression of matrix proteins of natural nacre for crystallization control (see below). Thus, *S. pasteurii* should be replaced by a more easily usable model organism such as *E. coli* or *B. subtilis*, for example by expressing urease or carbonic anhydrase from plasmids.

- **Up-scaling to the centimeter-scale in all 3 dimensions**

In this study, bacteria were 3D-printed in structures of several millimeters thickness. The next step towards bulk materials will be to up-scale to the centimeter-scale. The chemistry of alginate gelation is a major obstacle, since alginate crosslinks when complexing calcium ions, which in turn are furnished by diffusion from the printing substrate. Thus, gelation slows down with increased thickness of the printed structure, resulting in slower gelation speed and decreased resolution. Possible solutions to this problem include replacement of alginate by another compound with an alternative crosslinking mechanism (such as UV-crosslinking), periodic submersion of the gel into calcium ion-containing solutions, or simultaneous printing of bioink and calcium ions through separate channels.

- **Biomineralization in 3D-printed bioink gels**

  In Chapters 2 and 3, a production method for bacterial nacre was described. For the crystallization of each layer of calcium carbonate, the substrate was submerged into bacteria culture for one night. Thus, one layer can be produced per day, resulting in a very slow and labor-intensive production process. To achieve bacterial nacre as bulk material instead of a coating, a more efficient process is required. The growth of natural nacre can serve as inspiration: mollusks crystallize layers of calcium carbonate, but crystallization of several layers can occur in parallel (Figure 1.5) in a pre-formed organic matrix. In Chapter 6, bacteria were 3D-printed in an alginate gel and induced to form curli fibers to interconnect each other, thus effectively producing a 3D organic matrix. Consequently, the next step should be the combination of 3D printing and biomineralization, e.g. by modifying the curli-formers to produce calcium carbonate, or by printing mixed cultures. Several challenges will have to be overcome to achieve this goal:

  - Upon calcium carbonate crystallization, $Ca^{2+}$-ions will be sequestered from the matrix in large numbers, which will dissolve the cross-linked alginate gel. While curli-expression was shown to be sufficient to stabilize the gels after calcium-removal, the gels were observed to soften as a result (Section 6.2.6). Establishing the mechanical properties of the gels in relation to curli expression (e.g. through rheometry or indentation) will help to tune the gel properties for optimum stability.
  - Precursor transport into printed gels will be a major obstacle. Calcium carbonate crystallization requires large amounts of calcium and carbonate ions, but the concentrations of the ions or precursor substances will have to be limited to allow for the survival and metabolic activity of the bacteria. Furthermore, diffusion is slow over distances greater than 1 mm and crystallization will occur first at the gel-medium interfaces, further blocking diffusion of ions into the inner volumes of the gel. A possible solution could be the printing of gels with channels for liquid perfusion, comparable to the tissues of animals. 3D printing lends itself naturally to the production of channel-containing gels, due to its high precision and resolution.
  - Biofilms are highly heterogeneous, with cells in many different metabolic states. In this study, no sub-populations regarding curli production were observed, but it is conceivable that such populations will form in thicker gels

when nutrient and oxygen supply varies depending on the location. This heterogeneity will likely affect crystallization, so that new methods for the minimization of cell variability will be required, either by improved genetic control or the incorporation of channels, as described above.

– Mollusks maintain tight genetic control over calcium carbonate crystallization, restricting both the crystal type (aragonite in nacre) and the overall morphology of the crystals (platelets). To produce high-performance materials with bacteria, a comparable control over crystallization might be required, or could be used to tune the mechanical properties. Crystallization control could be achieved by expression of nacre matrix proteins by the bacteria, or by modification of the curli fibers themselves, which could bear side-chains known to modulate crystal formation.

Several limitations arose during the execution of this study as a consequence of the employed methods, which should be addressed in future research:

1. The control over calcium carbonate formation in bacterial nacre was not as rigorous as in animals. Layered structures were observed in less than half of the cross-sectional areas, resulting in a mixed material. The layered and unlayered parts probably exhibit different mechanical properties, which cannot be differentiated with the examination methods used in this study. Future research should focus on improving crystallization control to achieve a higher layered fraction of volume, e.g. through genetic engineering. Non-destructive imaging methods such as X-ray microtomography could be useful to identify layered areas prior to the mechanical tests.

2. The distinct cracking mechanism and the involvement of structures such as asperities and layers were inferred from 3-point bending curves. Mechanical testing under direct observation, e.g. through SEM or AFM, could help to confirm the actual mechanisms.

3. Bacterial nacre consisted of a mixture of vaterite and calcite, and since vaterite converts to calcite over time, the mechanical properties might not be constant. Natural nacre proteins could be included in the production process. This alteration could help to achieve pure calcite or even aragonite materials, as well as providing an exciting new way to research the mechanisms underlying the formation of natural nacre.

4. To achieve higher reproducibility, relatively expensive high-purity chemicals were used in the experiments, somewhat counteracting the aim of a cost-effective production method. Future methods should make use of cheap components, for example of waste products (e.g. urine as urea source).

5. The K'NEX 3D printer uses DC-motors for actuation of the stage. While this design decision facilitated the interfacing of K'NEX parts and electronic components, the precision of the stage movement suffered, as the stage position had to be determined with ultrasound sensors. Commercial 3D printers (such as the one pre-

sented in Chapter 5) use high-precision step motors, which do not require positional feedback apart from an initial calibration. Future iterations of the biolinker could be easily adapted to use these step motors.

6. Due to the low sample thickness fitting into the confocal microscope, the experiments used to investigate mixing behavior in printed gels (Figures 5.4 and 6.6) cannot depict the true bacteria distribution with certainty. Figure 5.4 was produced by printing bioink on a dialysis membrane, which was used for the transfer prior to imaging, leading to disruption of the gel structure. Figure 6.6 was produced by solidifying the gel on a microscope coverslip, which allows imaging without gel disruption, but which is not identical to printing on an agar substrate. To avoid disruption, the gels could be frozen and sectioned with a microtome prior to imaging.

This study has shown that the production of nacre-mimicking materials does not require high-tech equipment, vast amounts of energy, or a large monetary investment. Instead, significant hurdles were overcome towards a production method that mimics natural nacre growth. Even though it is much simpler than natural nacre and does not reach its outstanding mechanical properties yet, bacterial nacre shows a hierarchical structure and improved mechanical properties that vastly surpass what would be expected from the rule of mixtures. With the possibility of bacteria patterning and of expression of natural nacre proteins, the potential to improve bacterial nacre is far from exhausted.

Many applications for future iterations of bacterial nacre are conceivable. Natural nacre has been used as a tooth replacement and for the treatment of bone diseases. When produced in the lab, nacre-mimetic materials could be used as prostheses or (temporary) implants for the stabilization of fractured bones. The material properties could be tuned towards toughness, biocompatibility, longevity, or even resorption and replacement by natural bone. In civil engineering, bacterial nacre could be a valuable replacement for cement. The production of cement requires vast amounts of energy and is responsible for up to 5% of the global emissions of $CO_2$. Bacterial nacre could be produced by fixing $CO_2$ from the atmosphere, thus not only decreasing emissions, but actively counteracting $CO_2$ accumulation. If the mechanical properties of natural nacre could be reached, bacterial nacre would surpass concrete as building material in many aspects, allowing for thinner, lighter, and tougher houses, bridges, etc. When tuned towards toughness, reliability, and low weight, bacterial nacre could be used as a structural component in cars, ships, or planes.

Bacteria engineered to produce materials require very little space when stored or transported, and they are easily kept alive by freezing or as spores. This fact makes them ideal candidates as tools for space exploration. With a genetic engineering facility on site, bacteria could be easily modified and tuned to mission requirements with the help of genetic information sent from earth. Instead of finished parts, construction plans could be sent digitally and realized by 3D printing. Together with *in situ* methods of resource extraction, this would allow for a fundamental shift in building and supply of extra-terrestrial colonies: Instead of sending supply shipments with space ships, only information would need to be transmitted to produce new materials on site, potentially leading to huge cuts in the cost of space exploration.

# ACKNOWLEDGMENTS

Here it is, the only chapter most people will read, but I am happy you are here, because it's important! Even though only my name is printed on the cover of this dissertation, it is actually the result of a collaboration of many wonderful people, who assisted me in various ways to reach the point where I am now, be it by teaching me to be a better scientist and experimenter, by helping me write the papers and this dissertation, or just by joining me in the lunch breaks and sharing stories about our 'horrible' PhD student lives. As I am sure to forget the one or the other name, I'd like to thank all members and former members of the Bionanoscience Department of TU Delft for four great years. I am sure to always remember my time with you fondly.

Without any doubt, my professors Anne and Marie had the biggest impact on my time in Delft. I am deeply grateful that you gave me the chance to work with you, and for being such great people to work with. You taught me how to be a scientist, to design and manage experiments, to supervise students, and to present my work to others. At the same time, you left me my independence and allowed me to pursue the ideas I had, but you were always there when I needed help. I can sincerely say that I could not have hoped for better professors to work with, and that you are responsible in large parts for me having such a great time doing my PhD. Also thank you Bertus for being my mentor, thanks to the qualities of Anne and Marie, I never needed your help in that function, but I enjoyed talking to you over the coffee breaks very much.

Next I would like to thank the many members of Anne's and Marie's groups who I had the pleasure of meeting over the years (in no particular order): Mathia, Michela, Lisa, Irfan, Kuang, Ramon, Guillermo, Chaline, and Kui. Ewa, I am very happy that you joined my project, not only because it's great to have you around, but also because with your help we managed to get measurable results for the nacre project. Da, you impressed me with your keen mind and your excellent taste in science fiction literature. Victor, I remember many funny lunchtime conversations with you, where you showed an incredibly open mind and excellent humor. While I like you a lot as a person, Vanessa, you deeply impressed me with your persistence in doing a much harder PhD than I did, and as such you will always be a role model for me. Benjamin, it was great working with you in the 3D printer project, I admire you for your apparently permanently good mood, which transfers to the people around you. Aurora, you were a partner in crime when it came to secret candy, and with your great sense of humor it is always nice to have you around any coffeebreak. Ilja, you are excellent at your job, and you were a major factor in getting my experiments working, thank you! Jaqueline and Simon, you were the first Dutch colleagues I really got to know, and you both introduced me to this particular brand of humor that is so widely spread in the Netherlands. Even though you left after around two years, I remember you as the people who were with me when my adventure in Holland began.

I would also like to thank the astonishing number of Bachelor and Master students I met during my PhD time, in particular those who worked with me on the project: Nadine, Fiona, two Jeroens, Roel, Heleen, and Erick. All of you did great jobs and showed a high level of independence and ingenuity. I suspect I learned more from working with you than the other way around, so thank you! Of course also a big thank you to the three iGEM teams I had the chance to work with, especially to the 2015 team who had the idea to use bacteria for 3D printing, which became a big part of my PhD. A big thank you also to my advisor colleagues Jorine, Helena, Essie, and Timon, I had a great time working together with you!

Since the PhD usually involves diving into areas you have no experience in, you need help from a large number of people, and this was no different for me. I found my colleagues at BN, but also at other departments always happy to help me, so a big thank you to all the heroes at TU Delft who keep things running and help so many PhD students reach the point where I am now. Thank you Jérémie, Sacha, Jelle, Wiel, Eve, Theo, Erwin, Dimitri, Jan, Anke, Richard, Anna, Marije, Chantal, Amanda, and Jolijn. A big thank you also to our collaborators in the Faculty of Aerospace Engineering of TU Delft, Santiago and Antonio. You taught me with great patience the foundations of mechanical characterization and showed me how to use the machines. Without you it would have been very difficult to measure to properties of our materials. Finally, a thank you to those colleagues who were not directly involved in my research, but who I'll always remember with a big smile for the nice geeky chats we had in the coffee corner or just in the hallways between the labs: Marek, Jan, Ferhat, and Nicole. Thank you also to Jochem, who was not only a very nice office mate, but who also helped me with the Dutch summary of this dissertation, together with Stan, my awesome Dutch teacher!

Finally a big thank you to Mihaela, who was a great roommate during my first two years in Delft. I am very happy to have had the pleasure to work and live with you at the same places! A very big thank you also to Roland, who not only helped me a lot to achieve my PhD, but who also became one of my most dear friends and my most trusted sports partner! I would also like to say thank you to my parents Uschi and Klaus, who supported me in my endeavor to become a scientist, and to my sister Antonia and my brother Jonas and their families, who make me very happy whenever I get to meet them. Thank you for being in my life!

Ironically, despite all the great experiences I had during the four years of my PhD, the most important thing happened right at the start, when I met Maithili, who is my wonderful wife today. Maithili, you are more important to me than any title or achievement, and I am deeply greatful and happy that you are spending your life with me!

# Curriculum Vitæ

## Dominik Tobias Schmieden

08.03.1986 Born in Wiesbaden, Germany.

### Education

1996–2005 Secondary School
Göttenbach-Gymnasium, Idar-Oberstein

2007–2013 Diplom in Biology
Johannes Gutenberg-Universtät, Mainz

# List of Publications

7. **Schmieden, Dominik T.**; Spiesz, Ewa M.; Liang, Kuang; Grande, Antonio M.; Schwiedrzik, Jakob; Natalio, Filipe; Michler, Johann; Garcia, Santiago J.; Aubin-Tam, Marie-Eve; Meyer, Anne S., *Bacterially-Produced, Nacre-Inspired Composite Materials*, submitted.

6. Majerle, Andreja; **Schmieden, Dominik T.**; Jerala, Roman; Meyer, Anne S., *Synthetic biology for multiscale designed biomimetic assemblies: from designed self-assembling biopolymers to bacterial bioprinting*, submitted.

5. Spiesz, Ewa M.; Yu, Kui; Lehner, Benjamin A.E.; **Schmieden, Dominik T.**; Aubin-Tam, Marie-Eve; Meyer, Anne S., *3D patterning of engineered biofilms with a DIY bioprinter*, submitted.

4. **Schmieden, Dominik T.**; Basalo Vázquez, Samantha J.; Sangüesa, Héctor; van der Does, Marit; Idema, Timon; Meyer, Anne S., *Printing of Patterned, Engineered E. coli Biofilms with a Low-Cost 3D Printer*, ACS Synthetic Biology 7.5 (2018).

3. Lehner, Benjamin A. E.; **Schmieden, Dominik T.**; Meyer, Anne S., *A Straightforward Approach for 3D Bacterial Printing*, ACS Synthetic Biology 6.7 (2017).

2. **Schmieden, Dominik T.**; Meyer, Anne S.; Aubin-Tam, Marie-Eve, *Using Bacteria to Make Improved, Nacre-Inspired Materials*, MRS Advances 1.8 (2016).

1. Graf, Sabrina; **Schmieden, Dominik T.**; Tschauner, Karolin; Hunke, Sabine; Unden, Gottfried, *The Sensor Kinase DctS Forms a Tripartite Sensor Unit with DctB and DctA for Sensing C4-Dicarboxylates in Bacillus subtilis*, Journal of Bacteriology (2013): JB-01154.